Evolution of Deformation Along Restraining Bends Based on Case Studies of Different Scale and Complexity

William Joseph Cochran

Dissertation submitted to the faculty of the Virginia Polytechnic Institute and State University in partial fulfillment of the degree of

Doctor of Philosophy
In
Geosciences

James A. Spotila. Chair
Brian W. Romans.
John A. Hole
Richard D. Law
Esteban Gazel

April 18th, 2018
Blacksburg, Virginia

Keywords: Tectonics, Low-temperature thermochronometry, high-resolution topography, transpression, strike-slip faults

Evolution of Deformation Along Restraining Bends Based on Case Studies of Different Scale and Complexity

William Joseph Cochran

ABSTRACT

Globally, deformation along obliquely converging plate margins produce a wide variety of complex fault patterns, including crustal pop-ups, fault duplex structures, restraining bends, and flower structures. Depending on the plate velocity, plate obliquity, crustal rheology, length-scale, and climate, the evolution of faulting into translational and vertical strain can range in complexity and fault slip partitioning (i.e. vertical vs. horizontal strain). In this dissertation I studied two restraining bends to understand how these factors influence patterns of deformation along two major plate boundaries: The North American-Caribbean and the North American-Pacific plate boundaries. First, I estimate the exhumation and cooling history along the Blue Mountains restraining bend in Jamaica using multiple thermochronometers. Three phases of cooling have occurred within Jamaica: 1) initial rock crystallization and rapid emplacement of plutons from 75-68 Ma, 2) slow cooling from 68-20 Ma, and 3) two-stage exhumation from 20 Ma – Present. During the most recent phase of Jamaica's cooling history, two stages of exhumation have been identified at 0.2 mm/yr (20 – 5 Ma) and ~1 mm/yr (5 Ma – Present). Given the plate velocity to exhumation rate ratio during the most recent phase, we suggest that the climate of Jamaica increases the erosivity of the Blue Mountain suite, whereby the Blue Mountains may be in an erosional stead-state. Second, I studied the long-term evolution of a restraining bend at San Gorgonio Pass in southern California by relating fault kinematics within the uplifted San Bernardino Mountains to the nearby Eastern California shear zone. Using high-resolution topography (i.e. UAV and lidar surveys), I studied the plausibility of faulting along two potentially nascent faults within the San Bernardino Mountains, namely the Lone Valley and Lake Peak faults. We found that while both faults display evidence for Quaternary faulting, deciphering true fault slip rates was challenging due to the erosive nature of the mountainous landscape. Coupled with evidence of Quaternary faulting along other faults within the San Bernardino Mountains, we suggest a western migration of the Eastern California shear zone.

Evolution of Deformation Along Restraining Bends Based on Case Studies of Different Scale and Complexity

William Joseph Cochran

GENERAL AUDIENCE ABSTRACT

The deformation of rocks along tectonic plate boundaries provides insight into how the upper crust behaves, and is dependent on the crustal strength, plate velocity, temporal and spatial scales, and climate. At most convergent plate boundaries, plate motion is oblique to the plate boundary, resulting in zones of transpression: compression and translation. Geologists refer to these features as restraining bends. What factors dictate how faults within restraining bends evolve is a major question in the field of tectonics. In this dissertation I studied two major restraining bends which differ in both scale (i.e. length to width ratio) and climate, namely the Blue Mountains restraining bend in Jamaica and the restraining bend at San Gorgonio Pass in southern California. Along the Blue Mountains restraining bend, it was not understood when or how fast this mountain range was being exhumed due to the tectonic forces being applied to the plate boundary. I use a technique called thermochronometry, whereby instead of measuring the age of rock crystallization, I measure when the rock cools below a certain temperature. Different minerals have different closure temperatures, and by using multiple minerals, I determined the cooling path of the rocks in the Blue Mountains since they crystalized in the late Cretaceous (~75 million years ago). We found that the rocks experienced three different phases of cooling, with a more recent phase being divided into two stages since 20 Ma: Blue Mountain rocks being exhumed at a rate of 0.2 mm/yr from 20 – 5 Ma (relatively slow) and ~1 mm/yr from 5 – 0 Ma (relatively fast). I concluded that the climate of Jamaica weathers and erodes rocks so efficiently that the Blue Mountains are in an erosional balance between plate tectonic forces and climatic forces. My second chapter identifies small, unstudied faults within the San Bernardino Mountains, and determined that these faults display enough evidence that they should be considered a earthquake hazard. The restraining bend itself is migrating towards the southeast and is being influenced by other faults in the area. What once was a predominantly transpressional system, is now being influenced mainly by strike-slip faulting.

ACKNOWLEDGEMENTS

I would like to thank my advisor, Dr. Jim Spotila, for providing continued support and drive which lead me to grow as a geoscientist. His unwavering ability to teach and guide me through my dissertation gave me the confidence in my abilities I needed to complete my degree. I would also like to thank my committee members: Dr. Rick Law, Dr. Esteban Gazel, Dr. John Hole, and Dr. Brian Romans for their input and guidance in my writing and research. Additionally, I would like to thank P. Prince for bringing the Jamaica project and dropping it in my lap, doing field work in both Jamaica and California, and being a beast when it comes to making field work happen.

I would like to thank my family, including my mother Linda Ward, father Bill Cochran, step father Greg DeBerry, and brother Ryan Cochran, for always encouraging me to be the best I can be. Their continued love and support through the toughest of times always provided the necessary energy to push through. I would also like to acknowledge my friends who consistently provided the necessary social outlet for times when I needed to break from work. Additionally, my office mates who were always down to chat about research.

Finally, I would like to thank the Universe…just because.

FINANCIAL SUPPORT

Financial support for Chapter Two was provided by graduate student grants and other funds through my advisor by the Geological Society of America. Financial support for Chapter Three was provided by the National Science Foundation grant EAR-1145115 and NCALM seed proposal funding for flying the lidar survey.

ATTRIBUTIONS

Chapter Two has been accepted and was published in *Tectonophysics* in 2017. The co-authors are James A. Spotila, Philip P. Prince, and Ryan J. McAleer. I collected and processed samples, conducted analyses, interpreted data, conducted thermal modeling, and wrote the manuscript. Jim Spotila assisted in sample analyses and manuscript editing. Philip Prince helped with field work and writing on the manuscript, and Ryan McAleer for the argon-argon analysis and helping with the writing process.

Citation:

Cochran, W. J., Spotila, J. A., Prince, P. S., & McAleer, R. J. (2017). Rapid exhumation of Cretaceous arc-rocks along the Blue Mountains restraining bend of the Enriquillo-Plantain Garden fault, Jamaica, using thermochronometry from multiple closure systems. *Tectonophysics*, *721*, 292-309.

Chapter Three is in preparation for submission to *Bulletin of the Seismological Society of America*. The co-authors are James A. Spotila and Philip P. Prince. I conducted field work, sample preparation, and data analyses, and wrote the manuscript. Co-author Jim participated in field work and helped with the writing of the manuscript. Philip Prince assisted in field work.

Citation:

Cochran, W. J., Spotila, J. A., and Philip P. Prince (in prep.), Incipient evolution of the Eastern California shear zone through the transpressional zone of the San Bernardino Mountains, CA.

TABLE OF CONTENTS

Chapter One

1.1.0 INTRODUCTION

Deformation patterns associated with plate boundaries provide important evidence for the dynamics of crustal evolution in plate tectonics (Molnar, 1988). Purely convergent/divergent/ transform plate boundaries rarely occur, resulting in oblique plate velocity vectors composed of both pure and simple shear (Woodcock, 1986). Along strike-slip plate boundaries where a significant portion of deformation is partitioned into pure shear, namely transpressional/ transtensional boundaries, several factors influence how these systems evolve, including variation in fault geometry, plate motion obliquity, plate velocity, and rheology (Mann, 2007). Additionally, the type of structures formed as a result of oblique deformation is quite broad, including flower structures, crustal pop-ups, duplex structures, and paired bends (Cunningham and Mann, 2007). Understanding the role each factor plays in redistributing strain within the upper crust, and how they influence the formation of these structures through fault-strand development is not well understood. The range of complexity (i.e. interacting fault systems) and scale of transpressional/transtensional zones necessitates the need for understanding how these systems evolve.

Several deformation patterns have been observed along transpressional plate boundaries (Dewey et al., 1998; Harland, 1971; Sylvester, 1988). Two classes of these deformation behaviors occur under what are called pure-shear-dominated and wrench-dominated conditions, typically transitioning when plate motion obliquity (α) exceeds 20^{o} (Teyssier et al., 1995). Deformation tends to be distributed across wide zones of variable strain-partitioning and rock uplift where plate motion obliquity is high (i.e. $\alpha \geq 20^{o}$), such as the Lebanese restraining bend (Gomez et al., 2007) and Alpine fault (e.g. Little et al., 2005). Complicating factors, such as climate, surface erosivity, and topography, all influence erosion and rock uplift and therefore the

mass-balance and state of stress within the upper crust (Benowitz et al., 2011; Buscher and Spotila, 2007; Cowgill et al., 2004; Cruz et al., 2007; Spotila et al., 2007a). Below I introduce Chapters Two and Three and give an overview of the findings.

1.2.0 SUMMARY OF CHAPTER TWO AND THREE

In this dissertation, I present the results of two different research projects: 1) the exhumation and rock uplift history of the Blue Mountains restraining bend (BMRB) in Jamaica using low-temperature thermochronometry, and 2) the transient evolution of the restraining bend at the San Bernardino Mountains (SBM) in southern California, specifically looking at evidence for incipient strike-slip faulting within the hangingwall of the bend using high-resolution topography.

Chapter Two focuses on estimating the bedrock cooling and exhumation history associated with transpression within the BMRB. The BMRB is a relatively unstudied transpressional system in a highly erosive environment and is a great example of coupling between tectonic and climate. I provide new constrains on the exhumation history of the Blue Mountains restraining bend to define the exhumation history. We measured apatite (n=10) and zircon (n=6) (U-Th)/He ages, $^{40}Ar/^{39}Ar$ (n=2; amphibole and K-spar) ages, and U/Pb zircon (n=2) crystallization ages. Late Cretaceous U/Pb and $^{40}Ar/^{39}Ar$ ages (74-68 Ma) indicate rapid cooling following shallow emplacement of plutons during north-south subduction along the Great Caribbean Arc. Early to middle Miocene zircon helium ages (19-14 Ma) along a vertical transect suggest exhumation and island emergence at ~0.2 mm/yr. Older zircon ages 10-15 km to the north (44-35 Ma) imply less rock uplift. Apatite helium ages are young (6-1 Ma) across the entire orogen, suggesting rapid exhumation of the BMRB since the late Miocene. These constraints are consistent with previous reports of restraining bend formation and early

emergence of eastern Jamaica. An age-elevation relationship from a vertical transect implies an exhumation rate of 0.8 mm/yr, while calculated closure depths and thermal modeling suggests exhumation as rapid as 2 mm/yr. The rapid rock uplift rates in Jamaica are comparable to the most intense transpressive zones worldwide, despite the relatively slow (5-7 mm/yr) strike-slip rate. We hypothesize highly erosive conditions in Jamaica enable a higher fraction of plate motion to be accommodated by vertical deformation. Thus, strike-slip restraining bends may evolve differently depending on erosivity and local climate

Chapter Two, titled "Rapid exhumation of Cretaceous arc-rocks along the Blue Mountains restraining bend of the Enriquillo-Plantain Garden fault, Jamaica, using thermochronometry from multiple closure systems", was accepted and published in the Journal *Tectonophysics*. The citation for this publication is Cochran, W. J., Spotila, J. A., Prince, P. S., & McAleer, R. J. (2017). Rapid exhumation of Cretaceous arc-rocks along the Blue Mountains restraining bend of the Enriquillo-Plantain Garden fault, Jamaica, using thermochronometry from multiple closure systems. *Tectonophysics, 721*, 292-309.

Chapter Three focus on evidence for incipient faulting within the SBM, generating new evidence for strike-slip deformation in a largely transpression setting. Measuring long-term accumulation of strike-slip displacements and transpressional uplift is difficult where strain is accommodated across wide shear zones, as opposed to a single major fault (Cunningham and Mann, 2007). The Eastern California Shear Zone (ECSZ) in southern California accommodates dextral shear across several strike-slip faults and is potentially migrating and cutting through a formerly convergent zone of the San Bernardino Mountains. The advection of crust along the San Andreas fault to the SE has forced these two tectonic regimes into creating a nexus of interacting strike-slip faults north of San Gorgonio Pass. These elements make this region ideal

for studying complex fault interactions, evolving fault geometries, and deformational overprinting within a wide shear zone. Using high-resolution topography and field mapping, this study aims to test whether diffuse, poorly formed strike-slip faults within the uplifted SBM block are nascent elements of the ECSZ. Topographic resolution of ≤ 1m was achieved using both lidar and UAV surveys along two Quaternary strike-slip faults, namely the Lake Peak fault and Lone Valley faults. Although the Lone Valley fault cuts across Quaternary alluvium, the geomorphic expression is obscured, and may be the result of slow slip rates. In contrast, the Lake Peak fault is located high elevations north of San Gorgonio Peak in the SBM and displaces Quaternary glacial deposits. The deposition of large boulders along the escarpment also obscures the apparent magnitude of slip along the fault. Although determining fault offset is difficult, the Lake Peak fault does display evidence for minor right-lateral displacement, where the magnitude of slip would be consistent with individual faults within the ECSZ (i.e. ≤ 1 mm/yr). Compared to the preservation of displacement along strike-slip faults located within the Mojave Desert, the upland region of the SBM adds complexity for measuring fault offset. The distribution of strain across the entire SBM block, the slow rates of slip, and the geomorphic expression of these faults add difficulty for assessing fault-slip evolution. Although evidence for diffuse dextral faulting exists within the formerly uplifted SBM block, future work along other known examples of faults within the SBM is needed to determine if the ECSZ is migrating west.

Chapter Three, titled “Incipient evolution of the Eastern California shear zone through the transpressional zone of the San Bernardino Mountains, CA”, is in preparation for submission to the journal *The Bulletin of the Seismological Society of America*, with co-authors James A. Spotila and Philip P. Prince.

REFERENCES

Benowitz, J. A., Layer, P. W., Armstrong, P., Perry, S. E., Haeussler, P. J., Fitzgerald, P. G., and VanLaningham, S., 2011, Spatial variations in focused exhumation along a continental-scale strike-slip fault: The Denali fault of the eastern Alaska Range: Geosphere, v. 7, no. 2, p. 455-467.

Buscher, J. T., and Spotila, J. A., 2007, Near-field response to transpression along the southern San Andreas fault, based on exhumation of the northern San Gabriel Mountains, southern California: Tectonics, v. 26, no. 5, p. n/a-n/a.

Cowgill, E., Yin, A., Arrowsmith, J. R., Feng, W. X., and Shuanhong, Z., 2004, The Akato Tagh bend along the Altyn Tagh fault, northwest Tibet 1: Smoothing by vertical-axis rotation and the effect of topographic stresses on bend-flanking faults: Geological Society of America Bulletin, v. 116, no. 11-12, p. 1423-1442.

Cruz, L., Fayon, A., Teyssier, C., and Weber, J., 2007, Exhumation and deformation processes in transpressional orogens: The Venezuelan Paria Península, SE Caribbean–South American plate boundary, v. 434, p. 149-165.

Cunningham, W. D., and Mann, P., 2007, Tectonics of strike-slip restraining and releasing bends: Geological Society, London, Special Publications, v. 290, no. 1, p. 1-12.

Dewey, J. F., Holdsworth, R. E., and Strachan, R. A., 1998, Transpression and transtension zones: Geological Society, London, Special Publications, v. 135, no. 1, p. 1-14.

Gomez, F., Nemer, T., Tabet, C., Khawlie, M., Meghraoui, M., and Barazangi, M., 2007, Strain partitioning of active transpression within the Lebanese restraining bend of the Dead Sea Fault (Lebanon and SW Syria): Geological Society, London, Special Publications, v. 290, no. 1, p. 285-303.

Harland, W. B., 1971, Tectonic transpression in Caledonian Spitsbergen: Geol. Mag., v. 108, no. 1, p. 27-42.

Little, T. A., Cox, S., Vry, J. K., and Batt, G., 2005, Variations in exhumation level and uplift rate along the obliqu-slip Alpine fault, central Southern Alps, New Zealand: Geological Society of America Bulletin, v. 117, no. 5, p. 707.

Mann, P., 2007, Global catalogue, classification and tectonic origins of restraining- and releasing bends on active and ancient strike-slip fault systems: Geological Society, London, Special Publications, v. 290, no. 1, p. 13-142.

Molnar, P., 1988, Continental tectonics in the aftermath of plate tectonics: Nature, v. 335, no. 6186, p. 131.

Spotila, J. A., House, M., Niemi, N., Brady, R., Oskin, M., and Buscher, J., 2007, Patterns of bedrock uplift along the San Andreas fault and implications for mechanisms of transpression, *in* Till, A. B., Roeske, S. M., Sample, J. C., and Foster, D. A., eds., Exhumation Associated with Continental Strike-Slip Fault Systems, Geological Society of America Special Paper 434, p. 15-33.

Sylvester, A. G., 1988, Strike-slip faults: Geological Society of America Bulletin, v. 100, no. 11, p. 1666-1703.

Teyssier, C., Tikoff, B., and Markley, M., 1995, Oblique plate motion and continental tectonics: Geology, v. 23, no. 5, p. 447.

Woodcock, N. H., 1986, The role of strike-slip fault systems at plate boundaries: Phil. Trans. R. Soc. Lond. A, v. 317, no. 1539, p. 13-29.

Chapter Two

Rapid exhumation of Cretaceous arc-rocks along the Blue Mountain restraining bend of the Enriquillo-Plantain Garden fault, Jamaica, using thermochronometry from multiple closure systems

AUTHORS:

William J. Cochran[1*], James A. Spotila[1], Philip S. Prince[1], Ryan J. McAleer[2]

[1]*Department of Geosciences, 4044 Derring Hall, Virginia Tech, Blacksburg, VA 24061, USA, cwill13@vt.edu, spotila@vt.edu*

[2]*U.S. Geological Survey, 12201 Sunrise Valley Drive, Reston, VA 20192, USA*

Keywords: Transpression, restraining bend, exhumation, (U-Th)/He thermochronometry, Jamaica, Enriquillo-Plantain Garden fault

2.0.0 ABSTRACT

The effect of rapid erosion on kinematic partitioning along transpressional plate margins is not well understood, particularly in highly erosive climates. The Blue Mountains restraining bend (BMRB) of eastern Jamaica, bound to the south by the left-lateral Enriquillo-Plantain Garden fault (EPGF), offers an opportunity to test the effects of highly erosive climatic conditions on a 30-km-wide restraining bend system. No previous thermochronometric data exists in Jamaica to describe the spatial or temporal pattern of rock uplift and how oblique (> 20^{o}) plate motion is partitioned into vertical strain. To define the exhumation history, we measured apatite (n=10) and zircon (n=6) (U-Th)/He ages, $^{40}Ar/^{39}Ar$ (n=2; amphibole and K-spar) ages, and U/Pb zircon (n=2) crystallization ages. Late Cretaceous U/Pb and $^{40}Ar/^{39}Ar$ ages (74-68 Ma) indicate rapid cooling following shallow emplacement of plutons during north-south subduction along the Great Caribbean Arc. Early to middle Miocene zircon helium ages (19-14 Ma) along a vertical transect suggest exhumation and island emergence at ~0.2 mm/yr. Older zircon ages 10-15 km to the north (44-35 Ma) imply less rock uplift. Apatite helium ages are young (6-1 Ma) across the entire orogen, suggesting rapid exhumation of the BMRB since the late Miocene. These constraints are consistent with previous reports of restraining bend formation and early emergence of eastern Jamaica. An age-elevation relationship from a vertical transect implies an exhumation rate of 0.8 mm/yr, while calculated closure depths and thermal modeling suggests exhumation as rapid as 2 mm/yr. The rapid rock uplift rates in Jamaica are comparable to the most intense transpressive zones worldwide, despite the relatively slow (5-7 mm/yr) strike-slip rate. We hypothesize highly erosive conditions in Jamaica enable a higher fraction of plate motion to be accommodated by vertical deformation. Thus, strike-slip restraining bends may evolve differently depending on erosivity and local climate.

2.1.0 INTRODUCTION

The active margins of the Caribbean plate are complex and rapidly evolving, offering unique insights into a range of tectonic processes and tectonic evolution of the greater Gulf of Mexico region (Draper and Arros, 1994; Draper et al., 1994; Mann and Burke, 1984; Pindell, 1994; Pindell et al., 2012; Robinson, 1994; Sanchez et al., 2015). The transpressive sinistral northern boundary, for example, holds clues to understanding how transform faults evolve, the influence of inherited mechanical anisotropy on nascent deformation patterns, and the role of climate and erosion on surface uplift in a tropical, oceanic setting (Fig. 1). Despite the potential for learning about basic tectonic processes in this region, first-order tectonic problems remain for various Caribbean islands produced by recent deformation. Jamaica is an excellent example of this, in that there is an incomplete understanding of how nearly a cm/yr plate motion is distributed across the island, with a lack of quantitative constraints on the history of basement uplift. A major rock uplift zone known as the Blue Mountains restraining bend (BMRB) occurs as a right-stepping bend along the main transform fault, the Enriquillo-Plantain Garden fault (EPGF), yet its exhumation history has yet to be quantified using low-temperature thermochronometry. This is a rare example of a narrow restraining bend (< 30 km) in a highly erosive climate, which stands to add to our global understanding of coupled tectonic-climatic behavior within transpressive systems.

A broad spectrum of deformational behaviors have been observed along transpressive plate margins (Dewey et al., 1998; Harland, 1971; Sylvester, 1988). Differences in how transpressive plate motion kinematically manifests as deformation depend on degree of plate motion obliquity and partitioning between coaxial and non-coaxial strain, as well as three-dimensional structure, length-scales of the deformation zone, inherited crustal rheology, and

variations in erosivity (Benowitz et al., 2011; Bourne et al., 1998; Burkett et al., 2016; Fossen and Tikoff, 1998; Fossen et al., 1994; Gomez et al., 2007; Mann, 2007; Niemi et al., 2013; Spotila et al., 2007b; Teyssier et al., 1995; Tikoff and Teyssier, 1994; Tikoff et al., 2002). Two broad classes of these deformation behaviors occur under what are called pure-shear-dominated and wrench-dominated conditions, typically transitioning when plate motion obliquity (α) exceeds 20^o (Teyssier et al., 1995). Deformation tends to be distributed across wide zones of variable strain-partitioning and rock uplift where plate motion obliquity is high (i.e. $\alpha \geq 20^o$), such as the Lebanese restraining bend (Gomez et al., 2007) and Alpine fault (e.g. Little et al., 2005). Complicating factors, such as climate, surface erosivity, and topography, all influence erosion and rock uplift and therefore the mass-balance and state of stress within the upper crust (Benowitz et al., 2011; Buscher and Spotila, 2007; Cowgill et al., 2004; Cruz et al., 2007; Spotila et al., 2007a). The complex role of topography and surface processes on partitioning deformation in transpressional systems is clearly displayed along the San Andreas fault (Spotila et al., 2007b), yet most examples of transpressional systems are from arid or semi-arid regions. Although some examples display high erosion rates due to glacial influence (e.g. Denali fault, Alpine fault), our understanding of transpression in highly erosive tropical climates is limited to Southeast Asia (e.g. Mae Ping fault, Sorong fault) and the Caribbean (e.g. EPGF, Pilar-Coche faults) regions.

An additional motivation for studying transpression in Jamaica comes from the role of transform and secondary deformation in translating and modifying slivers of volcanic island arcs prior to amalgamation as terranes that may coalesce on continental margins (Johnston, 2001; Şengör, 1987; Şengör and Natal'in, 2004). This process, known as ribbon tectonics, is suggested to be a major driving force in creating continents (e.g. Şengör and Natal'in, 2004), with the strike-slip deformation in Jamaica representing a window into the translation stage of this

process. The role of transpression in exposing and translating island-oceanic margins may hold clues about the process of crustal accretion in the formation of continents.

The BMRB in Jamaica occurs within a narrow zone (< 30 km) of uplift that is uniformly influenced by rainfall year-round, suggesting that erosion could play an important role in dictating both the strain pattern and efficiency of partitioning far-field plate motion into local vertical deformation. Yet not enough information about the onset, or rates of rock uplift exists to make a meaningful comparison to tectonic boundary conditions. Previous work suggests normal fault structures were reactivated during the Miocene as a reverse-transpressional system (Benford et al., 2014; Burke et al., 1980; Mann and Burke, 1990), but has not focused specifically on the rock uplift in the BMRB. Paleontological and sedimentological evidence suggests that the basement within the BMRB was subaerially exposed by the middle to late Miocene (James-Williamson et al., 2014), yet the timing of this uplift event has not been corroborated by rigorous, multi-mineral closure system thermochronology. As a result, the specific timing of the onset of rock uplift, how it relates to kinematics of the EPGF, and the exhumation rate within the restraining bend over the past few million years remain unknown. It is therefore not possible to compare how this transpressional example fits into the partitioning model, as well as how climate and surface erosivity affect the deformation style and rock uplift patterns.

The aim of this study is to estimate the bedrock cooling history associated with transpression and rock uplift within the BMRB, using apatite (U-Th)/He (AHe), zircon (U-Th)/He (ZHe), argon-argon ($^{40}Ar/^{39}Ar$), and zircon U-Pb dating. These isotopic ages constrain the crystallization age of basement arc-rocks and the subsequent cooling history related to recent transpressional deformation. Low-temperature cooling ages constrain the exhumation history of

the restraining bend and its current rates of rock uplift. When placed in a context of other global examples of transpression from a spectrum of tectonic and climatic conditions, the results imply that climatic controls on pure-shear dominated, non-strike-slip-partitioned, small-scale transpressional settings have a greater influence on the efficiency of exhumation and partitioning into vertical deformation.

2.2.0 TECTONIC SETTING

Jamaica is positioned along the northern boundary between the Caribbean and North American Plates, and is the emergent tip of the drowned carbonate platform of the Nicaraguan Rise (Sanchez et al., 2015). The Nicaraguan Rise is comprised of 20-28 km of volcanic arc/basaltic basement, overlain by a series of clastic, volcanic, and carbonate rocks (Arden, 1969; Mutti et al., 2005). Regionally, the tectonic setting is dominated by sinistral strike-slip faulting due to the eastward motion of the Caribbean Plate relative to the North American Plate (Fig. 1). North of Jamaica, the Gônave Microplate moves west at 7 ± 1 mm/yr relative to the Caribbean Plate (Benford et al., 2012b; DeMets and Wiggins-Grandison, 2007), and is proposed to have formed as the result of the Caribbean Plate colliding with the Bahamas Carbonate Platform in the middle to late Miocene (Mann et al., 2002; Mann et al., 1995). The boundaries of the Gônave Microplate consist of the Oriente Fault to the North, the Cayman Spreading Center to the west, the Haiti Fold-and-Thrust-Belt to the east, and the Walton and Enriquillo-Plantain Garden (EPGF) faults to the south (Fig. 1). The EPGF, which produced the Haiti earthquake of 2010 (M_w=7.0), traces more than 800 km from western Hispaniola to eastern Jamaica and forms a restraining bend in the Blue Mountains. Cutting through oceanic lithosphere, including the Caribbean Plate, the island of Hispaniola, and Jamaica, the EPGF has several zones of oblique

motion, resulting in stepovers, restraining and releasing bends, and duplexes both on- and off-shore (Benford et al., 2012a; Corbeau et al., 2016b; Leroy et al., 2015; Mann, 2007).

The tectonic history of Jamaica is recorded within the geologic assemblages across the island, divided into different tectonic blocks and belts separated by faults. This includes several Cretaceous inliers (Fig. 2a) of igneous, metamorphic, and sedimentary suites across the island (Abbott et al., 2010; Abbott et al., 2016; Brown and Mitchell, 2010; Fisher and Mitchell, 2012; Hastie et al., 2009; Mitchell, 2013a; Mitchell and Blissett, 2001; Mitchell et al., 2011; West et al., 2014), subsequent Paleocene to Eocene rift basin deposits (e.g. Mann and Burke, 1990), Eocene to Miocene carbonate platform units (Mitchell, 2004;2013b), and middle Miocene to Quaternary carbonate and clastic deposits of the Coastal Group (James-Williamson and Mitchell, 2012; James-Williamson et al., 2014). Based on the geologic and tectonic constraints, Draper (1987) originally suggested a four-stage tectonic history for the island: 1) Cretaceous to early Eocene island arc formation; 2) Paleocene to Eocene extensional phase; 3) Eocene to middle Miocene tectonically quiescent phase; and 4) middle Miocene to Quaternary left-lateral transpression causing the emergence.

Locally, Jamaica accommodates oblique collision of the Gônave microplate with the Caribbean plate, transferring plate motion from the EPGF to the Cayman Spreading Center (Burke et al., 1980; Mann and Burke, 1984; Mann et al., 1985). The island itself has been left-laterally translated several hundred kilometers since collision with the Yucatan Block in the Late Cretaceous (Hastie et al., 2010; Pindell et al., 2012). The strike-slip faults across Jamaica are E-W striking, left-lateral faults, and are thought to have formed during the formation of the Great Caribbean Arc, originally as E-W striking, northward dipping reverse structures (Benford et al., 2014; Mitchell, 2003). From north to south, the strike-slip faults consist of the Walton fault, the

Duanvale fault, the Central Jamaican fault zone (Rio Minho-Crawle River, Cavaliers, and Siloah faults), the Aeolus Valley fault (in the Blue Mountains area), the EPGF, and the South Coast fault zone (Fig. 2b). Cumulative offset across these structures is unknown, but evidence for offset on specific individual faults (including the EPGF in eastern Jamaica) are 10-40 km (Burke et al., 1980; Mitchell, 2003; Wadge and Draper, 1978). Reverse faults are also prevalent across the island, with predominantly NW-SE striking oblique slip faults serving as transfer faults between the strike-slip strands (e.g., (Wiggins-Grandison and Atakan, 2005). These faults are proposed to be reactivated from Paleocene to Eocene normal faults that bounded the Wagwater rift (Benford et al., 2014; Burke et al., 1980; Draper, 2008; Mann and Burke, 1984;1990). This history is recorded in the exhumed stratigraphic sequences of the Wagwater Belt, Montpelier-Newmark Trough, and John Crow Mountains (e.g. James-Williamson et al., 2014; Mann and Burke, 1990; Robinson, 1994) (Fig. 2a). Typical values of throw on the reverse faults in southwest are suggested to be 1-2 km (Benford et al., 2014).

Recent evidence for island-wide fault activity has been corroborated by multiple studies involving GPS (Global Positioning System), focal mechanisms, and paleoseismology. Geodetic data suggests the EPGF and Central Jamaican fault zone are the main strike-slip structures in Jamaica (e.g. Benford et al., 2012b; Koehler et al., 2013; Wiggins-Grandison and Atakan, 2005). The vector field of left-lateral motion of Jamaica relative to the Caribbean Plate increases from south to north, suggesting an elastic strain gradient that sums to ~7 mm/yr of total motion of the Gônave plate (Benford et al., 2012b; DeMets and Wiggins-Grandison, 2007). Multiple focal mechanism studies indicate variation of mean principal stress axes across the island (western Jamaica: greatest principal stress ~190^{o}, sub-horizontal; eastern Jamaica: greatest principal stress ~80^{o}, sub-horizontal), suggesting a complex fault-array with a heterogeneous upper crust

(Benford et al., 2012b; DeMets and Wiggins-Grandison, 2007; Van Dusen and Doser, 2000; Wiggins-Grandison, 2001; Wiggins-Grandison and Atakan, 2005). Although no major rupture has occurred in modern times, penetrative deformation across the island is evident based on historical seismic events, namely the 1692 Port Royal (estimated $M_w \sim 8.0$), the 1907 Kingston ($M_s \sim 6.5$), and 1957 Montego Bay ($M_w \sim 6.9$) earthquakes. While the ruptured faults responsible for these events remain unclear, recent paleoseismology studies along the EPGF suggests Holocene rupture in the past 500 years (Koehler et al., 2013). Furthermore, recent bathymetric studies provide evidence for active faulting along the EPGF in the Jamaican Passage, suggesting a significant portion of North American Plate motion (~2 cm/yr) must be accommodated by the EPGF (Corbeau et al., 2016a; Corbeau et al., 2016b; Leroy et al., 2015).

While these studies provide ample evidence for ongoing deformation in Jamaica, there is much debate about the total amount of vertical strain being accommodated within the BMRB. Benford et al. (2014) recently proposed a model for how strike-slip and reverse faults combine to accommodate plate motion across Jamaica based on GPS and gravity data. In their interacting-fault array model, the E-W striking Central Jamaican fault zone and South Coast fault zone act as transfer zones, with reverse motion affecting deformation close to the transfer zones. This model predicts that slip transfer between minor faults precludes the need for a major, through-going structure from E to W across Jamaica. The South Coast fault zone, however, has been suggested to be inactive during the Quaternary, and therefore may not contribute to the current overall strain pattern within this model (Koehler et al., 2013). Additionally, Benford et al. (2014) proposed that the low velocity gradient (1-2 mm/yr) across the Blue Mountains is related to the cumulative deformation occurring along the other restraining blocks between the Central Jamaican and South Coast fault zones, such that the BMRB is inferred to experience little active

contraction and rock uplift. The geodetic data, however, resolve vertical motion poorly, and rock uplift rates have not been measured.

Various studies have used the geomorphology and stratigraphy of Jamaica to infer uplift history, including the onset of island formation as well as the sequence of vertical deformation across the major tectonic blocks (Brown and Mitchell, 2010; Domínguez-González et al., 2015a; Fisher and Mitchell, 2012; James-Williamson et al., 2014; Mitchell, 2004;2013a;2016). Stratigraphic and geomorphic relationships of volcanic ash deposits overlying the island-wide carbonate platform, subsequently forming bauxite deposits, suggest that Jamaica was subaerially exposed by the middle Miocene (Comer et al., 1980). Supporting stratigraphic evidence of the onset of vertical rock uplift in Jamaica is recognized in the metamorphic and igneous clasts, derived from the Blue Mountains, found in the Coastal Group (middle? to late Miocene to Pleistocene) (James-Williamson and Mitchell, 2012; James-Williamson et al., 2014). Recent geomorphic investigations utilized hypsometric integral, stream profiles, and surface roughness to suggest a propagation of young topography from east to west, and interpret the Blue Mountains as an older, deeply incised landscape (Domínguez-González et al., 2015a). Although the deep incision of the Blue Mountains is evident based on slope distribution (Fig. 2c), the idea of the Blue Mountains as being inactive contradicts current models that eastern Jamaica is a more recently exhumed landscape. This study of topography does not take into account geologic data, however, such as important stratigraphic evidence that supports a young landscape in eastern Jamaica (Mitchell et al., 2015). Yet models cannot be tested without thermochronological data for the timing of rock uplift, and this data does not exist for the Blue Mountains or Central Jamaica (Domínguez-González et al., 2015b; Mitchell et al., 2015).

The erosive climate of Jamaica is another reason to expect rapid rock uplift along the BMRB. Jamaica is located at ~18^{o} N latitude within a tropical-marine climate, with the Blue Mountains receiving an average annual rainfall of ~250 cm/yr (e.g. Scientific Research Council of Jamaica, 1963; Tanner, 1980). The region is susceptible to infrequent major rainfall events driven by Atlantic cyclonic activity, with numerous documented landslide and mass wasting events (Ahmad et al., 1997; Northmore et al., 2000). In addition to high precipitation and prolonged high atmospheric humidity (80-90%; Tanner (1980)), mean annual temperatures in Jamaica are very warm (26 ^{o}C at sea level; Keeler (1979)). As a result, the BMRB is covered by a dense tropical rain forest, which persists due to active rainfall year round (Fig. 3) (Tanner, 1980). The dense vegetation (and associated organic-rich, acidic soil), high rainfall, and warm temperatures produce rapid chemical weathering of bedrock (Tanner, 1980). While bedrock exposure is localized within river channels and along stepper slopes, anthropogenic exposures of deeply weathered Late Cretaceous crystalline bedrock in central Jamaica display >30-m-deep, highly leached saprolite, with meter-thick soil profiles (Ahmad et al., 1997). The combination of heavy precipitation and rapid rock weathering, along with the potential for rapid tectonic uplift, seemingly should translate to rapid denudation, similar to what is observed in other similar settings, including Taiwan (e.g. Dadson et al., 2003), Papua New Guinea (e.g. Miller et al., 2012), and Puerto Rico (e.g. Bhatt and McDowell, 2007). These conditions also create challenges for bedrock sampling aimed towards geochronology (Fig. 3). Whether the climate enables a coupled erosion-tectonic system, and how this may affect transpressive deformation, are key questions we address in our investigations.

2.3.0 METHODS

2.3.1 Sampling strategy and sample processing

To constrain the exhumation history associated with transpression in eastern Jamaica, we collected 16 bedrock samples for low temperature thermochronometry (Fig. 4). Because the low-temperature cooling history of the region is unknown, our goal was to capture first-order cooling age patterns. Therefore, we collected samples from a broad region both across and along the axis of the BMRB, and sampled at localities spanning a wide range of elevations (Fig. 4). Samples were of variable lithology, but were generally not ideal for yielding apatite and zircon. The sampled lithologies included sandstone, volcanic (rhyolitic, dacitic, andesitic), conglomerate, gabbro, and several granitoids (Table 1). The major practical limitation was the difficulty in finding exposed relatively fresh bedrock (except for difficult-access river channels) in the densely vegetated and deeply weathered rocks of the Blue Mountains.

The majority of our data consists of AHe and ZHe ages, which are based on the radiogenic production and thermal diffusion of ^{4}He and record the age of exhumation through the upper ~2-8 km, corresponding to closure temperatures (T_c) of ~50-70 ^{o}C (AHe) and ~175-195 ^{o}C (ZHe) (Ehlers and Farley, 2003; Farley, 2000; Reiners, 2005; Reiners et al., 2004; Spotila, 2005; Wolf et al., 1996). The cooling ages are dependent on cooling history, geothermal gradient, crystal size and shape, and presence of radiation damage to the crystal lattice (Brown et al., 2013; Ehlers and Farley, 2003; Flowers et al., 2009). The techniques used for the higher temperature systems are discussed below.

Due to complications in sample quality and complex lithologies for finding datable minerals, we collected large (4-6 kg) bulk samples and applied standard mineral separation techniques. Samples were crushed and sieved to 80-280 μm, passed over a Wilfley table (density

separation), and further processed for apatite and zircon using standard magnetic and density separation techniques. In general, apatite and zircon yields and quality from these samples were poor, requiring multiple cycles of heavy liquid mineral separation and careful grain selection. Datable apatite was recovered from 13 samples, while datable zircon was recovered from only 6 samples. Optical petrography also showed that several samples had relatively unaltered potassium-bearing minerals. These samples were processed further at the U.S. Geological Survey, and optically pure mineral separates of amphibole and K-feldspar were obtained from sample JAM20. Powder x-ray diffraction of the K-feldspar separate showed that it was orthoclase (see supplement, Section 1). Pure mineral separates of sufficient mass could not be extracted from the other samples.

2.3.2 Data Collection

Apatite (U-Th)/He analyses were completed at Virginia Tech. Apatite grains were handpicked at 100x magnification. Selected grains typically had a diameter of > 60 μm (Table 1) and free of micro-inclusions. Multiple aliquots (average=5) of ~4-5 grains per sample, equaling to ~0.01 – 0.04 mg per aliquot, were used to determine the reproducibility for each sample age. In samples with limited apatite content, less pristine grains were dated and we relied on the reproducibility of multiple aliquots to reveal problems with sample quality (e.g. inclusions, zonation). Aliquots were placed in a platinum tubes and outgassed twice at 950 ºC for 20 minutes in a resistance furnace. The outgassed ^{4}He was spiked with ^{3}He and measured via isotope ratio using a quadrupole mass spectrometer. Low-gas threshold for the blank correction on this system is 0.02 fmol ^{4}He. Radiogenic parent isotopic measurements (^{238}U, ^{235}U, ^{232}Th, ^{147}Sm) were measured at the University of Arizona using isotope dilution via ICP-MS.

Cumulative error based on uncertainty of each individual measurement is expected to be 5% (1σ), although natural samples, including the Durango apatite standard, generally reproduce to about 10% (1σ).

Zircon (U-Th)/He ages were measured at the University of Arizona Radiogenic Helium Dating Laboratory (ARHDL). Samples were first handpicked, screened for inclusions, and photographed at Virginia Tech for grain morphology (only grains with terminated pyramids used), appearance, and grain size measurements (>60 μm wide for both *a* and *b* axes) (Table 2). Single grain aliquots were placed in niobium tubes, with >5 aliquots per sample for sedimentary rocks and 3 aliquots per sample for plutonic rocks. Helium was extracted from zircon by laser heating to 1000-1250 ^{o}C, with multiple heating cycles to ensure complete gas extraction (heating was terminated when successive cycles contained <1-2% of the total He content). The liberated gas was then spiked with ^{3}He and ^{4}He/^{3}He measurements were made by quadrupole mass spectrometry. Parent isotope (U-Th-Sm) measurements involve complete dissolution of the zircons within the Nb tubes using HF-HNO_3 in high-pressure digestion vessels and then analysis by isotope dilution ICP-MS. Zircon from the Fish Canyon Tuff was used as a standard (Reiners, 2005). The propagated uncertainty for typical zircons ages is approximately 1-3% (1σ). For detailed methodology see the ARDHL website (http://www.geo.arizona.edu/~reiners/arhdl/procs.htm).

Amphibole and orthoclase separated from JAM20 were irradiated for 30 hours at the U.S. Geological Survey TRIGA reactor in Denver, Colorado (Dalrymple et al., 1981). The irradiation flux was monitored with Fish Canyon sanidine (FCT-2, Cebula et al., 1986) with a preferred age of 28.02 Ma (Renne et al., 1998). CaF_2 and K_2SO_4 were also included to monitor interfering isotope production ratios (see supplement, Section 1). Following irradiation separates from

JAM20 were analyzed by the $^{40}Ar/^{39}Ar$ furnace step-heating method at the U.S. Geological Survey $^{40}Ar/^{39}Ar$ laboratory in Reston, VA. The samples were heated in 10-minute increments in a double-vacuum low-blank furnace (Staudacher et al., 1978) with a tantalum crucible and molybdenum liner. Evolved gasses were cleaned in a fully automated 2-stage extraction line prior to inlet to the mass spectrometer. The gasses were then analyzed in 6 cycles with a MAP 216 noble gas mass-spectrometer fitted with Johnston MM-1 electron multiplier and operated in the static mode. Data collection and analysis were done with MassSpec v. 7.9 (Deino, 2014) and details of the analytical methods used are given in McAleer et al. (2017).

Zircon U/Pb ages were measured via LA-ICP-MS at the University of Arizona in the LaserChron Center (ALC), following the methods of Gehrels et al. (2008). Two samples were dated using this technique (see supplement, Section 2). Single grain spot analyses were measured on 10 (JAM9) and 18 (JAM20) grains per sample in order to constrain uncertainties, and test the statistical fit between the measured ages and the standard. The LA-ICP-MS is coupled to a laser ablation system for precision and accuracy of ages, with the ages based on the isotope ratios of $^{206}Pb/^{238}U$, $^{206}Pb/^{204}Pb$, $^{206}Pb/^{207}Pb$, and $^{207}Pb/^{235}U$ (Gehrels et al., 2009; Gehrels et al., 2008). The ages are primarily tested against two standards: the Sri Lanka and Duluth gabbro zircons, yielding an ID-TIMS age of 563 ± 2.3 Ma (2σ) and 1099 ± 2 Ma (2σ), with a total uncertainty of 1-2% (Gehrels et al., 2008; Paces and Miller, 1993; Schmitz et al., 2003).

2.3.3 Data Analysis

Many workers have reported that the scatter in age of replicate analyses of apatite and zircon by the (U-Th)/He method typically exceed that expected based on analytical uncertainties (e.g. Ehlers and Farley, 2003; Farley, 2000; Reiners et al., 2004). The possible causes for age

dispersion are numerous including: micro-inclusions, parent element zonation, and radiation damage. Because these factors are difficult to assess *a priori* our approach was to date multiple aliquots and cull apparently spurious ages. Our data treatment is below but the complete dataset, including culled analyses, is presented in Tables 1 and 2.

The errors reported in Table 1 for average measured AHe ages are the standard deviation (1σ) from the mean. Prior to calculating mean ages, we culled from the data specific age determinations that were more than a factor of two greater or less than the mean age (determined in an iterative fashion). The culled age determinations consist almost entirely of ages that are anomalously old relative to other aliquots of the same sample (Table 1). The likely explanation for anomalously old AHe ages is the presence of excess radiogenic ^{4}He from undetected and insoluble micro-inclusions rich in U and Th (i.e. zircon). We expect this to be a problem because of the poor apatite quality of our samples. We measured a high number of replicates (n=5-8) in each sample to counter the problem of outliers and poor reproducibility. Despite this, several samples did not yield geologically plausible ages. Sample JAM1 had a reproducible mean age, but was older than basement crystallization ages. Sample JAM10 had extremely high age dispersion, from which a mean age would be meaningless. Sample JAM6 reproduced poorly and, even after culling apparent outliers, had a mean age that exceeded the ZHe age for the same sample. Although we do not know the reasons why these three samples reproduced so poorly and yielded such old ages, we suspect there may be problems with the sample quality and do not consider them in our interpretations. From the remaining 13 samples, a total of 15 age determinations were culled as outliers, or 22% of the total data set. Two of these samples (JAM4 and JAM15) had limited apatite content and therefore only few age determinations, which we regard as poorly constrained. The mean reproducibility of these 13 samples was 25% (2σ). This

reproducibility exceeds that from other recent AHe studies using non-ideal lithologies from our laboratory (e.g. Spotila and Berger, 2010; Fame et al., in review; Tranel et al., 2011; Valentino et al., 2016), likely an expression of even worse sample quality.

Errors reported on Table 2 for average measured ZHe ages are also the standard deviation of replicate analyses. The average standard deviation for ZHe ages was 12% (1σ). This average was calculated after several individual age determinations were culled from the data set (n=8, 32% of total). Because of the lower number of replicate analyses for ZHe ages, we used a lower threshold for classifying anomalous age determinations ($\pm$50% of the mean age) in comparison to the AHe dataset. Several mean ZHe ages are based on only two age determinations and should be viewed as poorly constrained (JAM16, JAM20).

Complete isotopic data for the $^{40}Ar/^{39}Ar$ and U/Pb analyses are presented in the supplement. For the $^{40}Ar/^{39}Ar$ analyses single-step age uncertainties are plotted at 1σ (see supplement, Section 1) and plateau, isochron, and weighted average ages are reported at 2σ. A $^{40}Ar/^{39}Ar$ plateau age is reported where contiguous steps agree at the 95% confidence level and contain >50% of the $^{39}Ar_K$ (Fleck et al., 1977). An inverse isotope correlation age is reported if contiguous steps containing >50% of the $^{39}Ar_K$ yield a regression line with an MSWD (mean standard weighted deviation) < 2.5. Contiguous steps in the age spectrum for orthoclase for JAM20 do not meet the statistical criteria for a plateau age. Nevertheless, the spectrum is relatively flat, and the structural state of the feldspar indicates it cooled rapidly. Therefore, we report a weighted average age for a subset of steps that include > 90% of the $^{39}Ar_K$. Errors associated with the U/Pb are given as 2σ, ignoring the uncertainty in decay constants. The probability of concordance ranges from 0.13 (JAM9, n=9) - 0.98 (Jam20, n=17), and the MSWD ranges from 2.3 (JAM9) – 0.00087 (JAM20) (see supplement, Section 2). A probability density

function indicates each sample reproduced well, with zero rejected ages, and suggests each age is tightly constrained (see supplement, Section 2).

2.3.4 Thermal History

Sample cooling histories were modeled using the age data and closure temperatures for the various isotopic systems. For AHe ages, closure temperatures were calculated following Dodson (1973), using the apatite diffusion properties of Farley (2000) and each sample's grain size and estimated cooling history (performed iteratively). Given a lack of age correlation with eU and young cooling ages, we did not take potential radiation damage into account for calculating AHe closure temperatures. Resulting closure temperature (T_c) for AHe ages varied from 52-80 ^oC. For ZHe we assume that the T_c is 110 ^oC greater than the respective AHe T_c calculated for all 6 samples (e.g. Reiners, 2005; Reiners et al., 2003). Given the apparent rapid cooling from high temperature for these rocks (see Results) we use a T_c of ~550±50 ^oC for the diffusion of argon in amphibole (e.g. Baxter, 2010; McDougall and Harrison, 1999) and a T_c of ~350±50 ^oC for the diffusion of argon in orthoclase (Baxter, 2010). The U/Pb zircon ages are interpreted to reflect their time of crystallization.

To compare the AHe and ZHe systems, pseudo-elevation-age plots were constructed, assuming a difference in AHe-ZHe closure temperature of 110 ^oC, an assumed geothermal gradient of 30 ^oC (Simon-Labric et al., 2013), and a resulting AHe closure depth of 2 km. This approach shifts the elevation of ZHe samples upwards proportionate to the difference in closure temperature, in this case by 3.7 km (Reiners et al., 2003). We also used an ambient surface temperature of 26 ^oC at sea level (Keeler, 1979) and a lapse rate of 5 ^oC/km for calculations. Exhumation rates were estimated using these parameters and the calculated AHe closure

temperatures. Potential perturbations of isotherms due to heat advection in rapidly exhuming crust were not accounted for using thermo-kinematic models, given the modest relief and narrow width of the BMRB (Braun, 2002; Braun et al., 2012; Ehlers and Farley, 2003). Because of the uncertainty in measured AHe ages, the poorly constrained geothermal gradient, and the lack of thermo-kinematic modeling, our exhumation estimates should be considered as first-order approximations.

Thermal histories of samples with multiple dated mineral systems were modeled using HeFTy software (Ketcham, 2005a;b). This was performed to obtain tighter constraints on the timing of changes in cooling rate (e.g. onset of rock uplift) and more accurate estimates of Neogene cooling rates related to orogenic exhumation. HeFTy computes the predicted (U-Th)/He cooling ages for our forward models using the helium production and diffusion equations for diffusion and ejection parameters for respective minerals (Farley, 2000; Ketcham et al., 2011; Reiners et al., 2004). Forward models are constrained by existing data, including known time-temperature points from geologic information or other geochronometers, and well as initial hypotheses for how samples cooled. Results from forward models are used as a guide for setting constraints in inverse modeling. Based on our forward model parameters (i.e. T-t for each thermochronometer), inverse models using Monte Carlo analysis (n=10,000-50,000 runs) were generated until 100 good-fit paths and a goodness-of-fit over 80% was obtained. If 100 good-fit paths were not found, then the model ran until 100 acceptable paths were estimated, to estimate all possible cooling histories fitting to the defined constraints. These models statistically identify the quality of fit of different scenarios of the measured ages. We modeled cooling histories using this method for four samples (JAM9, 11, 19, and 20) based on specific criteria, including having

multiple thermochronometers per sample and geographic location (i.e. widespread lateral and vertical distribution).

2.4.0 RESULTS

Our results provide the first quantitative constraints on the low-temperature cooling history of Blue Mountains arc basement rocks, including the timing of onset and rate of rapid Neogene exhumation-associated transpression along the EPGF. Data also provide first-order constraints on the pattern of exhumation across the restraining bend, including three general zones: the core of the BMRB north of the EPGF (eight samples along our vertical transect), the BMRB periphery (two low-elevation sedimentary samples and two low-elevation plutonic samples), and the Wagwater Belt (two samples south of the Blue Mountains-Yallahs faults).

Well-constrained AHe ages from the BMRB are generally young, ranging from ~1 to 6 Ma (Table 1, Fig. 4), but with several exceptions, including samples that did not produce meaningful ages (JAM1, JAM6, and JAM10, as discussed above). Several samples along the peripheral eastern and western flanks of the BMRB are also somewhat older; JAM17 (6 Ma) and JAM15 (10 Ma) (Fig. 4). One sample from within the Wagwater Belt yielded an older age (JAM13; 30 Ma), but this sample is volcanic and the AHe age may have been only partially reset after the eruption (i.e. would yield an old age but not as old as the youngest volcanism in Jamaica (early Eocene)). Aside from these exceptions, the young (1-6 Ma) ages occur throughout the core of the BMRB, indicating significant late Cenozoic exhumation. This includes samples on both sides of the EPGF (i.e. JAM12, 2 Ma, occurs in the footwall; all other samples are in hangingwall), suggesting complex kinematics of rock uplift for the BMRB (Fig. 4). Rapid late Cenozoic exhumation in the BMRB is supported by a rough AHe age-elevation relationship,

which implies an exhumation rate of 0.3 mm/yr. This exhumation rate, however, is most likely faster based on closure depth of the youngest sample, where exhumation rate is estimated to be as high as 2 mm/yr (see discussion below) (Fig. 5a). An AHe age of ~5 Ma at Blue Mountain Peak (2256 m), coupled with the relatively steep and continuous slope on the age-elevation plot, demonstrate that no partial retention zone is retained near the crest of the range, suggesting relatively continuous rapid rock uplift (e.g. Fitzgerald et al., 1993).

Measured ZHe ages range from 15-44 Ma and are consistently older than AHe and younger than higher temperature systems (Table 2). ZHe ages from the core of the Blue Mountains define an age-elevation gradient of 0.20 mm/yr (Fig. 5b), based on weighting of errors associated with each sample (i.e. JAM6 is weighted less due to large uncertainty in reproducibility). This gradient suggests moderate exhumation rate in the early Miocene, slightly slower than the younger rate defined by the AHe age-elevation gradient. ZHe ages from the northern flank of the BMRB are considerably older (35-44 Ma) than in the core of the range (14-20 Ma), which contrasts with similar AHe ages in both regions. This implies that while recent exhumation may have been comparable in these areas, earlier exhumation may have been of lower magnitude on the range flanks.

Ages from higher temperatures systems were obtained from 2 samples. Amphibole from JAM20 (northern Blue Mountains) yielded a plateau age (Fleck et al., 1977) of 71.7 ± 1.0 Ma and an inverse isotope correlation age of 70.8 ± 1.4 Ma (see supplement, Section 1). These ages are slightly older than the U/Pb zircon age from the same sample (68.1 ± 0.7 Ma, see supplement, Section 2), although nearly overlapping at 2σ. Because optical petrography shows evidence for retrogression (e.g. biotite is nearly completely replaced by chlorite) and because the amphibole is very low in K (see supplement, Section 1; K/Ca < 0.02), we suggest that a minor

component of excess argon has affected the amphibole (McDougall and Harrison, 1999), and that the U/Pb age more closely approximates the emplacement age. Orthoclase from JAM20 also yielded a flat age spectrum with a weighted average age of 67.9 ± 1.2 Ma (see supplement, Section 1) overlapping with the U/Pb age. The similar age of the zircon U/Pb and $^{40}Ar/^{39}Ar$ orthoclase ages, and the lack of evidence for subsolidus transformation to microcline are strong evidence for rapid post-emplacement cooling in the Late Cretaceous and likely reflects shallow emplacement of this unit. Zircon U/Pb from JAM9 confirms the Cretaceous age of the suite with a produced concordia age of 74.9 ± 0.8 Ma (see supplement, Section 2), despite being mapped as the same pluton as JAM20 (Krijnen and Chin, 1978). Taken together, these represent additional age constraints for formation of the Blue Mountains arc-suite in the Late Cretaceous.

2.5.0 DISCUSSION

2.5.1 Cooling History and Pattern of Rock Uplift

Based on our crystallization and cooling ages, the volcanic-arc rocks of the BMRB have undergone three phases of cooling since formation in the Late Cretaceous (Fig. 6). The U/Pb ages for plutonic rocks suggest crystallization in the Late Cretaceous, consistent with a whole rock age (80 Ma) for a granodiorite near the town of Bath in the southeastern Blue Mountains (Wadge et al., 1982). The $^{40}Ar/^{39}Ar$ ages also reveal Late Cretaceous cooling down to <350 ºC and suggest shallow emplacement of these plutons. Using the $^{40}Ar/^{39}Ar$ orthoclase age and the youngest ZHe age implies a ~55 Ma period of slow cooling at an average rate of ~6 ºC/km throughout much of the Cenozoic. This is consistent with Eocene to Miocene carbonate platform development due to post-rift thermal subsidence in what has been termed the “quiescent phase” of Jamaican tectonics (Mann and Burke, 1990; Mitchell, 2004). Along the southern flank of the

Blue Mountains, peak metamorphism in the Westphalia and Mt. Hibernia schists was followed by exhumation and subsequent burial metamorphism as a result of Paleocene to early Eocene rifting (West et al., 2014). Our $^{40}Ar/^{39}Ar$ ages do not record a period of resetting due to burial metamorphism, perhaps because our samples lie on the upthrown-side (i.e. north) of the reactivated normal faults associated with the Paleocene to Eocene rifting event, and were not influenced by subsidence (Fig. 4). Prolonged stasis from 70 – 20 Ma following rapid cooling from 74 – 68 Ma is generally consistent with data from farther to the west, where the Green Bay schist suite experienced this "subsiding" phase from 50 – 20 Ma (Abbott et al., 2016).

The late Cenozoic cooling history is illustrated by the composite age-elevation profile of AHe ages and shifted ZHe ages from our vertical transect. This plot suggests two periods of exhumation: an earlier phase of ~0.2 mm/yr from 20-6 Ma, and a more rapid phase of exhumation of ~0.8 mm/yr from 6-0 Ma (Fig. 7). This is only a first-order approximation, and there is a range of possible exhumation rates which fit the data, increasing to as high as 2 mm/yr for the youngest stage directly adjacent to the EPGF. Nonetheless, the age-elevation relationships indicate a break-in-slope at about 6 Ma. This is the first quantitative evidence within the BMRB to suggest two separate phases of exhumation since the late Miocene.

Thermal modeling using HeFTY provides a more robust estimate of cooling history (Fig. 8a-c). Inverse models were run after prescribing specific constraints from the higher temperature cooling ages. An earlier phase of crystallization and subsequent rapid cooling was constrained using the U/Pb and $^{40}Ar/^{39}Ar$ ages (74 -68 Ma) from the plutonic samples (see supplement, Section 1-2). The early cooling phase for JAM19 is less constrained, since this sandstone (Cretaceous) likely had a much lower maximum burial temperature (Fig. 8c). Using these initial constraints, several inverse models for each sample were run using an iterative approach,

changing the size of T-t constraints at each node where age data exist. The modeling results are similar to the closure temperature approach, and reveal several consistent predictions for the later cooling phase. Model results for samples from the vertical transect (JAM9 and JAM11) suggest this phase occurred in two stages, starting with an initial stage of exhumation from ~20-5 Ma, with average cooling rates between 5-10 ^{o}C/Ma (Fig. 8a-b). Based on an assumed geothermal gradient of 30 ^{o}C/km, these cooling rates correspond to exhumation rates of ~0.15-0.3 mm/yr. The models reveal a second stage of exhumation beginning between 5-2 Ma and lasting until present-day, at an overall faster cooling rate of 20-50 ^{o}C/Ma. This cooling corresponds to exhumation rates of ~0.7-1.7 mm/yr. The modeling results from JAM19 are less clear, but that model does suggest an increase in exhumation rate at ~8 Ma (Fig. 8c). The other sample modeled, which lies on the northern flank of the BMRB (JAM20), shows a somewhat different cooling history. This sample's most recent stage of recent exhumation doesn't begin until ~3 Ma (Fig. 8d), corresponding to an exhumation rate of ~1 mm/yr. This later onset and slower exhumation may result from JAM20's greater distance (> 15 km) from the EPGF. Regardless of minor discrepancies, the inverse models indicate a two-stage exhumation history since the late Miocene, with exhumation rates up to ~1-2 mm/yr (both the northern and southern flanks) since the Miocene to Pliocene and lasting until the present day.

The results also provide constraints on the pattern of rock uplift associated with the BMRB. The lack of variation in AHe ages between the northern and southern flank of the range suggests a uniform exhumation pattern and whole-block rock uplift (i.e. entire hangingwall of the BMRB), consistent with no major range-bounding fault north of the EPGF (Benford et al., 2012b). This is illustrated in the relatively flat isochrons of young AHe ages along a south-north transect across the range (Fig. 9a). Older ages on the periphery of the BMRB suggest

exhumation tapers off outside of the core of the BMRB, depicting a pattern of rock uplift centered where the right-stepping Blue Mountains restraining bend attains its greatest fault curvature along the eastern flank of the Wagwater belt. That the ZHe data do not show this pattern, but instead show ages becoming steadily older northwards across the range (Fig. 9b), implies that the northern flank experienced a different pattern of (as well as slower) exhumation from ZHe closure to AHe closure. Given the uncertainty in these age determinations and the spacing of samples, the pattern of rock uplift is approximate, and there may be details that cannot be resolved with the existing data. One possible detail is the apparent alternating pattern between younger and older AHe ages along the southern flank, including samples JAM9 (3.4 Ma), JAM18 (6.4 Ma), JAM4 (3.5 Ma), and JAM19 (5.2 Ma). This pattern would suggest fold structures along the southern flank of the Blue Mountains (Fig. 9a). Another possibility is that isochrons may tilt upwards directly along the EPGF over the youngest age, as a result of increased rock uplift adjacent to the fault. Furthermore, detailed geologic maps within the Blue Mountains core misrepresent some geological units and cannot be interpreted at depth. Our data do not yet warrant analyses of fault geometry, geological offset, and structures within the BMRB. In order to delineate detailed structures related to the transpressive deformation, however, higher spatial and temporal resolution of thermochronometric data is required.

2.5.2 Tectonic Interpretations

The early phase of cooling evident in the thermochronometric results are consistent with current models of Jamaica and the tectonic framework of the Caribbean. Crystallization and rapid cooling of plutonic basement can be attributed to arc-related volcanism and northward subduction along the Great Caribbean Arc. Plate reconstruction and tectonic models suggest that

Jamaica collided with the arc in late Campanian to early Maastrichtian (~75-70 Ma) along a N-NE dipping subduction zone, and subsequently translated along the northern North American-Caribbean Plate boundary (Hastie et al., 2010; Pindell et al., 2012). The crystallization of the plutonic basement in the late Campanian to middle Maastrichtian (74-68 Ma) post-dates the formation of the Caribbean Large Igneous Province (~90 Ma; (e.g. Kerr et al., 1997; and references therein), implying that plutonic stocks were feeding arc-volcanism during the initial stages of Jamaica colliding with the Great Arc (Pindell et al., 2012). Evidence for widespread plutonism is visible in other Cretaceous suites across Jamaica. For example, east of the Central Inlier (Fig. 3), the Above Rocks and Flint River granodiorites have been dated at 63 Ma and 75 Ma, respectively (Chubb and Burke, 1963; Mitchell, 2003;2013a). After crystallization of the granitic plutons, cooling through the orthoclase $^{40}Ar/^{39}Ar$ closure temperature in ~5 Ma suggests rapid cooling and therefore shallow pluton emplacement. This model is consistent with subduction and subsequent exhumation of the Mt. Hibernia and Westphalia Schists from 78 - 66 Ma (West et al., 2014), and could be related to uplift between the Chortis block and the Great Arc (Sanchez et al., 2016).

Following volcanic-arc formation and associated metamorphism, several inverted rift deposits across the island (i.e. Wagwater Belt, John Crow Mountains, Montpelier-Newmark Trough) record a regional rifting phase which exposed the metamorphic rocks to erosion in the early Paleocene to Eocene (e.g. Mann and Burke, 1990; West et al., 2014). Although West et al. (2014) $^{40}Ar/^{39}Ar$ ages record this event within the Westphalia and Mt. Hibernia schists, our plutonic $^{40}Ar/^{39}Ar$ ages do not record this rifting phase. The absence of the rifting event may be attributed to sample distribution, or structural position relative to the inverted normal faults associated with this event (i.e. lie north on the upthrown-side of these structures). The tectonic

quiescence following Jamaica's rifting phase suggested by our data is also consistent with prevailing geologic models for Jamaica. Island-wide deposition of nearly 3 km of carbonate (Yellow and White limestone formations) suggests post-rifting thermal subsidence as a result of lithospheric cooling (Benford et al., 2014; Draper, 2008; James-Williamson et al., 2014; Mitchell, 2004). The formation of the carbonate platform, as well as the onlapping of Wagwater rift deposits (e.g. Richmond Fm.), provide an important stratigraphic marker for estimating total thickness of eroded material from the Blue Mountains region. Furthermore, the deposition of volcanic ash in the late to middle Miocene and subsequent bauxite formation suggests the carbonate platform was subaerially exposed by this time (Comer et al., 1980). This was the beginning stages of Jamaica's emergence as an island, and is consistent with late Miocene ZHe ages.

Existing tectonic models suggests that Neogene transpression between the leading edge of the Caribbean plate and the Bahamas escarpment resulted in the formation of the Gônave microplate and EPGF system (e.g. Benford et al., 2014; Draper, 2008; Mann et al., 1995). This appears to match the stages of exhumation indicated by lower temperature thermochronometry. ZHe and AHe ages indicate two stages of exhumation within the Miocene. The ZHe data suggests that the northern and southern flanks of the BMRB experienced different cooling histories. Younger ZHe ages in the south are consistent with onset of exhumation of ~0.1 – 0.3 mm/yr at ~20 Ma, while the older cooling ages and associated thermal models for the northern samples do not. Onset of exhumation at 20 Ma in the south is consistent with stratigraphic ages of the August Town formation, where metamorphic clasts indicate subaerial exposure by ~11 Ma (James-Williamson et al., 2014). The discrepancy between the 20 Ma onset of slower exhumation and the subaerial exposure of arc-rocks at 11 Ma may be the result of partial erosion

of the entire suite of White and Yellow limestone cover (i.e. the basement was being exhumed but was not exposed until the middle Miocene). Additionally, during this stage there was a significant decrease in spreading rate along the Cayman Ridge (~25 Ma by > 15%) (Rosencrantz et al., 1988), which could have forced Jamaica into a state of compressional stress, resulting in localized vertical strain within the upper crust without actual onset of strike-slip or transpression along the EPGF.

As illustrated by the AHe and thermal models across the BMRB, exhumation accelerated in the late Miocene to Pliocene (7-5 Ma), and can be attributed to the formation of the Gônave microplate, onset of the EPGF as a main-bounding fault between the North America and Caribbean Plates, and the shortening of the crust within the restraining bend (Benford et al., 2014; James-Williamson et al., 2014; Mann et al., 2002). Major plate kinematic reorganization took place during this time as a result of collision and subduction of the Bahamas Platform with the leading edge of the Greater Antilles Arc (Mann et al., 2002). This tectonic event caused thrusting south of Hispaniola along the Muertos trench, initiating transpressive strike-slip motion along the EPGF (Mann et al., 2002). As slip propagated along the EPGF from east to west, the fault converged with pre-transpressional NW-SE normal faults, reactivating them into thrusts and creating the right-stepping BMRB. Assuming a slip rate based on the modern GPS estimate of 5-7 mm/yr (Benford et al., 2012b; DeMets and Wiggins-Grandison, 2007), the total strike-slip offset on the EPGF since inception has been 35-50 km. This implies that much of the crust now in the BMRB once laid offshore to the east, while crust that should have experienced transpressive deformation in the core of the BMRB has been advected tens of kilometers to the west. This model is consistent with stratigraphic evidence suggesting a tectonic loading and subsidence of the southeastern Jamaican shelf (James-Williamson et al., 2014), yet deviates

somewhat from the model proposed by Domínguez-González et al. (2015a). Thermochronometry implies that rapid exhumation and rock uplift are ongoing in the core of the BMRB, whereas Domínguez-González et al. (2015a) interpreted the Blue Mountains to be an older uplift with active rock uplift migrating westward.

The young AHe ages suggest that the BMRB is a major active tectonic element in the strike-slip kinematics across Jamaica. AHe ages suggest exhumation of ~1 mm/yr across much of eastern Jamaica. This implies that a significant fraction of plate motion is being accommodated by thrusting and associated rock uplift in the BMRB, particularly given that the strike-slip motion accommodated in the bend is a maximum of only 5-7 mm/yr (the entire rate of the Gônave plate) or may be as little as 2-3 mm/yr (based on block modeling of Benford et al. (2012b). While a portion of this motion may be attributed to translation on the EPGF itself, some may also occur on unmapped thrust faults or be distributed across the BMRB. Rock uplift extending to the northern flank of the range implies that a bounding thrust fault should occur along the northern shore (see fault maps in Burke et al. (1980); James-Williamson et al. (2014)). Leroy et al. (1996) suggests that the northern slopes of Jamaica are part of a positive-flower structure of the North Jamaican fault zone, which could help drive rock uplift within the restraining bend. The young AHe age (2 Ma) in the footwall of the BMRB to the south implies that rock uplift propagates across the main bounding fault and requires deformation along the reactivated normal faults bounding the Wagwater rift (i.e. Wagwater and Blue Mountains-Yallahs faults) (Mann and Burke, 1990). Evidence for compression is also visible in folding across Long Mountain near Kingston (Draper, 2008) (Fig.3). AHe ages also suggest that rock uplift may be concentrated along the EPGF in the southern BMRB, where exhumation rates may be as high as 2 mm/yr. A zone of focused uplift could correspond with an area of rapid erosion,

as indicated by the knickzones, gorges, and fault-parallel stream flow along the southern Blue Mountains, as well as focused strain near the bounding structure. This interpretation that the BMRB is a major active transpressive zone of a comparable scale to restraining bends along other major strike-slip faults in the world is in contrast to recent models that suggest it is only a minor or even inactive component of deformation in Jamaica (Benford et al., 2014).

2.5.3 Implications for Transpression

Thermochronometry suggests significant late Cenozoic exhumation has occurred in the BMRB. ZHe ages, the lack of a preserved AHe partial retention zone atop the Blue Mountains, and the apparent exhumation rate based on AHe ages, suggest the total exhumation in the BMRB since onset at 5-7 Ma has been at least ~3 km of Yellow and White Limestone, with a more likely value of ~5-7 km based on unconformable contacts between the White Limestone and younger units (James-Williamson et al., 2014). The present-day topography of the Blue Mountains implies there has been an additional ~2 km of surface uplift in the same time frame. The resulting magnitude of rock uplift (7-9 km) is significant. Whether considering this from a crustal volume perspective, or from the perspective of implied shortening rates along NW-SE reverse faults, this rock uplift likely implies a comparable magnitude of horizontal shortening is being accommodated across the main thrust (i.e. Blue Mountains-Yallahs fault). If accurate, this implies that vertical strain has accommodated 15-25% of the total transform plate motion across Jamaica since the late Miocene. Given the plate motion obliquity across the EPGF ($\alpha > 20^{o}$) in the restraining bend (Fig. 3), we suggest that the BMRB should be classified as pure-shear-dominated with a high percentage of deformation partitioned into vertical strain and distributed

across a wide zone (i.e. not focused only along the EPGF), as in the context of Teyssier et al. (1995).

In contrast, other transpressive strike-slip systems tend to be less efficiently partitioned. For example, the ratios of uplift rate to strike-slip rate in the northern San Gabriel Mountains and southern San Bernardino Mountains, two pure-shear-dominated locations along the San Andreas fault in southern California, are only ~0.02 and ~0.06 (Buscher and Spotila, 2007; Spotila et al., 2001), relative to 0.15-0.25 in the BMRB. This suggests that something (e.g. climate, scale, fault dip, fault-array geometry) makes slip partitioning more efficient in the BMRB. High erosivity is an obvious hypothesis for why transpressive deformation is also efficient along the BMRB, given the heavy annual precipitation and observations of rapid weathering, high slopes, incision, and mass wasting across the Blue Mountains.

Another apparent difference between the BMRB and transpressive centers in less erosive, arid settings, is the lack of a gradient in rock uplift (i.e. AHe ages) away from the fault zone. Spotila et al. (2007a) found that rock uplift increased in the near field (< 10 km) within transpressive zones along the San Andreas fault. This was corroborated by Niemi et al. (2013), identifying a sharp gradient (~ 3 Ma/km) in AHe ages away from the trace of the San Andreas fault in the San Emigdio Mountains. This gradient was interpreted as reflecting concentrated zone of rock uplift along the fault and strong crustal tilting away from the fault. Although AHe ages are slightly younger near the EPGF in the BMRB, ages are young across the entire region, exhibiting only a slight northward tilt away from the EPGF (Fig. 9). This pattern implies that rapid rock uplift may be maintained across a broader zone as a result of the presumably more efficient erosion in Jamaica's tropical setting, or unmapped reverse structures either on- or offshore.

A final unique aspect of the BMRB is the concentration of topography within the fault bend itself. At other, similarly sized restraining bends, zones of rock uplift and high relief often trail off from the center of restraining bends in one or both directions, as zones of uplift are subsequently advected laterally by strike-slip motion on the master fault. An excellent example of this occurs in the Santa Cruz Mountains along the San Andreas fault (Anderson, 1990; Bürgmann et al., 1994). The lack of a trailing, tapering zone (i.e. gradient) of concentrated rock uplift away from the center of the BMRB (i.e. to the west) may result from rapid exhumation (Fig. 2). The combination of erosion and chemical denudation may be sufficiently rapid that mountainous topography is eroded once out of the zone of tectonic rock uplift. Globally, variation in erosion rates (i.e. climatic forcing) heavily impacts the topographic expression within the bend itself, and has been suggested to dictate both the scale (i.e. length to width ratio) and the fault-propagation pattern within restraining bends (e.g. Cunningham, 2007; Mann, 2007).

That climatically induced erosional efficiency in Jamaica may impart influence on deformation patterns is consistent with the extensive, mounting evidence for coupling between climate and tectonics (Koons, 1995; Malavieille, 2010; Whipple, 2004; Willett, 1999). In this context, the active tectonics of the BMRB and Jamaica in general may be comparable to the highly erosive, maritime settings such as Taiwan or Papua New Guinea, each of which experience several meters per year of precipitation, are heavily vegetated, and tropical or subtropical with rapid chemical weathering and denudation (Dadson et al., 2003; Miller et al., 2012). Similar to these areas, the Blue Mountains of the BMRB may be at erosional steady-state, in which the topography is maintained and all incoming tectonic rock flux is efficiently accommodated via erosional efflux, a condition commonly invoked for orogenic wedges (Burbank et al., 1996; Whipple and Meade, 2004; Willett et al., 2003). The low variance of AHe

ages over the entire BMRB, the rapid exhumation rates, and the uniform influence of precipitation by the easterly trade winds (i.e. there is no wet-dry side of the range), suggest a possible erosional steady-state for the BMRB (Spotila, 2005). This implies that convergent orogenic wedges may not be the only setting to attain such a climatically-induced balance of tectonics and erosion, but rather that this may also be attained in the moderate-uplift setting of a strike-slip restraining bends (e.g. Cunningham, 2007; Mann, 2007). A final implication is the dimensions and relief of transpressive mountain ranges in tropical settings may be misleading, and that without thermochronometric constraints major zones of rock uplift may be overlooked.

2.6.0 CONCLUSIONS

Our results provide first-order constraints on the thermal history within the Blue Mountains restraining bend, beginning with crystallization of the island arc-related plutonic rocks as part of the Great Arc of the Caribbean in the Late Cretaceous, and continuing through two pulses of exhumation in a left-lateral restraining bend setting during the middle Miocene to Recent. These results were obtained from extensive replicate measurements ($n \geq 5$) of poor quality apatite and zircon grains. Crystallization and high-temperature cooling ages suggests rapid, shallow emplacement of plutons into the lower crust in the Late Cretaceous (75-68 Ma) during subduction along the Great Caribbean Arc (e.g. Neill et al., 2011). New AHe and ZHe ages suggest two stages of rock uplift; a slower (~0.2 mm/yr) stage beginning as early as the early Miocene (~20-6 Ma), and a more rapid (~1-2 mm/yr) stage beginning in late Miocene (~6 Ma-Present). While young AHe ages across the Blue Mountains indicate whole-scale rock uplift across a wide zone (> 30 km) of distributed deformation, disparity in ZHe ages along the northern (34 – 44 Ma) and southern (14 – 19 Ma) flanks is likely a consequence of the ~10 – 15

km distance between the sample locations, and the temporal differences of the lithosphere advecting into the bend itself. Based on the local stratigraphy, a minimum of ~5 km has been eroded from the Blue Mountains since the island emerged in the late Miocene. Given the present-day 5-7 mm/yr Gônave plate velocity, the ~1-2 mm/yr rates of rock uplift represent a major percentage of overall plate motion. We hypothesize the efficiency of transpressional partitioning into vertical deformation is greatly influenced by climatically-induced erosivity, with the Blue Mountains potentially within an erosional steady-state. Despite similarities in obliquity and plate velocity with other transpressional systems, the BMRB is significantly more efficient at accommodating rock uplift due to climatic forcing on this restraining bend system.

2.7.0 ACKNOWLEDGEMENTS

We thank Barrett Adventures for providing transportation and hospitality during field work. We thank Michelle Fame and Josh Valentino for helpful discussion and assistance with sample preparation and processing. We would like to thank Sarah Mazza for analyzing and providing helpful discussion regarding our U-Pb samples. We thank the Geological Society of America for support through graduate student grants and other GSA funds. We thank reviewers' Simon Mitchell and Paul Mann for the constructive comments and suggestions. Any use of trade, firm, or product names is for descriptive purposes only and does not imply endorsement by the U.S. Government.

2.8.0 REFERENCES

Abbott, R. N., Jackson, T. A., and McSween, H. Y., 2010, Metamorphic Conditions in the Westphalia Schists of the Blue Mountain Inlier, Jamaica: Tectonic Implications: International Geology Review, v. 38, no. 12, p. 1143-1154.

Abbott, R. N., West, D. P., Jr., Bandy, B. R., and McAleer, R. J., 2016, Petrology and tectonic history of the Green Bay Schist, Portmore, St. Catherine Parish, Jamaica: Caribbean Journal of Earth Science, v. 48, p. 1-18.

Ahmad, R., Clark, J., Hellin, J., Manning, P. A., and McDonald, M., 1997, The potential of bio-engineering in slope stabilization: a case study from Jamaica, *in* Ahmad, R., ed., Natural hazards and hazard management in the Greater Caribbean and Latin America, Volume 3: Kingston, Jamaica, Unit for Disaster Studies, Department of Geology and Geography, Unv. of West Indies, p. 235.

Anderson, R. S., 1990, Evolution of the Northern Santa Cruz Mountains by Advection of Crust Past a San Andreas Fault Bend: Science, v. 249, no. 4967, p. 307-401.

Arden, D. D., 1969, Geologic History of the Nicaraguan Rise: Transcripts of the Gulf Coast Association of Geological Society, v. 19, p. 295-309.

Baxter, E. F., 2010, Diffusion of Noble Gases in Minerals: Reviews in Mineralogy and Geochemistry, v. 72, no. 1, p. 509-557.

Benford, B., DeMets, C., and Calais, E., 2012a, GPS estimates of microplate motions, northern Caribbean: evidence for a Hispaniola microplate and implications for earthquake hazard: Geophysical Journal International, v. 191, no. 2, p. 481-490.

Benford, B., DeMets, C., Tikoff, B., Williams, P., Brown, L., and Wiggins-Grandison, M., 2012b, Seismic hazard along the southern boundary of the Gônave microplate: block modelling of GPS velocities from Jamaica and nearby islands, northern Caribbean: Geophysical Journal International, v. 190, no. 1, p. 59-74.

Benford, B., Tikoff, B., and DeMets, C., 2014, Interaction of reactivated faults within a restraining bend: Neotectonic deformation of southwest Jamaica: Lithosphere, v. 7, no. 1, p. 21-39.

Benowitz, J. A., Layer, P. W., Armstrong, P., Perry, S. E., Haeussler, P. J., Fitzgerald, P. G., and VanLaningham, S., 2011, Spatial variations in focused exhumation along a continental-scale strike-slip fault: The Denali fault of the eastern Alaska Range: Geosphere, v. 7, no. 2, p. 455-467.

Bhatt, M. P., and McDowell, W. H., 2007, Controls on major solutes within the drainage network of a rapidly weathering tropical watershed: Water Resources Research, v. 43, no. 11, p. n/a-n/a.

Bourne, S. J., England, P. C., and Parsons, B., 1998, Themotion of crustal blocks driven by flowof the lower lithosphere and implications for slip rates of continental strike-slip faults: Nature, v. 391, p. 655-659.

Braun, J., 2002, Quantifying the effect of recent relief changes on age-elevation relationships: Earth and Planetary Science Letters, v. 200, p. 331-343.

Braun, J., van der Beek, P., Valla, P., Robert, X., Herman, F., Glotzbach, C., Pedersen, V., Perry, C., Simon-Labric, T., and Prigent, C., 2012, Quantifying rates of landscape evolution and tectonic processes by thermochronology and numerical modeling of crustal heat transport using PECUBE: Tectonophysics, v. 524-525, p. 1-28.

Brown, I., and Mitchell, S. F., 2010, Lithostratigraphy of the Cretaceous succession in the Benbow Inlier, Jamaica: Caribbean Journal of Earth Science, v. 41, p. 25-37.
Brown, R. W., Beucher, R., Roper, S., Persano, C., Stuart, F., and Fitzgerald, P., 2013, Natural age dispersion arising from the analysis of broken crystals. Part I: Theoretical basis and implications for the apatite (U–Th)/He thermochronometer: Geochimica et Cosmochimica Acta, v. 122, p. 478-497.
Burbank, D., Leland, J., Fielding, E., Anderson, R. S., Brozovic, N., Reid, M. R., and Duncan, C., 1996, Bedrock incision, rock uplift and threshold hillslopes in northwestern Himalayas: Nature, v. 379, p. 505-510.
Bürgmann, R., Arrowsmith, R., Dumitru, T., and McLaughlin, R., 1994, Rise and fall of the southern Santa Cruz Mountains, California, from fission tracks, geomorphology, and geodesy: Journal of Geophysical Research: Solid Earth, v. 99, no. B10, p. 20181-20202.
Burke, K., Grippi, J., and Şengör, A. M. C., 1980, Neogene Structures in Jamaica and the Tectonic Style of the Northern Caribbean Plate Boundary Zone: The Journal of Geology, v. 88, no. 4, p. 375-386.
Burkett, C. A., Bemis, S. P., and Benowitz, J. A., 2016, Along-fault migration of the Mount McKinley restraining bend of the Denali fault defined by late Quaternary fault patterns and seismicity, Denali National Park & Preserve, Alaska: Tectonophysics, v. 693, p. 489-506.
Buscher, J. T., and Spotila, J. A., 2007, Near-field response to transpression along the southern San Andreas fault, based on exhumation of the northern San Gabriel Mountains, southern California: Tectonics, v. 26, no. 5, p. n/a-n/a.
Cebula, G. T., Kunk, M. J., Mehnert, H. H., Naeser, C. W., Obradovich, J. D., and Sutter, J. F., 1986, The Fish Canyon Tuff, a potential standard for the 40Ar-39Ar and fission-track dating methods Terra Cognita, v. 6, no. 2, p. 139-140.
Chubb, L. J., and Burke, K., 1963, Age of the Jamaican Granodiorite: Geological Magazine, v. 100, no. 06, p. 524.
Comer, J. B., Naeser, C. W., and McDowell, F. W., 1980, Fission-track ages of zircon from Jamaican bauxite and Terra Rossa: Economic Geology, v. 75, p. 117-121.
Corbeau, J., Rolandone, F., Leroy, S., Mercier de Lépinay, B., Meyer, B., Ellouz-Zimmermann, N., and Momplaisir, R., 2016a, The northern Caribbean plate boundary in the Jamaica Passage: Structure and seismic stratigraphy: Tectonophysics, v. 675, p. 209-226.
Corbeau, J., Rolandone, F., Leroy, S., Meyer, B., Mercier de Lépinay, B., Ellouz-Zimmermann, N., and Momplaisir, R., 2016b, How transpressive is the northern Caribbean plate boundary?: Tectonics, v. 35, no. 4, p. 1032-1046.
Cowgill, E., Yin, A., Arrowsmith, J. R., Feng, W. X., and Shuanhong, Z., 2004, The Akato Tagh bend along the Altyn Tagh fault, northwest Tibet 1: Smoothing by vertical-axis rotation and the effect of topographic stresses on bend-flanking faults: Geological Society of America Bulletin, v. 116, no. 11-12, p. 1423-1442.
Cruz, L., Fayon, A., Teyssier, C., and Weber, J., 2007, Exhumation and deformation processes in transpressional orogens: The Venezuelan Paria Península, SE Caribbean–South American plate boundary, v. 434, p. 149-165.
Cunningham, D., 2007, Structural and topographic characteristics of restraining bend mountain ranges of the Altai, Gobi Altai and easternmost Tien Shan: Geological Society, London, Special Publications, v. 290, no. 1, p. 219-237.

Cunningham, W. D., and Mann, P., 2007, Tectonics of strike-slip restraining and releasing bends: Geological Society, London, Special Publications, v. 290, no. 1, p. 1-12.
Dadson, S. J., Hovius, N., Chen, H., Dade, W. B., Hsieh, M.-L., Willett, S. D., Hu, J.-C., Horng, M.-J., Chen, M.-C., Stark, C. P., Lague, D., and Lin, J.-C., 2003, Links between erosion, runoff variability and seismicity in the Taiwan orogen: Nature, v. 426, p. 648-651.
Dalrymple, G. B., Alexander, E. C. J., Lanphere, M. A., and Kracker, G. P., 1981, Irradiation of samples for $^{40}Ar/^{39}Ar$ dating using the Geological Survey TRIGA reactor: U.S. Geological Survey Professional Paper, v. 1176, p. 1-55.
Deino, A. L., 2014, Users manual for Mass Spec v. 7.961: Berkeley Geochronology Center Special Publication 3, p. 130.
DeMets, C., and Wiggins-Grandison, M., 2007, Deformation of Jamaica and motion of the Gonâve microplate from GPS and seismic data: Geophysical Journal International, v. 168, no. 1, p. 362-378.
Dewey, J. F., Holdsworth, R. E., and Strachan, R. A., 1998, Transpression and transtension zones: Geological Society, London, Special Publications, v. 135, no. 1, p. 1-14.
Dodson, M. H., 1973, Closure temperature in colling geochronological and petrological systems: Contributions to Mineralogy and Petrology, v. 40, p. 259-274.
Domínguez-González, L., Andreani, L., Stanek, K. P., and Gloaguen, R., 2015a, Geomorpho-tectonic evolution of the Jamaican restraining bend: Geomorphology, v. 228, p. 320-334.
Domínguez-González, L., Andreani, L., Stanek, K. P., and Gloaguen, R., 2015b, Reply to the comment of Mitchell et al. on "Geomorpho-tectonic evolution of the Jamaican restraining bend" by L. Domínguez-González, L. Andreani, K.P. Stanek and R. Gloaguen [Geomorphology, 228 (2015) 320–334]: Geomorphology.
Draper, G., 1987, A revised tectonic model for the evolution of Jamaica, *in* Ahmad, R., ed., Proceedings of a Workshop on the Status of Jamaican Geology Special Issue No. 10: Kingston, Jamaica, Geological Society of Jamaica, p. 24-51.
Draper, G., 2008, Some speculations on the Paleogene and Neogene tectonics of Jamaica: Geological Journal, v. 43, no. 5, p. 563-572.
Draper, G., and Arros, J. A. B., 1994, Cuba, *in* Donovan, S. K., and Jackson, T. A., eds., The Caribbean: An Introduction: Kingston, Jamaica, University of the West Indies Publishers' Association, p. 65-83.
Draper, G., Jackson, T. A., and Donovan, S. K., 1994, Geologic provinces of the Caribbean region, *in* Donovan, S. K., and Jackson, T. A., eds., The Caribbean: An Introduction: Kingston, Jamaica, University of the West Indies Publishers' Association, p. 3-12.
Ehlers, T. A., and Farley, K. A., 2003, Apatite (U-Th)/He thermochronometry: methods and applications to problems in tectonic and surface processes: Earth and Planetary Science Letters, v. 206, p. 1-14.
Farley, K. A., 2000, Helium diffusion from apatite: General behavior as illustrated by Durango fluorapatite: Journal of Geophysical Research: Solid Earth, v. 105, no. B2, p. 2903-2914.
Fisher, J., and Mitchell, S. F., 2012, Lithostratigraphy of the Grange Inlier, Westmoreland, Jamaica: Caribbean Journal of Earth Science, v. 44, p. 19-24.
Fitzgerald, P. G., Stump, E., and Redfield, T. F., 1993, Late Cenozoic uplift of Denali and its relation to relative plate motion and fault morphology: Science, v. 259, p. 497-499.
Fleck, R. J., Sutter, J. F., and Elliot, D. H., 1977, Interpretation of discordant $^{40}Ar/^{30}Ar$ age-spectra of Mesozoic tholeiites from Antarctica: Geochimica et Cosmochimica Acta, v. 41, p. 15-32.

Flowers, R. M., Ketcham, R. A., Shuster, D. L., and Farley, K. A., 2009, Apatite (U–Th)/He thermochronometry using a radiation damage accumulation and annealing model: Geochimica et Cosmochimica Acta, v. 73, no. 8, p. 2347-2365.

Fossen, H., and Tikoff, B., 1998, Extended models of transpression and transtension, and application to tectonic settings: Geological Society, London, Special Publications, v. 135, no. 1, p. 15-33.

Fossen, H., Tikoff, B., and Teyssier, C., 1994, Strain modeling of transpressional and transtensional deformation: Norsk Geologisk Tidsskrift, v. 74, p. 134-145.

Gehrels, G., Rusmore, M., Woodsworth, G., Crawford, M., Andronicos, C., Hollister, L., Patchett, J., Ducea, M., Butler, R., Klepeis, K., Davidson, C., Friedman, R., Haggart, J., Mahoney, B., Crawford, W., Pearson, D., and Girardi, J., 2009, U-Th-Pb geochronology of the Coast Mountains batholith in north-coastal British Columbia: Constraints on age and tectonic evolution: Geological Society of America Bulletin, v. 121, no. 9-10, p. 1341-1361.

Gehrels, G. E., Valencia, V. A., and Ruiz, J., 2008, Enhanced precision, accuracy, efficiency, and spatial resolution of U-Pb ages by laser ablation-multicollector-inductively coupled plasma-mass spectrometry: Geochemistry, Geophysics, Geosystems, v. 9, no. 3, p. n/a-n/a.

Gomez, F., Nemer, T., Tabet, C., Khawlie, M., Meghraoui, M., and Barazangi, M., 2007, Strain partitioning of active transpression within the Lebanese restraining bend of the Dead Sea Fault (Lebanon and SW Syria): Geological Society, London, Special Publications, v. 290, no. 1, p. 285-303.

Harland, W. B., 1971, Tectonic transpression in Caledonian Spitsbergen: Geol. Mag., v. 108, no. 1, p. 27-42.

Hastie, A. R., Kerr, A. C., McDonald, I., Mitchell, S. F., Pearce, J. A., Millar, I. L., Barfod, D., and Mark, D. F., 2010, Geochronology, geochemistry and petrogenesis of rhyodacite lavas in eastern Jamaica: A new adakite subgroup analogous to early Archaean continental crust?: Chemical Geology, v. 276, no. 3-4, p. 344-359.

Hastie, A. R., Kerr, A. C., Mitchell, S. F., and Millar, I. L., 2009, Geochemistry and tectonomagmatic significance of Lower Cretaceous island arc lavas from the Devils Racecourse Formation, eastern Jamaica: Geological Society, London, Special Publications, v. 328, no. 1, p. 339-360.

James-Williamson, S. A., and Mitchell, S. F., 2012, Revised lithostratigraphy of the Coastal Group of south-eastern St. Thomas, Jamaica: Caribbean Journal of Earth Science, v. 44, p. 9-17.

James-Williamson, S. A., Mitchell, S. F., and Ramsook, R., 2014, Tectono-stratigraphic development of the Coastal Group of south-eastern Jamaica: Journal of South American Earth Sciences, v. 50, p. 40-47.

Johnston, S. T., 2001, The Great Alaskan Terrane Wreck: reconciliation of paleomagnetic and geologic data in northern Cordillera: Earth and Planetary Science Letters, v. 193, p. 259-272.

Keeler, K. H., 1979, Distribution of Plants with Extrafloral Nectaries and Ants at Two Elevations in Jamaica: Biotropica, v. 11, no. 2, p. 152-154.

Kerr, A. C., Tarney, J., Marriner, G. F., Nivia, A., and Saunders, A. D., 1997, The Caribbean-Colombian Cretaceous igneous Province: the internal anatomy of an Oceanic Plateau, *in*

Mahoney, J. J., and Coffin, M. F., eds., Large Igneous Provinces: Continental, Oceanic, and Planetary Flood Volcanism: Washington, American Geophysical Union, p. 123-144.
Ketcham, R. A., 2005a, Forward and Inverse Modeling of Low-Temperature Thermochronometry Data: Reviews in Mineralogy and Geochemistry, v. 58, no. 1, p. 275-314.
Ketcham, R. A., 2005b, HeFTy Beta Version 2, Austin, Texas, University of Texas, Austin, Dept. of Geo. Sci.
Ketcham, R. A., Gautheron, C., and Tassan-Got, L., 2011, Accounting for long alpha-particle stopping distances in (U–Th–Sm)/He geochronology: Refinement of the baseline case: Geochimica et Cosmochimica Acta, v. 75, no. 24, p. 7779-7791.
Koehler, R. D., Mann, P., Prentice, C. S., Brown, L., Benford, B., and Wiggins-Grandison, M., 2013, Enriquillo-Plantain Garden Fault Zone in Jamaica: Paleoseismology and Seismic Hazard: Bulletin of the Seismological Society of America, v. 103, no. 2A, p. 971-983.
Koons, P. O., 1995, Modeling the topographic evolution of collisional belts: Annual Review of Earth and Planetary Sciences, v. 23, p. 275-408.
Krijnen, J. P., and Chin, A. C. L., 1978, Geology of the northern, central, and south-eastern Blue Mountains, Jamaica, with a provisional compilation map of the entire inlier: Geologie en Mijnbouw, v. 57, no. 2, p. 243-250.
Leroy, S., Ellouz-Zimmermann, N., Corbeau, J., Rolandone, F., de Lépinay, B. M., Meyer, B., Momplaisir, R., Granja Bruña, J.-L., Battani, A., Baurion, C., Burov, E., Clouard, V., Deschamps, R., Gorini, C., Hamon, Y., Lafosse, M., Leonel, J., Le Pourhiet, L., Llanes Estrada, P., Loget, N., Lucazeau, F., Pillot, D., Poort, J., Tankoo, K. R., Cuevas, J.-L., Alcaide, J.-F., Jean Poix, C., Muñoz-Martin, A., Mitton, S., Rodriguez, Y., Schmitz, J., Seeber, L., Carbo-Gorosabel, A., and Muñoz, S., 2015, Segmentation and kinematics of the North America-Caribbean plate boundary offshore Hispaniola: Terra Nova, v. 27, no. 6, p. 467-478.
Leroy, S., Mercier de Lépinay, B., Mauffret, A., and Pubellier, M., 1996, Structural and tectonic evolution of the eastern Cayman Trough (Caribbean Sea) from seismic reflection data: AAPG Bulletin, v. 80, no. 2, p. 222-247.
Little, T. A., Cox, S., Vry, J. K., and Batt, G., 2005, Variations in exhumation level and uplift rate along the obliqu-slip Alpine fault, central Southern Alps, New Zealand: Geological Society of America Bulletin, v. 117, no. 5, p. 707.
Malavieille, J., 2010, Impact of erosion, sedimentation, and structural heritage on the structure and kinematics of orogenic wedges: Analog models and case studies: GSA Today, p. 4-10.
Mann, P., 2007, Global catalogue, classification and tectonic origins of restraining- and releasing bends on active and ancient strike-slip fault systems: Geological Society, London, Special Publications, v. 290, no. 1, p. 13-142.
Mann, P., and Burke, K., 1984, Neotectonics of the Caribbean: Review of Geophysics and Space Physics, v. 22, no. 4, p. 309-362.
Mann, P., and Burke, K., 1990, Transverse intra-arc rifting: Palaeogene Wagwater Belt, Jamaica: Marine and Petroleum Geology, v. 7, p. 410-427.
Mann, P., Calais, E., Ruegg, J.-C., DeMets, C., Jansma, P. E., and Mattioli, G. S., 2002, Oblique collision in the northeastern Caribbean from GPS measurements and geological observations: Tectonics, v. 21, no. 6, p. 7-1-7-26.

Mann, P., Draper, G., and Burke, K., 1985, Neotectonics of a strike-slip restraining bend system Jamaica: Society for Sedimentary Geology, v. Special Publications 37, p. 211-226.
Mann, P., Taylor, F. W., Edwards, R. L., and Ku, T.-L., 1995, Actively evolving microplate formation by oblique collision and sideways motion along strike-slip faults: An example from the northeastern Caribbean plate margin: Tectonophysics, v. 246, p. 1-69.
McAleer, R. J., Bish, D. L., Kunk, M. J., Sicard, K. R., Valley, P. M., Walsh, G. J., Wathen, B. A., and Wintsch, R. P., 2017, Reaction softening by dissolution-precipitation creep in a retrograde greenschist facies ductile shear zone, New Hampshire, USA: Journal of Metamorphic Geology, v. 35, no. 1, p. 95-119.
McDougall, K. A., and Harrison, T. M., 1999, Geochronology and thermochronology by the 40Ar/39Ar method, United States, Oxford University Press.
Miller, S. R., Baldwin, S. L., and Fitzgerald, P. G., 2012, Transient fluvial incision and active surface uplift in the Woodlark Rift of eastern Papua New Guinea: Lithosphere, v. 4, no. 2, p. 131-149.
Mitchell, S. F., 2003, Sedimentology and tectonic evolution of the Cretaceous rocks of Central Jamaica: relationships to the plate tectonic evolution of the Caribbean, *in* Bartolini, C., Buffler, R. T., and Blickwede, J., eds., The Circum-Gulf of Mexico and the Caribbean: Hydrocarbon habitats, basin formation, and plate tectonics:, Volume 79, AAPG Memoir, p. 605-623.
Mitchell, S. F., 2004, Lithostratigraphy and palaeogeography of the White Limestone Group: Cainozoic Research, v. 3, no. 1-2, p. 5-29.
Mitchell, S. F., 2013a, Lithostratigraphy of the Central Inlier, Jamaica: Caribbean Journal of Earth Science, v. 46, p. 31-42.
Mitchell, S. F., 2013b, Stratigraphy of the White Limestoneof Jamaica: Bulletin de la Société Géologique de France, v. 184, no. 1-2, p. 111-118.
Mitchell, S. F., 2016, Geology of the western margin of the Benbow Inlier - implications for the relationship between the Yellow Limestone and White Limestone groups (with the description of the Litchfield Formation, new name): Caribbean Journal of Earth Science, v. 48, p. 19-25.
Mitchell, S. F., and Blissett, D., 2001, Lithostratigraphy of the Late Cretaceous to ?Paleocene succession in the western part of the Central Inlier of Jamaica: Caribbean Journal of Earth Science, v. 35, p. 19-31.
Mitchell, S. F., James-Williamson, S. A., Miller, D. J., and Mandal, A., 2015, Comment on: “Geomorpho-tectonic evolution of the Jamaican restraining bend” by Leomaris Domínguez-González, Louis Andreani, Klaus P. Stanek and Richard Gloaguen [Geomorphology, 228 (2015) 320–334]: Geomorphology.
Mitchell, S. F., Ramsook, R., Coutou, R., and Fisher, J., 2011, Lithostratigraphy and age of the St. Ann’s Great River Inlier, northern Jamaica: Caribbean Journal of Earth Science, v. 42, p. 1-16.
Molnar, P., 1988, Continental tectonics in the aftermath of plate tectonics: Nature, v. 335, no. 6186, p. 131.
Mutti, M., Droxler, A. W., and Cunningham, A. D., 2005, Evolution of the Northern Nicaragua Rise during the Oligocene–Miocene: Drowning by environmental factors: Sedimentary Geology, v. 175, no. 1-4, p. 237-258.
Neill, I., Kerr, A. C., Hastie, A. R., Stanek, K. P., and Millar, I. L., 2011, Origin of the Aves Ridge and Dutch-Venezuelan Antilles: interaction of the Cretaceous 'Great Arc' and

Caribbean-Colombian Oceanic Plateau?: Journal of the Geological Society, v. 168, no. 2, p. 333-348.
Niemi, N. A., Buscher, J. T., Spotila, J. A., House, M. A., and Kelley, S. A., 2013, Insights from low-temperature thermochronometry into transpressional deformation and crustal exhumation along the San Andreas fault in the western Transverse Ranges, California: Tectonics, v. 32, no. 6, p. 1602-1622.
Northmore, K. J., Ahmad, R., O'Connor, E. A., Greenbaum, D., McDonald, A. J. W., Jordan, C. J., Marchant, A. P., and Marsh, S. H., 2000, Landslide hazard mapping: Jamaica case study, BGS Technical Report WC/00/10.
Paces, J. B., and Miller, J. D., 1993, Precise U-Pb ages of Duluth Complex and related mafic intrusions, northeastern Minnesota: Geochronological insights to physical, petrogenetic, paleomagnetic, and tectonomagmatic processes associated with the 1.1 Ga Midcontinent Rift System: Journal of Geophysical Research: Solid Earth, v. 98, no. B8, p. 13997-14013.
Pindell, J., 1994, Evolution of the Gulf of Mexico and the Caribbean, *in* Donovan, S. K., and Jackson, T. A., eds., The Caribbean: An Introduction: Kingston, Jamaica, University of the West Indies Publishers' Association, p. 13-39.
Pindell, J., Maresch, W. V., Martens, U., and Stanek, K., 2012, The Greater Antillean Arc: Early Cretaceous origin and proposed relationship to Central American subduction mélanges: implications for models of Caribbean evolution: International Geology Review, v. 54, no. 2, p. 131-143.
Reiners, P. W., 2005, Zircon (U-Th)/He Thermochronometry: Reviews in Mineralogy and Geochemistry, v. 58, no. 1, p. 151-179.
Reiners, P. W., Spell, T. L., Nicolescu, S., and Zanetti, K. A., 2004, Zircon (U-Th)/He thermochronometry: He diffusion and comparisons with 40Ar/39Ar dating: Geochimica et Cosmochimica Acta, v. 68, no. 8, p. 1857-1887.
Reiners, P. W., Zhou, Z., Ehlers, T. A., Xu, C., Brandon, M. T., Donelick, R. A., and Nicolescu, S., 2003, Post-orogenic evolution of the Dabie Shan, eastern China, from (U-Th)/He and fission-track thermochronology: American Journal of Science, v. 303, p. 489-518.
Renne, P. R., Swisher, C. C., Deino, A. L., Karner, D. B., Owens, T. L., and DePaolo, D. J., 1998, Intercalibration of standards, absolute ages and uncertainties in $^{40}Ar/^{39}Ar$ dating: Chemical Geology, v. 145, p. 117-152.
Robinson, E., 1994, Jamaica, *in* Donovan, S. K., and Jackson, T. A., eds., The Caribbean: An Introduction: Kingston, Jamaica, University of the West Indies Publishers' Association, p. 111-127.
Rosencrantz, E., Ross, M. I., and Sclater, J. G., 1988, Age and spreading history of the Cayman Trough as determined from depth, heat flow, and magnetic anomalies: Journal of Geophysical Research, v. 93, no. B3, p. 2141.
Sanchez, J., Mann, P., and Emmet, P. A., 2015, Late Cretaceous-Cenozoic tectonic transition from collision to transtension, Honduran Borderlands and Nicaraguan Rise, NW Caribbean Plate boundary: Geological Society, London, Special Publications.
Sanchez, J., Mann, P., and Emmet, P. A., 2016, Late Cretaceous–Cenozoic tectonic transition from collision to transtension, Honduran Borderlands and Nicaraguan Rise, NW Caribbean Plate boundary: Geological Society, London, Special Publications, v. 431, no. 1, p. 273-297.

Schmitz, M. D., Bowring, S. A., and Ireland, T. R., 2003, Evaluation of Duluth Complex anorthositic series (AS3) zircon as a U-Pb geochronological standard: new high-precision isotope dilution thermal ionization mass spectrometry results: Geochimica et Cosmochimica Acta, v. 67, no. 19, p. 3665-3672.

Scientific Research Council of Jamaica, 1963, The Rainfall of Jamaica.

Şengör, A. M. C., 1987, Tectonics of the Tethysides: orogenic collage development in a collisional setting: Annual Review of Earth and Planetary Sciences, v. 15, p. 213-244.

Şengör, A. M. C., and Natal'in, B., 2004, Ribbon continents: a marginal affair of central importance: Geological Society of America Abstacts with Programs, v. 36, no. 5, p. 534.

Simon-Labric, T., Brocard, G. Y., Teyssier, C., van der Beek, P. A., Fellin, M. G., Reiners, P. W., and Authemayou, C., 2013, Preservation of contrasting geothermal gradients across the Caribbean-North America plate boundary (Motagua Fault, Guatemala): Tectonics, p. n/a-n/a.

Spotila, J. A., 2005, Applications of Low-Temperature Thermochronometry to Quantification of Recent Exhumation in Mountain Belts: Reviews in Mineralogy and Geochemistry, v. 58, no. 1, p. 449-466.

Spotila, J. A., and Berger, A. L., 2010, Exhumation at orogenic indentor corners under long-term glacial conditions: Example of the St. Elias orogen, Southern Alaska: Tectonophysics, v. 490, no. 3-4, p. 241-256.

Spotila, J. A., Farley, K. A., Yule, J. D., and Reiners, P. W., 2001, Near-field transpressive deformation along the San Andreas fault zone in southern California, based on exhumation constrained by (U-Th)/He dating: Journal of Geophysical Research: Solid Earth, v. 106, no. B12, p. 30909-30922.

Spotila, J. A., House, M., Niemi, N., Brady, R., Oskin, M., and Buscher, J., 2007a, Patterns of bedrock uplift along the San Andreas fault and implications for mechanisms of transpression, *in* Till, A. B., Roeske, S. M., Sample, J. C., and Foster, D. A., eds., Exhumation Associated with Continental Strike-Slip Fault Systems, Geological Society of America Special Paper 434, p. 15-33.

Spotila, J. A., Niemi, N., Brady, R., House, M., Buscher, J., and Oskin, M., 2007b, Long-term continental deformation associated with transpressive plate motion: The San Andreas fault: Geology, v. 35, no. 11, p. 967.

Staudacher, T., Jessberger, E. K., Dorflinger, D., and Kiko, J., 1978, A refined ultrahigh-vacuum furnace for rare gas analysis: Journal of Physics E: Scientific Instruments, v. 11, p. 781-784.

Sylvester, A. G., 1988, Strike-slip faults: Geological Society of America Bulletin, v. 100, no. 11, p. 1666-1703.

Tanner, E. V. J., 1980, Litterfall in Montane rain forests of Jamaica and its relation to climate: Journal of Ecology, v. 68, no. 3, p. 833-848.

Teyssier, C., Tikoff, B., and Markley, M., 1995, Oblique plate motion and continental tectonics: Geology, v. 23, no. 5, p. 447.

Tikoff, B., and Teyssier, C., 1994, Strain modeling of displacement-field partitioning in transpressional orogens: Journal of Structural Geology, v. 16, no. 11, p. 1575-1588.

Tikoff, B., Teyssier, C., and Waters, C., 2002, Clutch tectonics and the partial attachment of lithospheric layers: EGU Stephan Mueller Special Publication Series, v. 1, p. 57-73.

Tranel, L. M., Spotila, J. A., Kowalewski, M. J., and Waller, C. M., 2011, Spatial variation of erosion in a small, glaciated basin in the Teton Range, Wyoming, based on detrital apatite (U-Th)/He thermochronology: Basin Research, v. 23, no. 5, p. 571-590.

Valentino, J. D., Spotila, J. A., Owen, L. A., and Buscher, J. T., 2016, Rock uplift at the transition from flat-slab to normal subduction: The Kenai Mountains, Southeast Alaska: Tectonophysics, v. 671, p. 63-75.

Van Dusen, S. R., and Doser, D. I., 2000, Faulting processes of historic (1917–1962) M≥6.0 earthquakes along the north-central Caribbean margin: Pure and Applied Geophysics, v. 157, p. 719-736.

Wadge, G., and Draper, G., 1978, Structural geology of the southeastern Blue Mountains, Jamaica: Geologie en Mijnbouw, v. 57, no. 2, p. 347-352.

Wadge, G., Jackson, T. A., Isaacs, M. C., and Smith, T. E., 1982, The ophiolitic Bath-Dunrobin Formation, Jamaica: significance for Cretaceous plate margin evolution in the north-western Caribbean: Journal of Geological Society, London, v. 139, p. 321-333.

West, D. P., Abbott, R. N., Bandy, B. R., and Kunk, M. J., 2014, Protolith provenance and thermotectonic history of metamorphic rocks in eastern Jamaica: Evolution of a transform plate boundary: Geological Society of America Bulletin, v. 126, no. 3-4, p. 600-614.

Whipple, K. X., 2004, Bedrock Rivers and the Geomorphology of Active Orogens: Annual Review of Earth and Planetary Sciences, v. 32, no. 1, p. 151-185.

Whipple, K. X., and Meade, B. J., 2004, Controls on the strength of coupling among climate, erosion, and deformation in two-sided, frictional orogenic wedges at steady state: Journal of Geophysical Research: Earth Surface, v. 109, no. F1, p. n/a-n/a.

Wiggins-Grandison, M., 2001, Preliminary results from the New Jamaica Seismograph Network: Seismological Research Letters, v. 72, no. 5, p. 525-537.

Wiggins-Grandison, M. D., and Atakan, K., 2005, Seismotectonics of Jamaica: Geophysical Journal International, v. 160, no. 2, p. 573-580.

Willett, S. D., 1999, Orogeny and orography: The effects of erosion on the structure of mountain belts: Journal of Geophysical Research: Solid Earth, v. 104, no. B12, p. 28957-28981.

Willett, S. D., Fisher, D., Fuller, C., En-Chao, Y., and Chia-Yu, L., 2003, Erosion rates and orogenic-wedge kinematics in Taiwan inferred from fission-track thermochronometry: Geology, v. 31, no. 11, p. 945–948.

Wolf, R. A., Farley, K. A., and Silver, L. T., 1996, Helium diffusion and low-temperature thermochronometry of apatite: Geochimica et Cosmochimica Acta, v. 60, no. 21, p. 4231-4240.

2.9.0 Tables.

Table 1. Apatite (U-Th)/He data

Sample	Elevation (m)	Longitude	Latitude	Rock Type	mass (mg)	MWAR (um)	He (pmol)	U (ppm)	Th (ppm)	Sm (ppm)	# of grains	F_T	Corr. Age (Ma)	Average Age (Ma)	Standard Deviation
JAM1*	324	-76.5822	18.1458	Serpentinite	0.0229	77.1	0.1671	7.0	0.3	50.6	3	0.835	231.14		
					0.0131	53.9	0.1833	12.9	0.7	62.1	4	0.783	255.43	250.8	17.74 Ma
					0.0105	49.3	0.2109	18.0	3.7	130.2	4	0.749	265.69		7.1%
JAM4**	2124	-76.4823	17.9729	Volcanic	0.0053	60.6	0.0004	3.5	9.6	102.9	2	0.784	2.83		
				(andesitic)	0.0047	40.8	0.0004	2.8	11.7	141.6	4	0.702	4.12	3.47	0.91 Ma
					0.0047	40.7	0.0323	32.7	39.6	163.8	4	0.685	44.67		26.2%
JAM6***	1724	-76.5789	18.0471	Volcanic	0.0122	67.5	0.0184	14.2	11.3	128.2	1	0.831	20.32		
				(rhyolitic)	0.0115	52.7	0.0140	7.2	17.3	122.6	5	0.766	26.41		
					0.0131	54.6	0.0147	3.3	*7.0*	115.2	5	0.775	53.50	24.8	5.73 Ma
					0.0072	45.7	0.0026	2.6	8.1	107.2	5	0.727	20.17		23.1%
					0.0072	46.9	0.0041	2.6	7.7	113.0	4	0.737	32.17		
					0.0057	39.9	0.0064	3.2	11.4	130.7	5	0.689	50.41		
					0.0053	40.6	0.0100	3.5	11.1	150.0	6	0.702	80.27		
JAM7	996	-76.5839	18.0459	Schist	0.0092	69.0	0.0076	27.9	65.9	65.9	2	0.806	4.48		
					0.0065	55.4	0.0120	21.6	55.8	64.7	3	0.768	12.94		
					0.0064	50.4	0.0062	33.9	85.2	72.2	4	0.729	4.66	4.70	0.40 Ma
					0.0067	53.0	0.0082	37.0	95.3	74.7	4	0.740	5.27		8.5%
					0.0050	40.0	0.0035	29.0	67.1	75.2	5	0.681	4.38		
JAM8	965	-76.5872	18.0444	Serpentinite	0.0080	103.5	0.0013	1.4	0.9	32.4	1	0.869	21.92		
					0.0112	67.5	0.0003	1.4	1.4	47.9	2	0.819	3.11		
					0.0100	55.6	0.0002	1.7	3.3	65.7	3	0.774	2.21	3.42	1.39 Ma
					0.0062	72.0	0.0005	1.1	2.2	57.1	2	0.830	10.52		40.7%
					0.0085	60.1	0.0004	1.5	1.9	65.7	3	0.789	4.94		
JAM9	1170	-76.5971	18.0506	Granitoid	0.0174	66.3	0.0013	4.4	10.4	148.3	5	0.824	2.39		
					0.0177	66.3	0.0015	4.1	10.2	153.2	5	0.800	3.05		
					0.0184	59.9	0.0023	5.2	14.8	169.8	5	0.793	3.35	3.39	0.72 Ma
					0.0140	56.6	0.0015	3.8	9.7	145.1	5	0.777	4.16		21.2%
					0.0134	53.5	0.0017	5.1	11.6	157.4	5	0.770	3.99		
JAM10***	1262	-76.6101	18.0368	Granitoid	0.0026	31.9	0.0141	4.9	15.9	293.5	5	0.644	178.03		
					0.0031	33.2	0.0008	4.1	10.5	134.7	6	0.656	11.42		

					0.0029	31.8	0.0012	3.6	9.2	125.0	5	0.647	19.95		
					0.0040	30.4	0.0010	7.1	18.3	128.2	7	0.641	6.44	10.0	3.12 Ma
					0.0049	33.0	0.0015	4.3	10.5	132.3	6	0.670	12.19		31.1%
					0.0034	32.4	0.0035	5.0	13.3	202.2	6	0.666	34.28		
					0.0030	30.5	0.0005	4.1	11.9	142.3	7	0.639	66.59		
JAM11	709	-76.6106	18.0344	Granodiorite	0.0130	96.6	0.0008	10.9	16.2	143.6	1	0.890	0.92		
					0.0138	76.5	0.0016	19.9	20.3	127.9	3	0.835	1.07		
					0.0090	69.6	0.0020	28.6	29.5	151.6	2	0.817	1.42		
					0.0081	48.2	0.0028	34.1	30.1	127.7	5	0.727	2.17	1.23	0.31 Ma
					0.0224	66.3	0.0028	21.2	23.6	127.0	5	0.816	1.07		25.2%
					0.0151	59.6	0.0016	11.4	14.5	151.5	5	0.800	1.68		
JAM12	515	-76.6321	18.0457	Conglomerate	0.0276	87.9	0.0029	4.8	15.4	115.6	2	0.871	2.69		
					0.0412	108.6	0.0229	6.5	20.9	299.3	2	0.876	10.22		
					0.0210	94.5	0.0066	6.7	24.7	352.4	2	0.863	5.32	2.93	1.07 Ma
					0.0306	66.8	0.0066	5.7	24.3	284.2	4	0.811	4.27		36.5%
					0.0274	60.9	0.0052	7.8	23.6	334.2	6	0.786	3.35		
					0.0137	69.7	0.0026	5.9	24.7	193.3	2	0.823	3.67		
					0.0112	72.8	0.0008	6.9	23.1	455.4	2	0.828	1.26		
					0.0117	67.5	0.0015	6.1	27.5	252.1	2	0.812	2.34		
JAM13	965	-76.6174	18.0482	Volcanic	0.0238	103.5	0.0222	5.5	4.0	75.7	1	0.882	30.83		
				(dacitic)	0.0184	126.0	0.0104	1.2	2.7	114.2	1	0.891	59.91		
					0.0137	99.0	0.0095	4.0	6.3	59.4	1	0.874	27.20	30.4	2.28 Ma
					0.0163	79.2	0.1513	42.7	101.5	145.4	2	0.844	31.09		7.5%
					0.0211	75.4	0.0127	2.7	5.3	93.0	3	0.851	32.56		
JAM15	123	-76.6394	18.0238	Sandstone	0.0323	96.8	0.0080	1.7	9.8	177.6	2	0.870	12.69	9.97	3.84 Ma
					0.0324	96.5	0.0065	3.2	11.1	151.1	2	0.871	7.26		38.5%
JAM16	472	-76.6772	18.0293	Granitoid	0.0187	61.5	0.0014	6.7	9.1	177.0	5	0.799	1.96		
					0.0291	70.5	0.0147	10.9	11.3	206.4	4	0.815	8.59		
					0.0201	82.5	0.0015	7.2	8.3	171.9	3	0.839	1.80	1.99	0.21 Ma
					0.0134	66.5	0.0011	6.8	7.5	163.4	3	0.803	2.22		10.5%
					0.0129	49.7	0.0025	8.4	8.7	184.5	6	0.741	4.66		
JAM17	47	-76.5050	18.1276	Conglomerate	0.0197	87.6	0.0023	4.4	4.9	123.1	2	0.857	4.66		
					0.0189	84.8	0.0065	4.1	8.4	98.6	2	0.852	12.51		
					0.0166	83.9	0.0038	5.1	9.4	91.6	2	0.843	6.89	5.77	1.58 Ma
					0.0171	85.6	0.0061	4.2	6.2	102.1	2	0.862	13.78		27.4%
JAM18	1545	-76.4290	18.0771	Gabbro	0.0151	87.4	0.0063	4.0	9.7	140.5	1	0.866	14.06		

					0.0310	73.9	0.0058	4.3	11.2	147.8	5	0.850	5.82		
					0.0304	79.7	0.0041	3.9	9.6	130.3	5	0.858	4.69		
					0.0196	76.0	0.0043	3.9	10.7	132.7	5	0.841	7.50		
					0.0208	64.8	0.0057	4.2	18.3	136.0	5	0.829	7.18	6.36	1.04 Ma
					0.0148	54.9	0.0033	4.8	12.0	156.5	5	0.792	6.89		16.4%
					0.0292	77.2	0.0059	4.5	11.8	145.4	5	0.846	6.09		
JAM19	2237	-76.6165	18.1474	Sandstone	0.0104	56.4	0.0024	5.0	15.1	150.8	4	0.783	6.36		
					0.0076	44.2	0.0052	4.1	9.2	176.2	5	0.721	2.80		
					0.0072	43.1	0.0015	4.7	12.4	138.3	5	0.714	7.14		
					0.0064	41.8	0.0009	4.1	12.6	183.7	5	0.708	5.32	5.24	1.72 Ma
					0.0078	45.4	0.0011	4.2	10.5	134.7	5	0.736	5.37		32.8%
					0.0046	37.5	0.0009	4.0	14.1	165.3	5	0.687	7.50		
					0.0068	49.7	0.0005	3.4	8.5	189.2	4	0.759	3.64		
					0.0055	43.8	0.0007	5.7	14.9	155.1	4	0.719	3.77		
JAM20	100	-76.8392	18.2887	Granitoid	0.0265	96.5	0.0009	2.2	5.8	146.7	2	0.869	1.94		
					0.0357	86.8	0.0017	1.9	4.9	155.2	3	0.863	3.26	2.27	0.87 Ma
					0.0275	66.9	0.0031	2.4	6.3	156.6	5	0.825	6.40		38.1%
					0.0187	61.8	0.0017	2.5	6.7	136.7	4	0.805	5.11		
					0.0200	62.7	0.0015	8.7	10.9	152.4	5	0.791	1.62		

MWAR = mass-weighted average radius

F_T = alpha ejected correction factor

eU = U + (0.235 x Th), effective uranium concentration

Standard deviation of ages used for average are as Ma and percent

Ages in red are excluded from averages (see 3.3 for explanation)

Latitude, longitude, and vertical datum are WGS84

**Anomalously old age that reproduced, but is inconsistent with age of the rocks and all other data.*

***Low He gas content; should be considered poorly constrained*

****Measured ages did not reproduce into a meaningful average age.*

Table 2. Zircon (U-Th)/He data

Sample	mass zirc (g)	He (pmol)	U (ppm)	Th (ppm)	Th/U	4He/g (nmol)	Raw age (Ma)	*Corr. age (Ma)	1s age (Ma)	Average Age (Ma)	Standard Deviation
JAM6_Z1	2.70E-06	0.0345	141.3	69.0	0.5012	12.78	15.03	21.00	0.41		
JAM6_Z2	2.77E-06	0.0290	151.7	78.9	0.5332	10.49	11.42	15.99	0.25		
JAM6_Z3	1.53E-06	0.0150	102.7	58.1	0.5802	9.83	15.65	23.03	0.48	13.86	3.04 Ma
JAM6_Z4	1.29E-06	0.0080	146.2	80.0	0.5617	6.21	6.98	10.38	0.28		21.9%
JAM6_Z5	1.68E-06	0.0181	173.6	87.4	0.5164	10.79	10.30	15.20	0.24		
JAM6_Z6	2.20E-06	0.0579	150.3	83.7	0.5714	26.37	28.71	39.58	0.87		
JAM9_Z1	3.35E-06	0.0744	314.6	203.8	0.6646	22.20	11.34	14.99	0.21		
JAM9_Z2	5.18E-06	0.1035	271.6	164.3	0.6206	19.98	11.93	15.29	0.21	17.25	2.67 Ma
JAM9_Z3	3.22E-06	0.0560	187.2	89.3	0.4895	17.41	15.49	20.68	0.30		15.5%
JAM9_Z5	1.32E-05	0.2774	220.2	145.7	0.6788	21.02	15.30	18.06	0.37		
JAM11_Z5	8.33E-06	0.0678	121.3	50.0	0.4226	8.13	11.34	13.71	0.29		
JAM11_Z6	9.36E-06	0.0030	84.0	35.6	0.4340	0.32	0.64	0.77	0.02	15.18	1.91 Ma
JAM11_Z7	4.96E-06	0.1291	320.9	154.8	0.4948	26.03	13.50	17.34	0.25		12.6%
JAM11_Z8	4.47E-06	0.0192	64.6	26.8	0.4264	4.30	11.25	14.49	0.22		
JAM16_Z1	3.89E-06	0.1965	194.7	163.4	0.8607	50.50	40.02	53.30	0.75		
JAM16_Z2	4.27E-06	0.2603	414.5	123.2	0.3049	60.89	25.43	32.89	0.49	34.73	2.60 Ma
JAM16_Z3	3.13E-06	0.0725	141.9	60.4	0.4363	23.18	27.48	36.57	0.69		7.5%
JAM19_Z1	1.94E-06	0.0129	93.5	34.6	0.3802	6.67	12.16	16.91	0.34		
JAM19_Z2	2.19E-06	0.0439	160.5	80.5	0.5143	20.07	20.72	28.83	0.55		
JAM19_Z3	1.42E-06	0.0117	96.8	48.2	0.5104	8.26	14.15	20.79	0.44	19.73	2.47 Ma
JAM19_Z4	3.47E-06	0.0690	148.4	86.5	0.5979	19.90	21.83	28.81	0.53		12.5%
JAM19_Z5	1.33E-06	0.0303	254.0	161.9	0.6537	22.73	14.42	21.49	0.40		
JAM20_Z1	2.32E-06	0.0888	191.9	121.8	0.6512	38.32	32.15	44.43	0.80		
JAM20_Z2	2.64E-06	0.1956	381.4	180.5	0.4855	74.13	32.36	43.88	0.79	44.15	0.39 Ma
JAM20_Z3	3.80E-06	0.0202	87.3	33.4	0.3918	5.33	10.38	12.84	0.25		0.9%

Latitude, longitude, elevation, and lithology for each sample can be found in AHe data table

1s error of measurement, 1 standard deviation of the mean

Standard deviation of ages used for average are as Ma and percent

Ages in red are excluded from average (see 3.3 for explanation)

U and Th ppm based on mass of zircon grains

**F_T correction factors for ^{238}U. ^{235}U, ^{232}Th, ^{147}Sm used for corrected age given in supplement*

Full data table can be found in supplement, Section 3

2.10.0 FIGURES

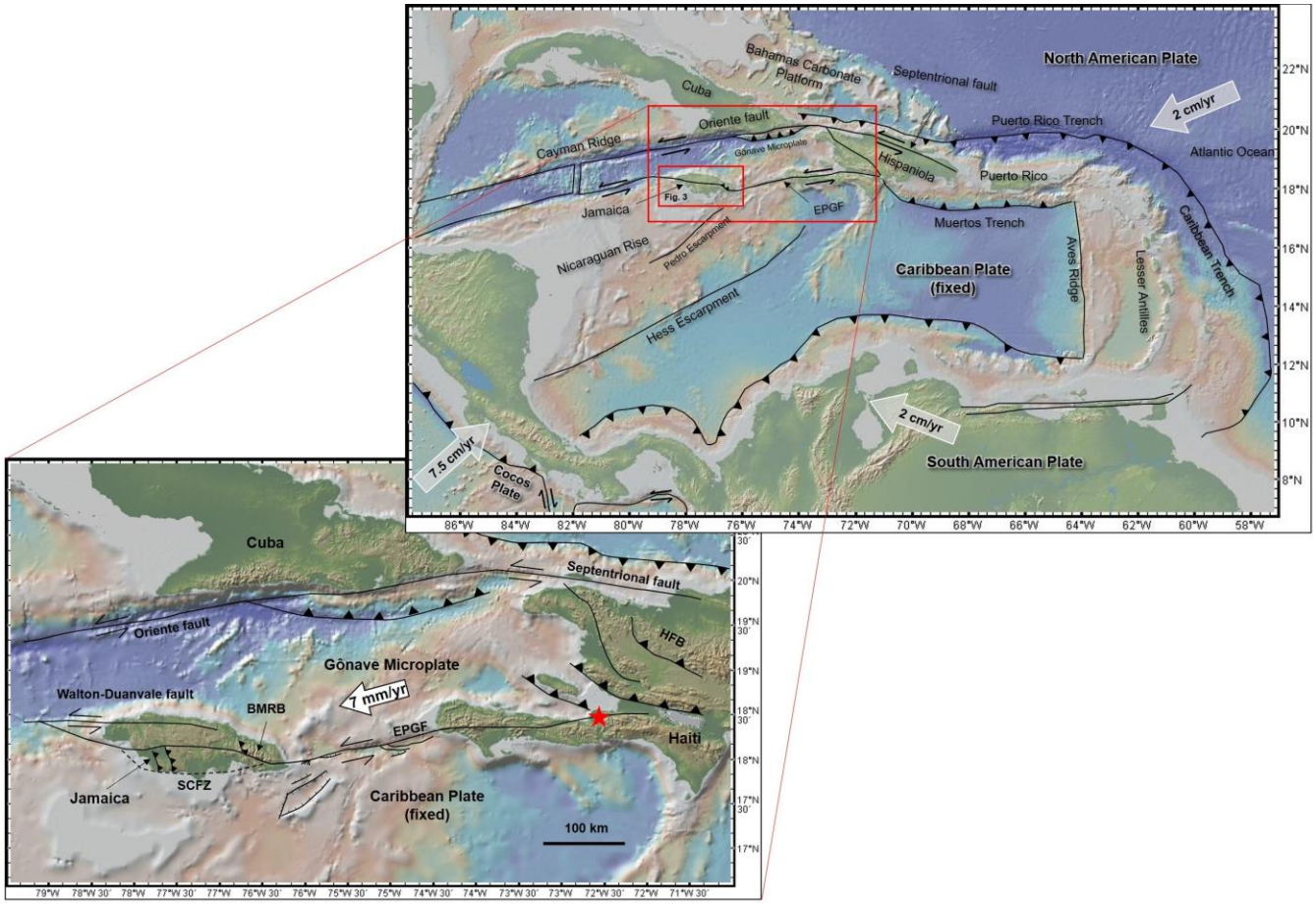

Figure 1. Generalized tectonic map of the Caribbean region showing the major tectonic elements, faults, and plate boundaries. Bathymetry and topography data were built by NOAA Globe (1 km) using GeoMapApp 3.5.Upper figure: GPS velocities from DeMets et al. (2010), and are relative to a fixed Caribbean Plate. Lower figure: GPS velocities for the Gônave microplate are from Benford et al. (2012), relative to a fixed Caribbean Plate. Red star indicates epicenter of the 2010 Haiti earthquake (M_w = 7.0). EPGF – Enriquillo Plantain Garden Fault, HFB – Haiti Fold Belt, SCFZ – South Coast fault zone, BMRB – Blue Mountains restraining bend.

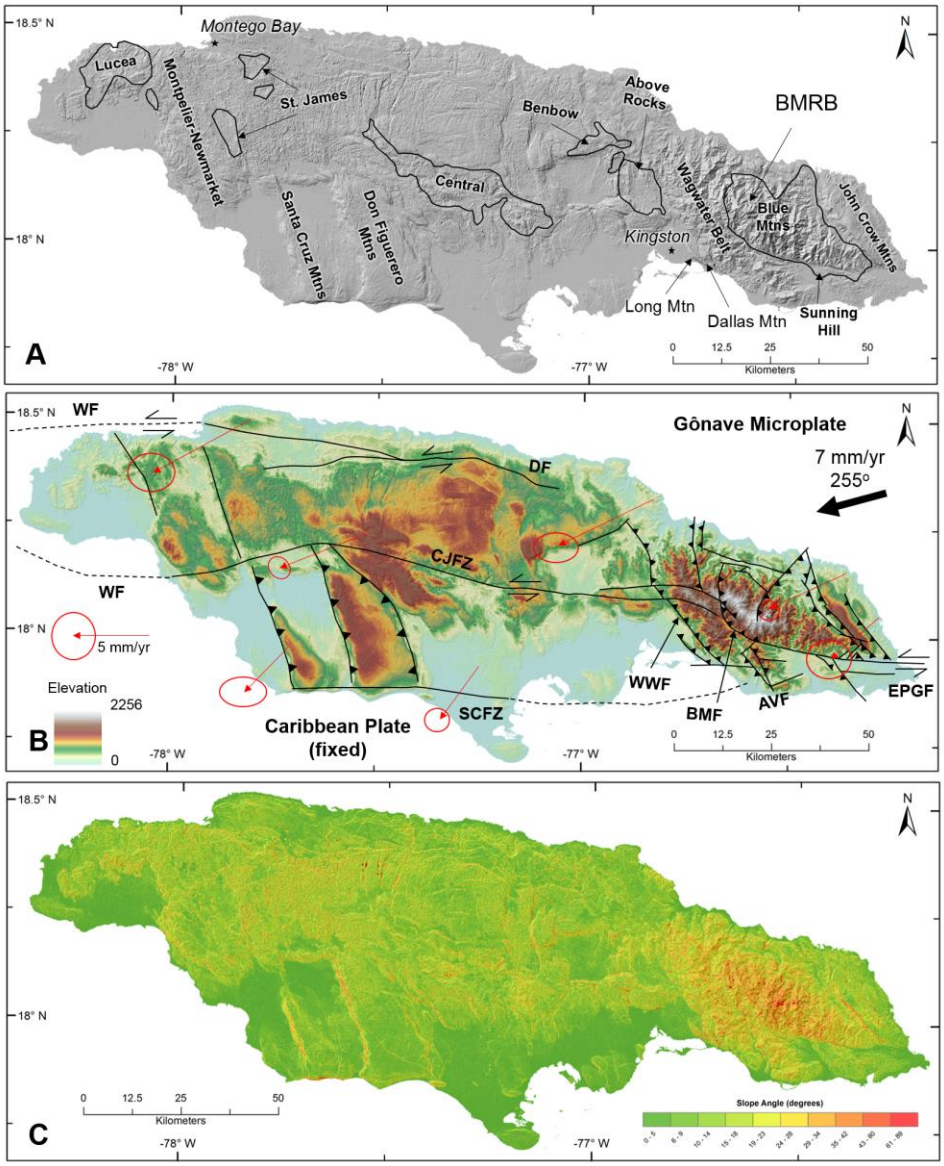

Figure 2. A) Shaded relief map of Jamaica derived from 1/3 arc-second ASTER DEM showing the different Cretaceous Inliers (black outlines) and mountain ranges mentioned in Section 2. B) 1/3 arc-second ASTER DEM indicating the major faults within Jamaica. GPS velocity of Gônave microplate relative to fixed Caribbean Plate (Benford et al., 2012; DeMets and Wiggins-Grandison, 2007). Faults shown are the major through-going faults of Jamaica and are a composite from several sources (Benford et al., 2012; Benford et al., 2014; James-Williamson et al., 2014; Mitchell, 2016; Wiggins-Grandison and Atakan, 2005). GPS vectors from Benford et al. (2012b) relative to fixed Caribbean Plate. Dashed lines proposed continuation of faults offshore. AVF – Aeolus Valley fault, BMF – Blue Mountains fault, CJFZ – Central Jamaican fault zone, DF – Duanvale fault, EPGF – Enriquillo Plantain Garden fault, WF – Walton fault, WWF – Wagwater fault. C) Slope-angle map derived from 1/3 arc second ASTER DEM, showing that the Blue Mountains region has the greatest magnitude of relief and steepest slopes of Jamaica.

Figure 3. Field photos from bedrock sampling during 2014 campaign. Top: Facing east, a photo composite of Blue Mountain Peak showing complete coverage of slopes by thick vegetation. Taken near JAM10 (see Fig. 4). Lower left: Slot canyon on northern flank of Blue Mountains in the Swift River watershed showing a knickzone within near-vertical faces of Cretaceous sedimentary bedrock, located south of JAM20 (Late Cretaceous granodiorite) (see Fig. 4). Lower middle: Typical bedrock sampling location of deeply weathered granite near saprolite conditions, located at JAM9 (see Fig. 4). Lower right: Facing east, highly vegetated, extremely steep slopes vulnerable to mass wasting during storm events. Taken upslope and to the east of JAM1 (see Fig. 4) [photos taken by William Cochran].

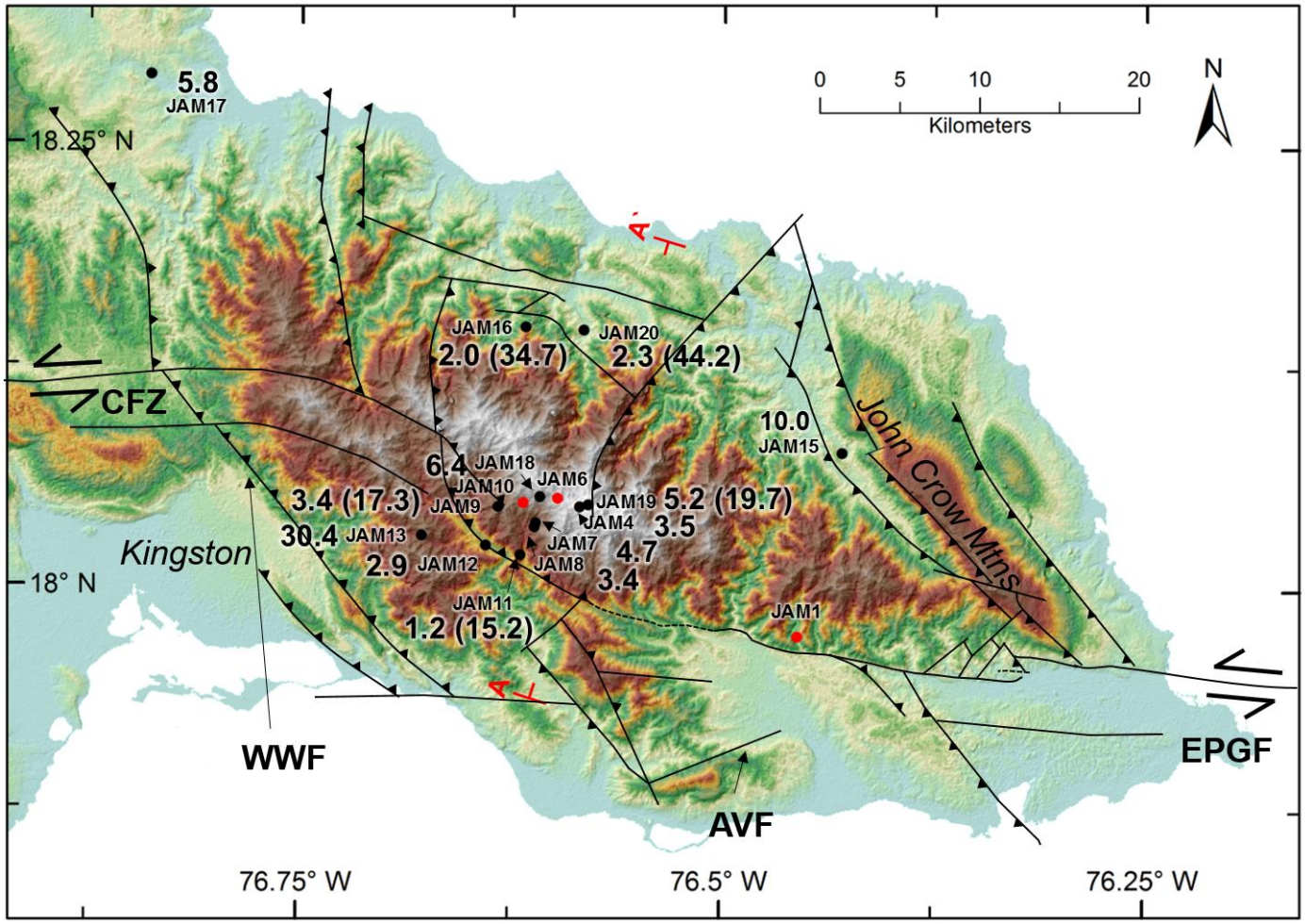

Figure 4. Average AHe and ZHe (in parentheses) ages (Ma) for the Blue Mountains region. Labels adjacent to each dot correspond to sample name in Tables 1 & 2. Topographic profile A-A` for Figure 9 is shown. Red dot: sample that did not produce a meaningful average AHe age; Black dot: sample with a meaningful AHe result (see section 4). Fault locations were taken from James-Williamson et al. (2014) and Mann and Burke (1990). AVF – Aeolus Valley fault, BMF – Blue Mountains fault, CJFZ – Central Jamaican fault zone, EPGF – Enriquillo Plantain Garden fault, SCFZ – South Coast fault zone, WWF – Wagwater fault.

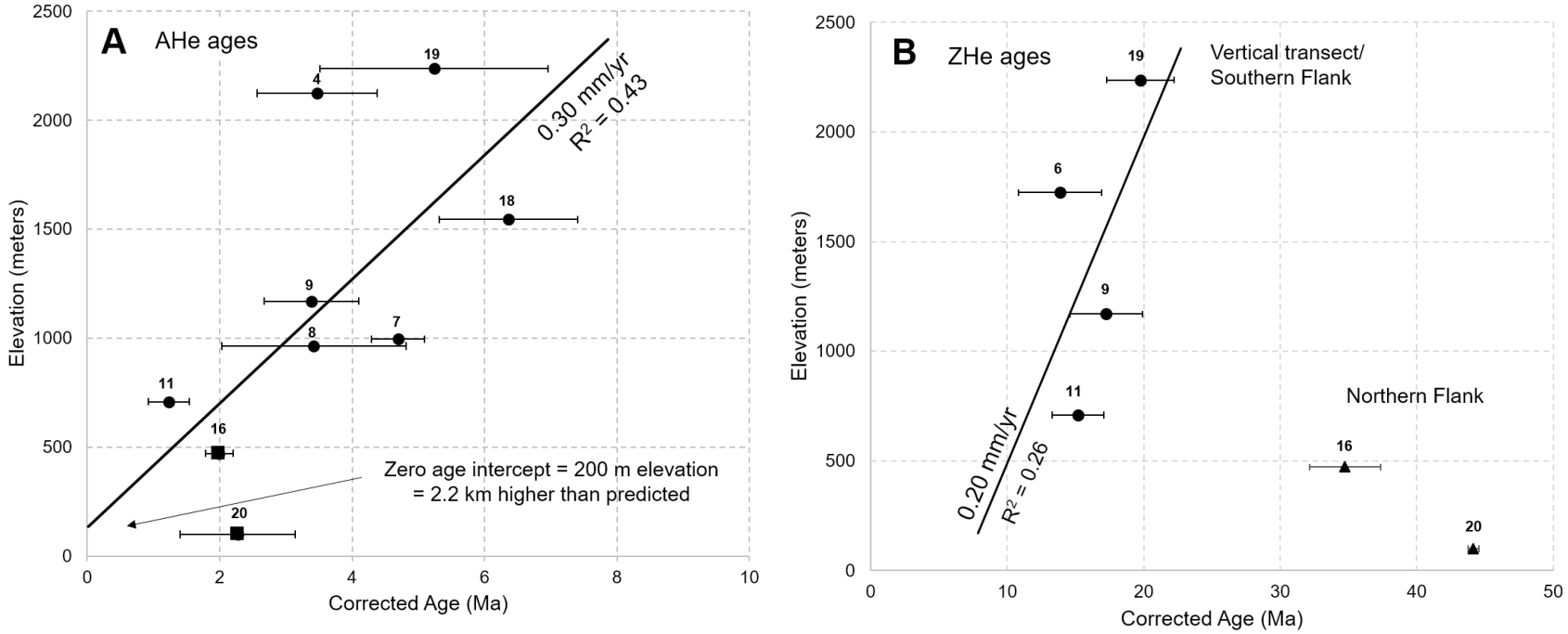

Figure 5. Age-Elevation plots for mean AHe (A) and ZHe (B) ages located within the core of Blue Mountains. Number labels corresponds to sample number found in Tables 1 & 2 and Figure 4. Each line is a linear regression of data along the vertical transect (circles), with the R^2 value corresponding to statistical goodness-of-fit, with the slope of the line representing exhumation rate along the vertical transect. The circles represent data along our vertical transect. Squares and triangles represent data along the northern flank. A) The y-intercept of the best-fit line should correspond to a predicted depth of 2 km, representing the zero-age for helium closure (Spotila, 2005). B) Data are separated by the northern and southern flanks, with the best-fit line of data only along the southern flank (i.e. vertical transect).

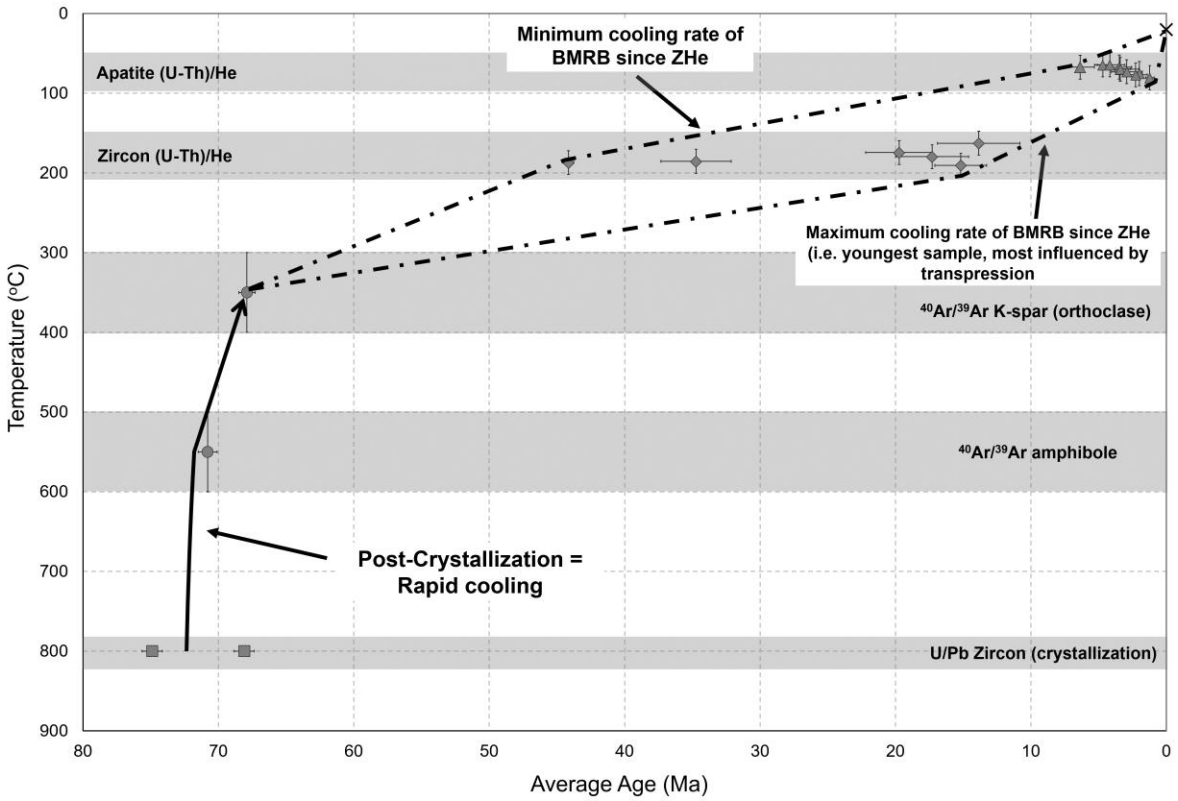

Figure 6. Generalized time-temperature cooling path based on the U/Pb, $^{40}Ar/^{39}Ar$, ZHe, and AHe data. Each gray box corresponds to a typical cooling temperature based on the system used (see section 3.1-3.2). Solid line represents earlier stage of cooling from crystallization to $^{40}Ar/^{39}Ar$ K-feldspar closure temperature. Dashed lines represent two end-member cooling pathways based on the cooling rates after ZHe closure. ZHe closure temperatures determined by adding an additional 110 ^{o}C from our calculate closure temperatures for AHe (Reiners, 2005).

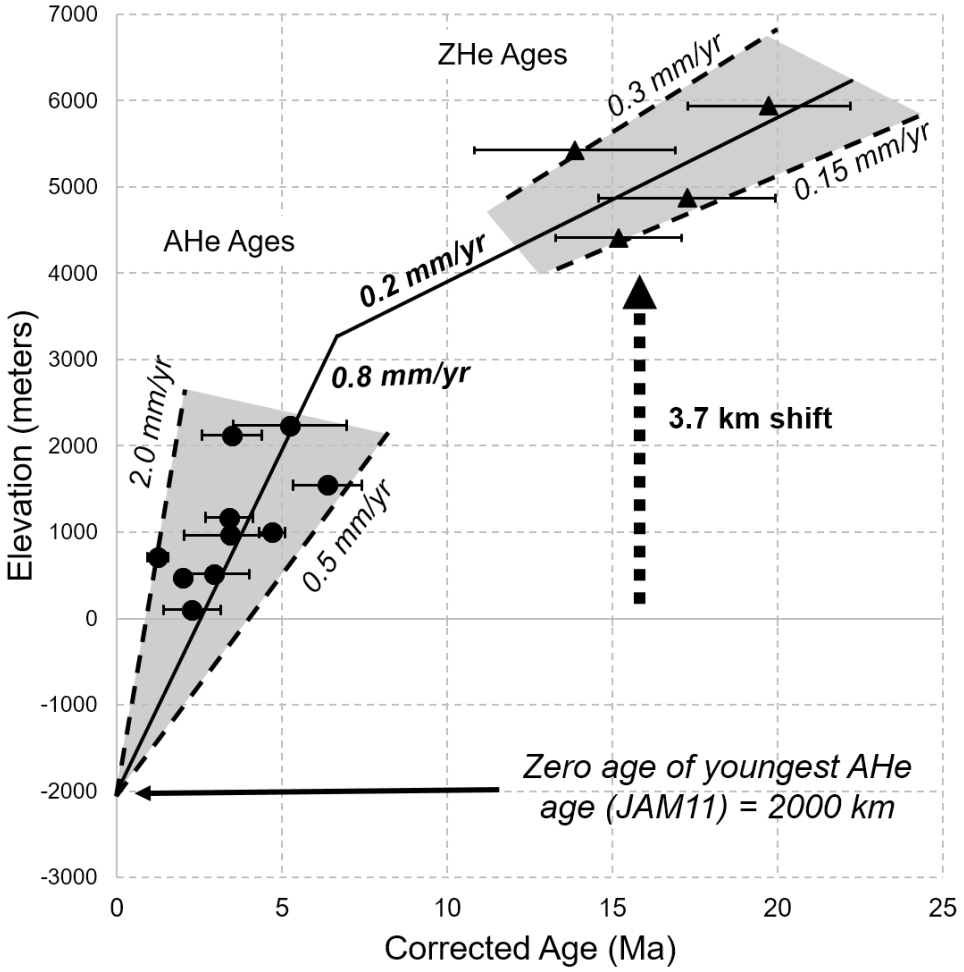

Figure 7. Pseudo-elevation-age plot of AHe and ZHe data for the Blue Mountains. The AHe includes all young ages on both the northern and southern flanks, as well as the footwall sample adjacent to the EPGF. This represents the rapid exhumation across the BMRB, including rapid footwall exhumation. Zero age calculated for the youngest sample based on bulk closure temperature equation for thermally activated diffusion (McDougall and Harrison, 1999). The ZHe ages are shifted upwards 3.7 km, based on the difference in closure temperature and 30 ^{o}C geothermal gradient. The gray represents a range of possible exhumation rates based on the errors associated with each data set.

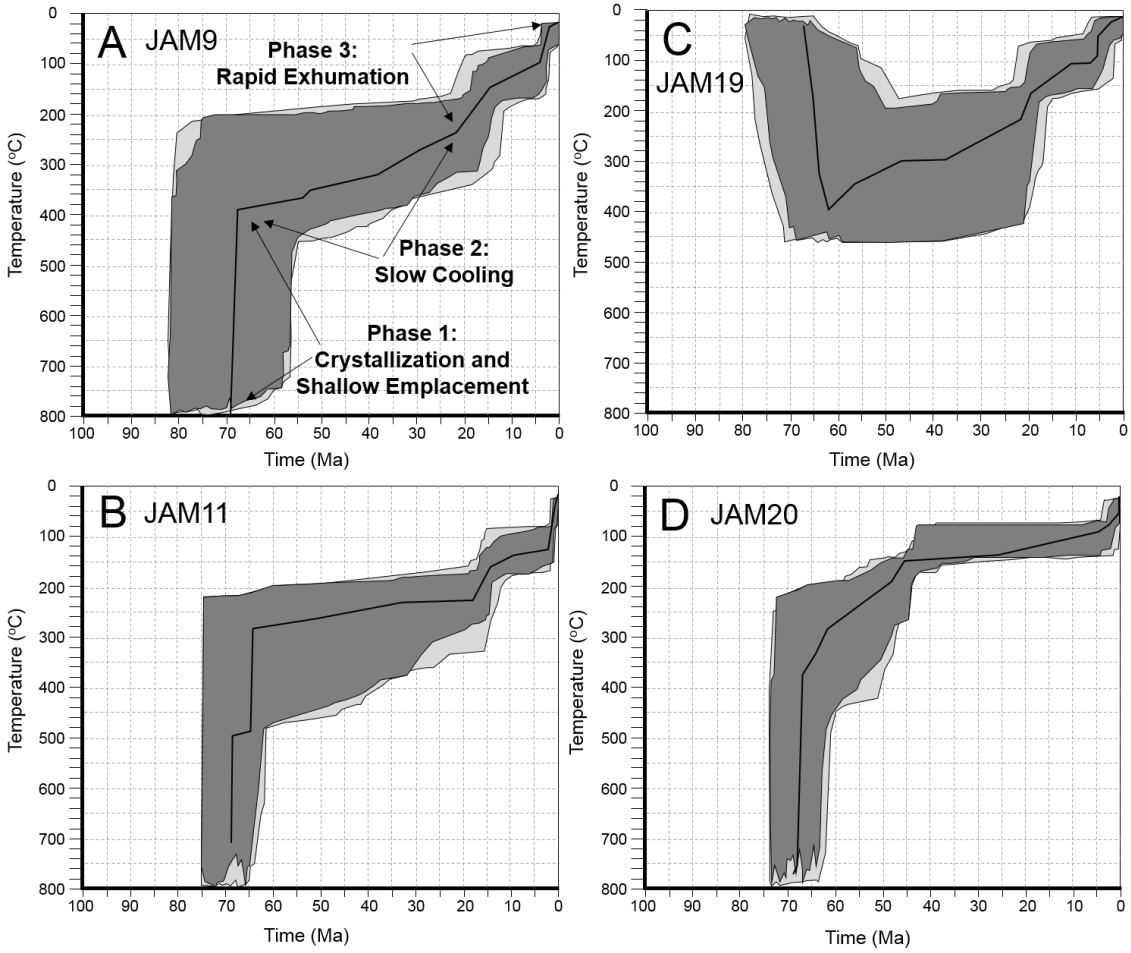

Figure 8. HeFTY inverse models of time-temperature cooling history for A) JAM9, B) JAM11, C) JAM19, and D) JAM20. The dark- and light-grey represent all the good-fit and acceptable-fit pathways, respectively, based on Ketcham (2005) and the input model parameters, including: He, Th, and Sm concentrations, calibrations of activation energy and geometry from Farley (2000), alpha particle distance from Ketcham et al. (2011), and corrected ages from thermochronometric (i.e. AHe and ZHe) analyses. The good-fit and acceptable-fit paths based on a Monte Carlo simulation of the data, with the best-fit line for the specific run as the black line. For all models, each pathway was halved 2 times for simplicity in the model. Models of the plutonic rocks (A, B, D) show three phases of cooling: 1) Crystallization and shallow emplacement in the Late Cretaceous; 2) Prolonged stasis and slow cooling from Paleocene to middle Miocene; and 3) Rapid exhumation from middle Miocene to present, involving two stages of exhumation: ~20-5 Ma at 0.2 mm/yr, and 5 Ma-Present at ~1.0 mm/yr. For our sedimentary sample (C), burial to a depth large enough to force total reset of closure system. Following a period of gradual exhumation, ~6 Ma shows a potential increase in exhumation rate. All models represent a period of rapid exhumation beginning ~5 Ma and lasting until the Present day.

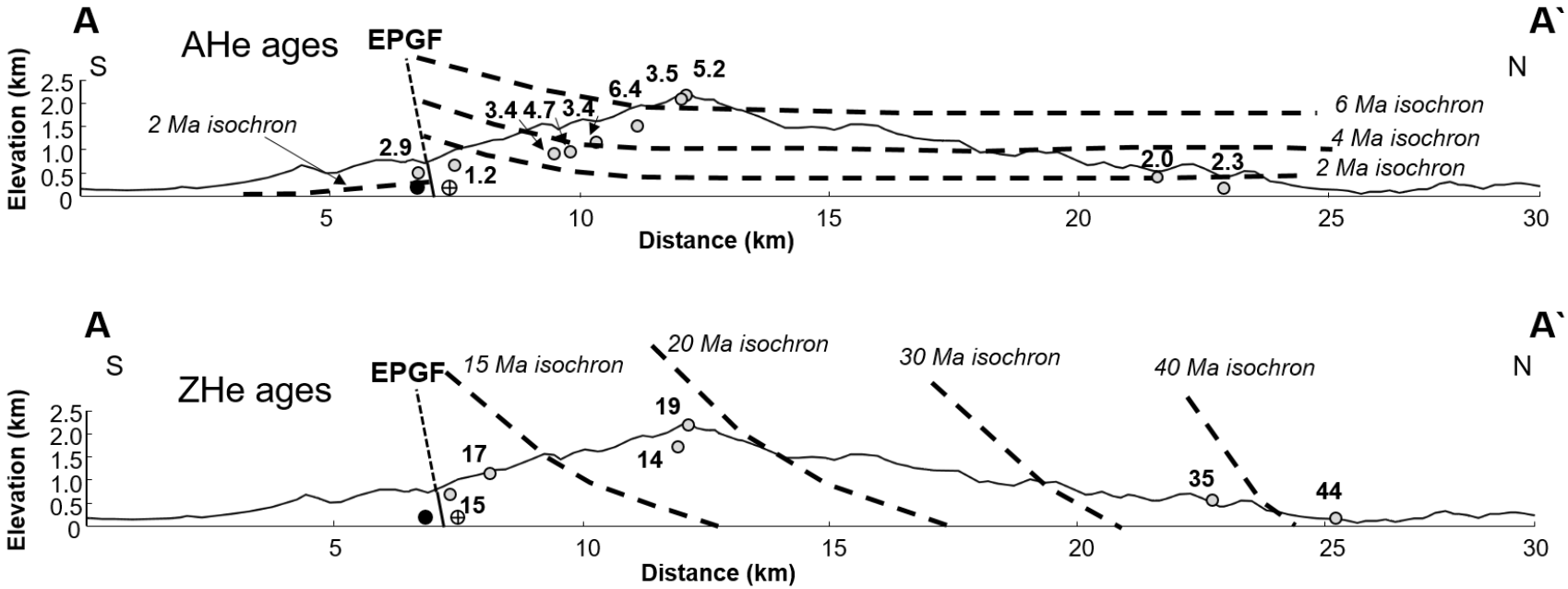

Figure 9. Age-distance plots for AHe (top) and ZHe (bottom) along topographic profile from south to north within the Blue Mountains (A-A'; see Fig. 4 for profile location). Isochron positions are generalized and approximate, taking into account variation in ages and uncertainties. AHe age isochrons are flat across most of the range, indicating rapid exhumation in the core and flanks of the BMRB, although slightly greater rock uplift directly along the fault. ZHe isochrons are tilted upwards to the south, due to the northward increase in ZHe age. The difference in these isochron patterns indicates changes in the style of deformation from ZHe to AHe closure, and how exhumation patterns have changed due to advection of crust into the bend.

2.11.0 SUPPLEMENT MATERIAL

Section 1.

Table 1. $^{40}Ar/^{39}Ar$ step heating experiments for JAM20, amphibole.

Step	*Temp	^{40}Ar (moles)	^{40}Ar (volts)	s_{40} (volts)	^{39}Ar (volts)	s_{39} (volts)	^{38}Ar (volts)	s_{38} (volts)	$^{*37}Ar$ (volts)	s_{37} (volts)	^{36}Ar (volts)
A	650	7.95E-14	0.405327	0.000707	0.000897	0.000011	0.001130	0.000022	0.002591	0.000032	0.001343
B	850	6.77E-14	0.345080	0.000667	0.011415	0.000046	0.003424	0.000030	0.048322	0.000102	0.000940
C	950	5.84E-14	0.297635	0.000646	0.007508	0.000035	0.001477	0.000021	0.007754	0.000044	0.000843
D	1050	5.78E-14	0.294629	0.000707	0.019097	0.000053	0.006896	0.000041	0.049981	0.000112	0.000625
E	1100	9.17E-14	0.467271	0.000701	0.042715	0.000072	0.030346	0.000070	0.209224	0.000181	0.000960
F	1150	2.75E-13	1.403913	0.000874	0.154781	0.000170	0.122249	0.000151	1.164819	0.000460	0.002884
G	1200	9.04E-14	0.460549	0.000695	0.045840	0.000082	0.033821	0.000077	0.316134	0.000201	0.000982
H	1250	6.71E-14	0.341817	0.000661	0.035563	0.000073	0.027878	0.000068	0.247479	0.000191	0.000677
I	1300	7.40E-14	0.377324	0.000707	0.042006	0.000063	0.031698	0.000070	0.286281	0.000201	0.000700
J	1350	3.71E-14	0.188980	0.000632	0.018972	0.000053	0.015928	0.000057	0.140058	0.000141	0.000401
K	1450	2.29E-14	0.116821	0.000606	0.007663	0.000032	0.006672	0.000035	0.057189	0.000097	0.000283
L	1650	5.47E-14	0.279026	0.000667	0.001414	0.000019	0.001406	0.000020	0.010576	0.000053	0.000893

Step	s_{36} (volts)	$\%^{40}Ar^*$	$^{40}Ar^*/^{39}Ar_K$	s	Age (Ma)	s (Ma)	Ca/K	Cl/K	^{39}Ar (%total)	$^{39}Ar_K$ (moles)
A	0.000021	2.4	10.74881	7.28061	115.74	75.93	25.069	0.76822	0.2	1.74E-16
B	0.000021	24.8	7.58170	0.55484	82.40	5.89	36.746	0.21542	2.9	2.21E-15
C	0.000019	17.3	6.86064	0.78169	74.72	8.34	8.972	0.12930	1.9	1.47E-15
D	0.000019	43.7	6.79897	0.30097	74.07	3.21	22.751	0.27146	4.9	3.72E-15
E	0.000020	56.2	6.24209	0.15856	68.11	1.70	42.607	0.55018	11.0	8.26E-15
F	0.000024	70.6	6.54709	0.11523	71.38	1.23	65.508	0.61357	39.9	2.97E-14
G	0.000021	62.9	6.44816	0.16794	70.32	1.80	60.074	0.57190	11.8	8.81E-15
H	0.000021	68.8	6.75262	0.20174	73.57	2.15	60.658	0.60884	9.2	6.83E-15
I	0.000019	73.8	6.76854	0.17002	73.74	1.81	59.448	0.58596	10.8	8.08E-15
J	0.000019	65.4	6.65608	0.31824	72.54	3.40	64.437	0.65267	4.9	3.64E-15
K	0.000018	47.0	7.33258	0.73825	79.75	7.85	65.188	0.67502	2.0	1.47E-15
L	0.000022	6.8	13.77896	4.77057	147.07	48.90	65.397	0.68542	0.4	2.71E-16

RUN INFO

Sample:	JAM20	*Lab #:*	31062	*J:*	0.006164(15)
Mineral:	Amphibole	*D1:*	1.00676(86)	*Heating Time (s):*	600
Irradiation c	9.45	*Sensitivity (mol/volt):*	1.962E-13(45)	*39ArKTot (mol):*	7.46E-14
Mass (mg):	29.551	*Days Since Irr:*	76	*37 treatment:*	normal

JAM20, Amphibole Age Summary

	Age (Ma)	s (Ma)	Steps	39Ar (%total)	40/36i	s40/36i
Plateau Age	71.7	0.5	F-L	79.0	295.5	---
Isochron Age	70.8	0.7	A-L	100.0	302	4
Total Gas Age	72.4					

Table 2. $^{40}Ar/^{39}Ar$ step Heating Experiments for JAM20, K-spar.

Step	*Temp	^{40}Ar (moles)	^{40}Ar (volts)	s_{40} (volts)	^{39}Ar (volts)	s_{39} (volts)	^{38}Ar (volts)	s_{38} (volts)	$^{*37}Ar$ (volts)	s_{37} (volts)	^{36}Ar (volts)
A	600	6.63E-14	0.337926	0.000788	0.005971	0.000032	0.000931	0.000017	0.000091	0.000030	0.001115
B	700	6.67E-14	0.339960	0.000737	0.037963	0.000068	0.001311	0.000018	0.000320	0.000031	0.000450
C	800	1.46E-13	0.743393	0.000844	0.113724	0.000120	0.001920	0.000019	0.000792	0.000030	0.000265
D	850	1.20E-13	0.609551	0.000902	0.091890	0.000130	0.001257	0.000018	0.000470	0.000030	0.000132
E	900	1.36E-13	0.695187	0.000857	0.106208	0.000140	0.001425	0.000017	0.000440	0.000031	0.000087
F	950	2.01E-13	1.025142	0.000922	0.154051	0.000130	0.002218	0.000019	0.000479	0.000031	0.000188
G	1000	2.49E-13	1.268520	0.000876	0.191896	0.000190	0.002652	0.000024	0.000445	0.000030	0.000182
H	1050	2.61E-13	1.331736	0.000950	0.199856	0.000170	0.002680	0.000023	0.000350	0.000030	0.000164
I	1100	2.46E-13	1.252445	0.001030	0.188097	0.000160	0.002571	0.000021	0.000357	0.000030	0.000184
J	1150	2.59E-13	1.318618	0.000943	0.198800	0.000130	0.002822	0.000027	0.000562	0.000030	0.000220
K	1200	2.40E-13	1.225643	0.000863	0.180764	0.000130	0.002675	0.000022	0.000995	0.000032	0.000334
L	1250	2.76E-13	1.407007	0.001015	0.211814	0.000170	0.003500	0.000027	0.001480	0.000032	0.000338
M	1300	6.70E-13	3.415671	0.001290	0.523397	0.000270	0.010096	0.000037	0.001134	0.000033	0.000601
N	1350	1.11E-12	5.641099	0.001644	0.854238	0.000410	0.016419	0.000054	0.000605	0.000031	0.001209
O	1450	4.96E-13	2.529362	0.001100	0.368162	0.000220	0.007006	0.000041	0.000505	0.000031	0.000663
P	1650	3.38E-13	1.724663	0.001038	0.114634	0.000140	0.002771	0.000020	0.000076	0.000029	0.003311

Step	s_{36} (volts)	$\%^{40}Ar^*$	$^{40}Ar^*/^{39}Ar_K$	s	Age (Ma)	s (Ma)	Ca/K	Cl/K	^{39}Ar (%total)	$^{39}Ar_K$ (moles)
A	0.000017	2.5	1.43621	0.87461	15.87	9.62	0.135	0.08590	0.2	1.17E-15
B	0.000016	60.9	5.44828	0.12576	59.49	1.35	0.075	0.01546	1.1	7.46E-15
C	0.000015	89.5	5.84320	0.04118	63.72	0.44	0.062	0.00286	3.2	2.23E-14
D	0.000015	93.6	6.20406	0.04984	67.59	0.53	0.045	0.00045	2.6	1.81E-14
E	0.000015	96.3	6.29589	0.04484	68.57	0.48	0.037	0.00033	3.0	2.09E-14
F	0.000016	94.6	6.28607	0.03153	68.46	0.34	0.028	0.00105	4.3	3.03E-14
G	0.000015	95.8	6.32214	0.02565	68.85	0.27	0.021	0.00063	5.4	3.77E-14
H	0.000015	96.4	6.41357	0.02427	69.82	0.26	0.016	0.00033	5.6	3.93E-14
I	0.000015	95.7	6.36187	0.02601	69.27	0.28	0.017	0.00051	5.3	3.70E-14
J	0.000015	95.1	6.29838	0.02473	68.59	0.26	0.025	0.00091	5.6	3.91E-14
K	0.000015	92.0	6.22816	0.02662	67.84	0.28	0.049	0.00127	5.1	3.55E-14
L	0.000016	92.9	6.16519	0.02488	67.17	0.27	0.062	0.00268	6.0	4.16E-14
M	0.000018	94.8	6.17935	0.01266	67.32	0.14	0.019	0.00495	14.8	1.03E-13
N	0.000018	93.7	6.17741	0.01003	67.30	0.11	0.006	0.00485	24.1	1.68E-13
O	0.000018	92.3	6.33004	0.01674	68.93	0.18	0.012	0.00464	10.4	7.23E-14
P	0.000023	43.2	6.50162	0.06987	70.76	0.75	0.006	0.00471	3.2	2.25E-14

RUN INFO

Sample:	JAM20	*Lab #:*	32062-	*J:*	0.006153(15)
Mineral:	K-SPAR	*D1:*	1.00676(86)	*Heating Time (s):*	600
*Irradiation (	8.95	*Sensitivity (mol/volt):*	1.962E-13(45)	*39ArKTot (mol):*	6.96E-13
Mass (mg):	3.489	*Days Since Irr:*	77	*37 treatment:*	normal

JAM20, K-Spar Age Summary

	Age (Ma)	s (Ma)	Steps	39Ar (%total)	40/36i	s40/36i
Weightged Ave	67.9	0.60	D-O	92.3	295.5	---
Isochron Age	---	---	---	---	---	---
Total Gas Age	67.82					

Table 3. All isotopic parameters and correlative references used for step-heating experiments.

Relative Isotope Values Used			
(40Ar/36Ar)A	295.5 (0)	**Steiger and Jager, 1977	
(38Ar/36Ar)A	0.1869 (0)	**Steiger and Jager, 1977	
Interfering isotope production ratios			
(40Ar/39Ar)K	8.62E-3(142)	This study	
(38Ar/39Ar)K	1.285E-2(4)	This study	
(37Ar/39Ar)K	1.59E-4(45)	This study	
(39Ar/37Ar)Ca	6.80E-4(18)	This study	
(38Ar/37Ar)Ca	8.3E-5(19)	This study	
(36Ar/37Ar)Ca	2.78E-4(10)	This study	
(36Cl/38Cl)	316(0)	Roddick, 1983	
Ca/K multiplier	1.92(0)	Fleck et al., 1977	
Cl/K multiplier	0.794(0)	Reston Lab Data	
Decay constants			
40K lambda e	5.81E-11(0)	Steiger and Jager, 1977	/yr
40K lambda beta	4.962E-10(0)	Steiger and Jager, 1977	/yr
39Ar	7.06E-6(8)	Stoenner et al., 1965	/d
37Ar	1.975E-5(6)	Stoenner et al., 1965	/d
36Cl lambda beta	6.12E-09	Weast, 1981	/d

Relative isotope values are corrected for baseline, background, mass discrimination and radioactive decay.

**Temperature is an overestimate due to thermal lag. See text.*

****Steiger and Jager rounded published values from Nier, 1950.*

Nier's reported values correspond to 40/36A = 296.0(5) and 38/36A = 0.1880(3) (McDougall and Harrison, 1999).

Uncertainty in the last digit is reported in paranthesis.

Where no uncertainty was listed in the reference the uncertainty not included in data reduction and is listed here as 0.

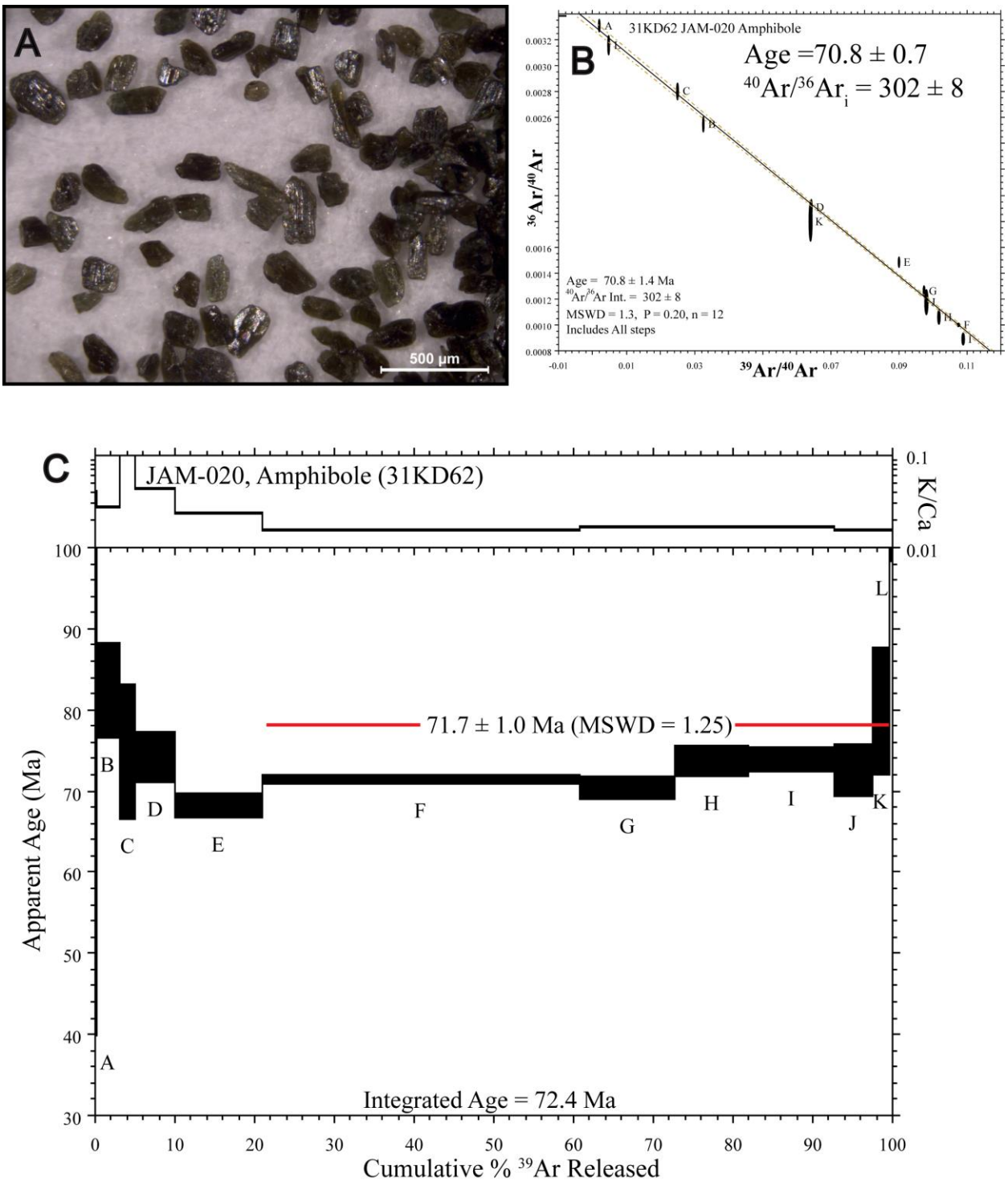

Figure 1. JAM20 - Amphibole: A) Incident light image of amphibole separate from JAM20. B) Inverse isotope correlation diagram from amphibole step heating experiment. C) Age spectrum from step-heating experiment. Note the large age uncertainty of individual steps and the low calculated K/Ca values (Plateau and correlation age given with 2σ uncertainty, individual steps plotted at 1σ).

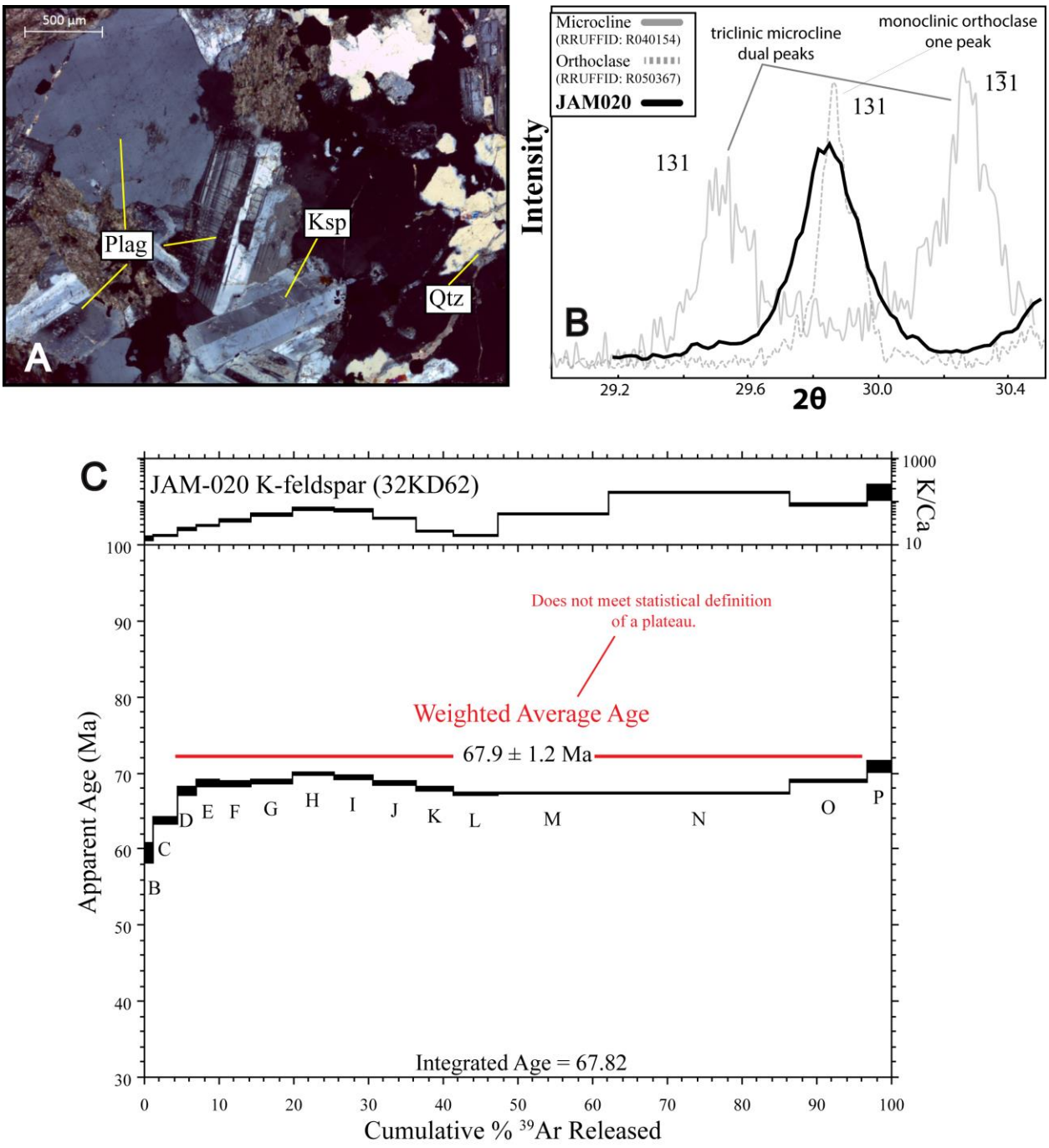

Figure 2. JAM20 – K-spar: A) Cross polarized light photomicrograph. K-feldspar grain exhibits Carlsbad twinning suggesting the K-feldspar is orthoclase. B) 2θ range of 29-30.5º from a powder x-ray diffraction pattern of the K-feldspar mineral separate (data corrected for sample displacement). The presence of a single 131 peak at ~30º indicates the K-feldspar is monoclinic and confirms the optical identification of orthoclase. Reference microcline and orthoclase XRD patterns are taken from the free online database at rruff.info. C) Age spectrum showing little variation (~2 Ma) over >90% of the ^{39}Ar/K released, consistent with rapid cooling through closure. A weighted average age for all steps is shown (uncertainty 2σ).

Section 2.

Table 1. Data table for spot zircon analyses for JAM9 and JAM20.

	Corrected Concentrations and Ratios										Apparent ages (Ma)							
Analysis	U (ppm)	206Pb 204Pb	U/Th	206Pb* 207Pb*	± (%)	207Pb* 235U*	± (%)	206Pb* 238U	± (%)	error corr.	206Pb* 238U*	± (Ma)	207Pb* 235U	± (Ma)	206Pb* 207Pb*	± (Ma)	**Best age (Ma)**	**± (Ma)**
-Jam 20 Spot 1	56	4025	1.5	21.9576	5.3	0.0663	6.0	0.0106	2.9	0.48	67.7	1.9	65.2	3.8	26.5	127.7	67.7	1.9
-SAMPLE 1 Spot 2	35	2220	2.6	22.4772	9.2	0.0652	9.6	0.0106	2.9	0.30	68.1	1.9	64.1	6.0	83.5	225.5	68.1	1.9
-SAMPLE 1 Spot 3	188	29334	1.1	21.5350	3.6	0.0656	4.1	0.0102	1.8	0.44	65.7	1.2	64.5	2.5	20.3	87.6	65.7	1.2
-SAMPLE 1 Spot 4	69	31802	1.7	19.9429	6.1	0.0758	6.5	0.0110	2.4	0.37	70.3	1.7	74.2	4.7	201.6	140.6	70.3	1.7
-SAMPLE 1 Spot 5	127	5040	2.0	21.4298	5.4	0.0694	5.8	0.0108	2.2	0.38	69.1	1.5	68.1	3.9	32.1	129.5	69.1	1.5
-SAMPLE 1 Spot 6	128	28050	2.4	19.8093	4.9	0.0751	5.3	0.0108	2.0	0.38	69.2	1.4	73.5	3.8	217.2	113.3	69.2	1.4
-SAMPLE 1 Spot 7	33	3467	2.5	19.5215	9.1	0.0752	10.1	0.0106	4.3	0.43	68.3	2.9	73.6	7.2	251.0	210.5	68.3	2.9
-SAMPLE 1 Spot 8	67	4748	1.4	19.6178	5.8	0.0749	6.3	0.0107	2.6	0.40	68.4	1.7	73.4	4.5	239.6	133.8	68.4	1.7
-SAMPLE 1 Spot 9	101	43564	1.4	19.4131	4.8	0.0752	5.4	0.0106	2.4	0.44	67.9	1.6	73.6	3.8	263.8	111.0	67.9	1.6
-SAMPLE 1 Spot 10	134	6089	2.6	20.8893	5.2	0.0692	5.6	0.0105	2.1	0.38	67.2	1.4	68.0	3.7	92.9	123.6	67.2	1.4
-SAMPLE 1 Spot 11	72	2406	3.1	23.6094	6.7	0.0612	6.9	0.0105	1.6	0.24	67.2	1.1	60.3	4.1	205.3	169.2	67.2	1.1
-SAMPLE 1 Spot 12	115	83996	2.7	20.2744	6.0	0.0726	6.5	0.0107	2.4	0.37	68.4	1.6	71.1	4.5	163.2	140.9	68.4	1.6
-SAMPLE 1 Spot 13	72	9210	2.9	20.2546	7.7	0.0735	8.0	0.0108	2.1	0.27	69.2	1.5	72.0	5.6	165.5	181.3	69.2	1.5
-SAMPLE 1 Spot 14	43	1575	2.7	25.7227	7.1	0.0573	7.4	0.0107	2.2	0.30	68.6	1.5	56.6	4.1	425.1	185.5	68.6	1.5
-SAMPLE 1 Spot 15	85	36164	1.6	19.6835	6.1	0.0751	6.7	0.0107	2.9	0.43	68.7	2.0	73.5	4.8	231.9	140.0	68.7	2.0
-SAMPLE 1 Spot 16	90	3863	2.5	22.9574	5.6	0.0640	6.1	0.0107	2.4	0.39	68.4	1.6	63.0	3.7	135.5	139.2	68.4	1.6
-SAMPLE 1 Spot 17	104	19655	1.4	20.3168	5.3	0.0715	5.7	0.0105	2.1	0.37	67.6	1.4	70.2	3.8	158.4	123.1	67.6	1.4
-SAMPLE 1 Spot 18	82	31297	1.4	20.2964	5.3	0.0733	5.7	0.0108	2.1	0.37	69.2	1.5	71.8	3.9	160.7	123.5	69.2	1.5
-JAM9 Spot 36	132	19564	2.4	20.3047	4.2	0.0801	4.6	0.0118	1.9	0.40	75.6	1.4	78.2	3.5	159.7	98.9	75.6	1.4
-Sample 2 Spot 37	220	23848	1.7	20.1703	3.1	0.0791	3.3	0.0116	1.3	0.38	74.1	0.9	77.3	2.5	175.2	72.2	74.1	0.9
-Sample 2 Spot 38	349	37347	1.2	20.7150	3.2	0.0784	3.7	0.0118	1.9	0.51	75.4	1.4	76.6	2.8	112.7	76.1	75.4	1.4
-Sample 2 Spot 39	155	160318	2.1	19.7998	4.5	0.0814	5.0	0.0117	2.1	0.43	74.9	1.6	79.5	3.8	218.3	105.2	74.9	1.6
-Sample 2 Spot 40	215	33435	1.8	20.7763	3.0	0.0776	3.5	0.0117	1.7	0.49	75.0	1.3	75.9	2.5	105.7	71.6	75.0	1.3
-Sample 2 Spot 41	288	20076	1.5	20.4826	3.7	0.0792	4.1	0.0118	1.7	0.40	75.4	1.2	77.4	3.0	139.3	87.8	75.4	1.2
-Sample 2 Spot 42	125	6159	2.4	21.6234	4.9	0.0752	5.2	0.0118	1.5	0.29	75.6	1.1	73.6	3.7	10.5	118.8	75.6	1.1
-Sample 2 Spot 43	169	9035	2.2	20.7768	5.2	0.0787	5.4	0.0119	1.6	0.30	76.0	1.2	76.9	4.0	105.7	121.8	76.0	1.2
-Sample 2 Spot 44	329	20696	1.1	21.2289	3.0	0.0746	3.2	0.0115	1.2	0.38	73.6	0.9	73.0	2.3	54.6	71.2	73.6	0.9
-Sample 2 Spot 46	250	32775	1.6	20.8024	3.2	0.0781	3.6	0.0118	1.7	0.48	75.5	1.3	76.3	2.6	102.8	74.6	75.5	1.3

Spot analyses for JAM9 and JAM20 zircons
Concentrations based on measurement of standards (see 3.1, Data Analysis)
Apparent ages based on isotopic ratios of $^{206}Pb/^{238}U$, $^{207}Pb/^{235}U$, $^{206}Pb/^{207}Pb$
Best ages are used for the concordia diagrams below
Errors reported are 1σ
**corrected for common Pb concentrations and fractionation (Gehrels et al., 2008)*

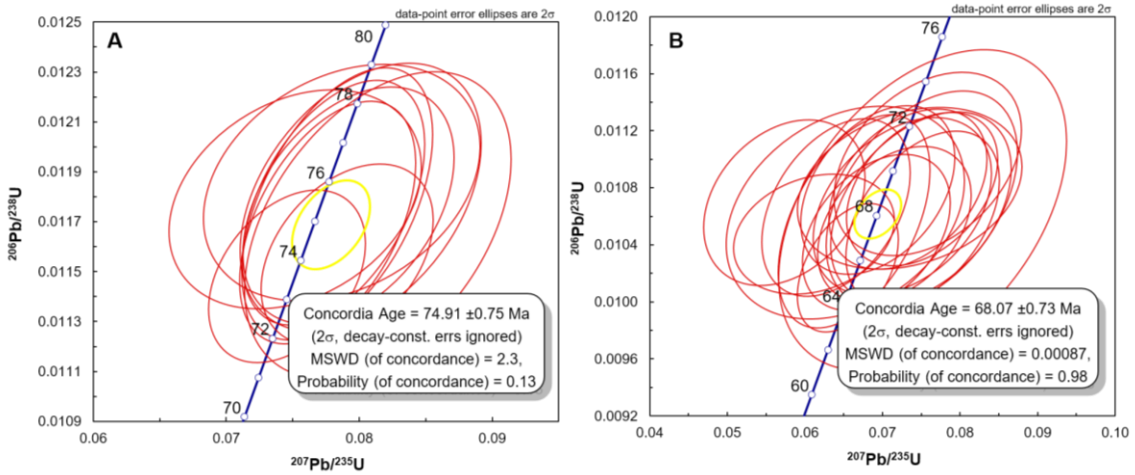

Figure 1. U/Pb concordia plots of $^{206}Pb/^{238}U$ vs. $^{207}Pb/^{235}U$ from spot zircon analysis for A) JAM9 and B) JAM20. Red ellipses are individual measurements and the yellow ellipses is the average.

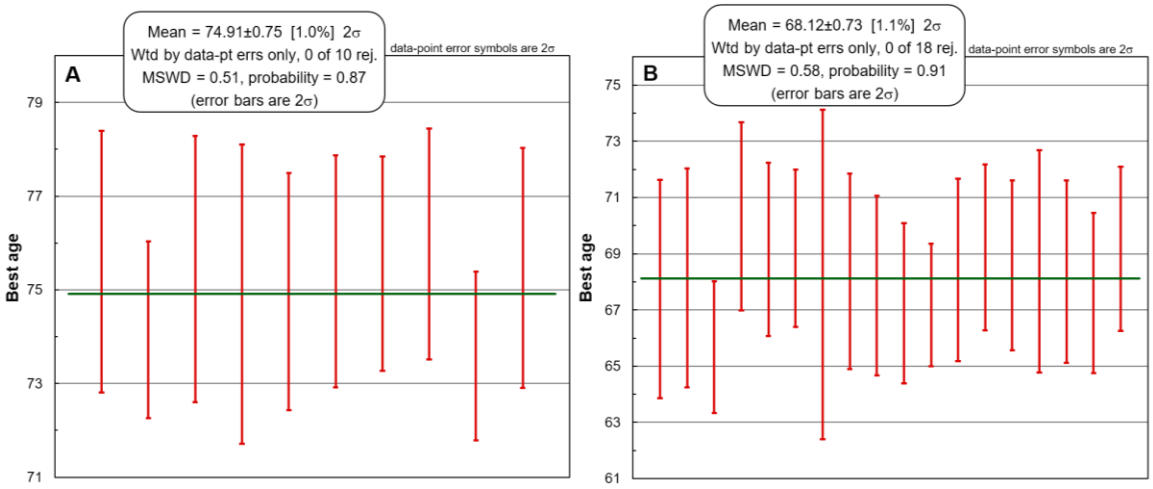

Figure 2. Probability density function of the "Best-age" calculated in U/Pb data table for A) JAM9 and B) JAM20. Note that out of all 28 zircons analyzed, zero were rejected due to large uncertainties.

Section 3.

Table 1. Full data table for ZHe measurements, including F_T corrections, and all relevant measurements.

Sample	He (pmol)	He±1s (pmol)	U (ng)	U±1s (ng)	Th (ng)	Th±1s (ng)	Zr (ng)	Zr±1s (ng)	Th/U	mass zirc (g)	U (ppm)	Th (ppm)	4He/g (nmol)	Ft 238U	Ft 235U	Ft 232Th	Ft 147Sm	Rs (um)	Raw age (Ma)	Corrected age (Ma)	1s age (Ma)	Average Age (Ma)	Standard Deviation
JAM6_Z1	0.0345	0.0005	0.3818	0.0055	0.1865	0.0027	1344.5029	21.3766	0.5012	2.70E-06	141.31	69.03	12.78	0.721	0.682	0.682	0.911	42.60	15.03	21.00	0.41		
JAM6_Z2	0.0290	0.0003	0.4200	0.0060	0.2183	0.0032	1377.6537	21.6911	0.5332	2.77E-06	151.73	78.86	10.49	0.719	0.680	0.680	0.910	42.37	11.42	15.99	0.25		
JAM6_Z3	0.0150	0.0002	0.1566	0.0023	0.0886	0.0013	759.2931	11.9365	0.5802	1.53E-06	102.67	58.07	9.83	0.686	0.642	0.642	0.899	37.38	15.65	23.03	0.48	13.86	3.04
JAM6_Z4	0.0080	0.0002	0.1889	0.0028	0.1034	0.0015	643.3132	10.4741	0.5617	1.29E-06	146.16	80.02	6.21	0.679	0.635	0.635	0.896	36.49	6.98	10.38	0.28		21.9%
JAM6_Z5	0.0181	0.0002	0.2915	0.0042	0.1467	0.0021	835.6473	13.4560	0.5164	1.68E-06	173.60	87.38	10.79	0.684	0.640	0.640	0.898	37.11	10.30	15.20	0.24		
JAM6_Z6	0.0579	0.0010	0.3302	0.0054	0.1839	0.0032	1093.5984	16.8753	0.5714	2.20E-06	150.25	83.69	26.37	0.730	0.692	0.692	0.914	44.25	28.71	39.58	0.87		
JAM9_Z1	0.0744	0.0005	1.0545	0.0152	0.6832	0.0097	1668.0326	26.6114	0.6646	3.35E-06	314.61	203.82	22.20	0.762	0.728	0.728	0.924	50.69	11.34	14.99	0.21		
JAM9_Z2	0.1035	0.0007	1.4074	0.0202	0.8514	0.0122	2578.6850	43.0923	0.6206	5.18E-06	271.60	164.32	19.98	0.786	0.754	0.754	0.932	56.65	11.93	15.29	0.21	17.25	2.67
JAM9_Z3	0.0560	0.0004	0.6022	0.0088	0.2874	0.0041	1601.2068	25.1762	0.4895	3.22E-06	187.18	89.31	17.41	0.753	0.718	0.718	0.922	48.76	15.49	20.68	0.30		15.5%
JAM9_Z5	0.2774	0.0046	2.9056	0.0418	1.9224	0.0277	6566.5947	98.9270	0.6788	1.32E-05	220.20	145.69	21.02	0.851	0.829	0.829	0.954	83.34	15.30	18.06	0.37		
JAM11_Z5	0.0678	0.0012	1.0101	0.0146	0.4161	0.0060	4145.2520	62.5544	0.4226	8.33E-06	121.26	49.96	8.13	0.830	0.804	0.804	0.947	72.32	11.34	13.71	0.29		
JAM11_Z6	0.0030	0.0001	0.7868	0.0113	0.3328	0.0048	4658.6821	71.2125	0.4340	9.36E-06	84.05	35.55	0.32	0.837	0.812	0.812	0.949	75.68	0.64	0.77	0.02	15.18	1.91
JAM11_Z7	0.1291	0.0009	1.5921	0.0230	0.7679	0.0111	2468.8602	37.0217	0.4948	4.96E-06	320.92	154.78	26.03	0.782	0.751	0.751	0.931	55.79	13.50	17.34	0.25		12.6%
JAM11_Z8	0.0192	0.0002	0.2888	0.0042	0.1200	0.0018	2225.2177	33.4705	0.4264	4.47E-06	64.58	26.84	4.30	0.780	0.748	0.748	0.930	55.12	11.25	14.49	0.22		
JAM16_Z1	0.1965	0.0015	0.7580	0.0109	0.6359	0.0092	1936.9714	29.2265	0.8607	3.89E-06	194.74	163.38	50.50	0.757	0.722	0.722	0.923	49.54	40.02	53.30	0.75		
JAM16_Z2	0.2603	0.0018	1.7718	0.0256	0.5266	0.0077	2127.2051	33.1222	0.3049	4.27E-06	414.50	123.20	60.89	0.776	0.743	0.743	0.929	54.03	25.43	32.89	0.49	34.73	2.60
JAM16_Z3	0.0725	0.0010	0.4440	0.0064	0.1888	0.0028	1556.7888	23.7654	0.4363	3.13E-06	141.93	60.36	23.18	0.755	0.720	0.720	0.922	49.15	27.48	36.57	0.69		7.5%
JAM19_Z1	0.0129	0.0002	0.1815	0.0026	0.0673	0.0010	966.3002	14.8386	0.3802	1.94E-06	93.46	34.63	6.67	0.723	0.684	0.684	0.911	43.03	12.16	16.91	0.34		
JAM19_Z2	0.0439	0.0006	0.3508	0.0051	0.1759	0.0025	1087.8160	16.7077	0.5143	2.19E-06	160.49	80.46	20.07	0.723	0.685	0.685	0.911	43.04	20.72	28.83	0.55		
JAM19_Z3	0.0117	0.0002	0.1370	0.0020	0.0682	0.0010	704.3182	10.7111	0.5104	1.42E-06	96.83	48.18	8.26	0.686	0.643	0.643	0.899	37.43	14.15	20.79	0.44	19.73	2.47
JAM19_Z4	0.0690	0.0009	0.5144	0.0074	0.2998	0.0043	1724.6935	25.9313	0.5979	3.47E-06	148.44	86.52	19.90	0.762	0.728	0.728	0.925	50.77	21.83	28.81	0.53		12.5%
JAM19_Z5	0.0303	0.0004	0.3388	0.0049	0.2159	0.0032	663.7552	10.4121	0.6537	1.33E-06	254.02	161.86	22.73	0.678	0.634	0.634	0.896	36.36	14.42	21.49	0.40		
JAM20_Z1	0.0888	0.0012	0.4446	0.0064	0.2823	0.0041	1153.3153	17.6623	0.6512	2.32E-06	191.86	121.79	38.32	0.729	0.691	0.691	0.913	44.03	32.15	44.43	0.80		
JAM20_Z2	0.1956	0.0025	1.0064	0.0145	0.4763	0.0070	1313.0210	20.4725	0.4855	2.64E-06	381.44	180.52	74.13	0.742	0.705	0.705	0.918	46.36	32.36	43.88	0.79	44.15	0.39
JAM20_Z3	0.0202	0.0003	0.3317	0.0048	0.1267	0.0018	1889.9888	28.6084	0.3918	3.80E-06	87.34	33.36	5.33	0.812	0.784	0.784	0.941	65.10	10.38	12.84	0.25		0.9%

All measurements provide 1s (1 sigma) error
F_T is alpha correction factor for a given grain geometry, needed for corrected age

Chapter Three

Incipient evolution of the Eastern California shear zone through the transpressional zone of the San Bernardino Mountains, CA

AUTHORS:

William J. Cochran[1], James A. Spotila[1], Philip S. Prince[1]

[1]*Department of Geosciences, 4044 Derring Hall, Virginia Tech, Blacksburg, VA 24061, USA, cwill13@vt.edu, spotila@vt.edu*

Keywords: Strike-slip fault, high-resolution topography, UAV, transpression, San Bernardino Mountains

3.0.0 ABSTRACT

Measuring long-term accumulation of strike-slip displacements and transpressional uplift is difficult where strain is accommodated across wide shear zones, as opposed to a single major fault. The Eastern California Shear Zone (ECSZ) in southern California accommodates dextral shear across several strike-slip faults and is potentially migrating and cutting through a formerly convergent zone of the San Bernardino Mountains (SBM). The advection of crust along the San Andreas fault to the SE has forced these two tectonic regimes into creating a nexus of interacting strike-slip faults north of San Gorgonio Pass. These elements make this region ideal for studying complex fault interactions, evolving fault geometries, and deformational overprinting within a wide shear zone. Using high-resolution topography and field mapping, this study aims to test whether diffuse, poorly formed strike-slip faults within the uplifted SBM block are nascent elements of the ECSZ. Topographic resolution of ≤ 1m was achieved using both lidar and UAV surveys along two Quaternary strike-slip faults, namely the Lake Peak fault and Lone Valley faults. Although the Lone Valley fault cuts across Quaternary alluvium, the geomorphic expression is obscured, and may be the result of slow slip rates. In contrast, the Lake Peak fault is located at high elevations north of San Gorgonio Peak in the SBM and displaces Quaternary glacial deposits. Even with very high-resolution mapping, determining fault offset is difficult; however, the Lake Peak fault does display evidence for minor right-lateral displacement, where the magnitude of slip would be consistent with individual faults within the ECSZ (i.e. ≤ 1 mm/yr). Compared to the preservation of displacement along strike-slip faults located within the Mojave Desert, the erosive nature of the mountainous landscape adds complexity for measuring fault offset. The distribution of strain across the entire SBM block, the slow rates of slip, and the geomorphic expression of these faults add difficulty for assessing fault-slip evolution.

3.1.0 INTRODUCTION

The transient evolution of continental transforms along obliquely deforming zones provides a window into the complexity of fault-strand development and crustal deformation (Cunningham and Mann, 2007). Complex fault patterns are commonly observed along nascent shear zones and are known to include conjugate fault sets, fault overprinting, and fault slip partitioning result in dynamic rupture patterns (Harris and Day, 1993; Magistrale and Day, 1999; Rubin, 1996; Segall and Pollard, 1980). Along the southern San Andreas fault (SAF) system near San Gorgonio Pass (SGP), the activity, seismogenic role, and likelihood of through-going rupture of several major fault strands have been extensively debated (e.g. Kendrick et al., 2015; Morton and Matti, 1993; Yule, 2009; Yule and Sieh, 2003). An additional complication to this nexus of interacting fault strands is its proximity to the Eastern California shear zone (ECSZ) (Fig. 1). Although many researchers have focused on faults within the ECSZ (Herbert et al., 2014; Oskin et al., 2007; Spinler et al., 2010; Thatcher et al., 2016), little work has been done assessing fault kinematics on smaller, dextral faults located within the San Bernardino Mountains (SBM) that connect the ECSZ to the SAF. Understanding how slip is transferred through the SBM on these little-studied faults provides additional constraints on fault development in obliquely convergent shear zones.

The complex connection between the ECSZ and SAF in the vicinity of SGP embodies three fundamental problems related to continental transform fault behavior. First, the possibility of a developing structural connection between the fault systems in the SBM relates to the problem of how discontinuous fault strands in shear zones integrate into through-going fault systems with progressive slip. Strike-slip faults are thought to lengthen and integrate by linking through gaps in faulting and become smoother with increasing deformation (Wesnousky, 1988).

Yet this behavior is difficult to document, and faults may instead remain poorly integrated due to ongoing alteration and development of step-overs (i.e. slip-strengthening) (Buscher and Spotila, 2007; Cowgill et al., 2004; Gomez et al., 2007). Second, the overlap between diffuse shear and transpressional deformation in the vicinity of the SBM relates to the problem of how secondary deformation advects along either side of a fault bend. Both sides of a strike-slip fault may move equally with respect to a geometric fault feature, but in some cases, it appears that propagation, or shunting, of adjacent, evolving transpressional or transtensional deformation fields may occur at variable rates (Anderson, 1990; Burkett et al., 2016; Wakabayashi, 2007). Finally, the possibility that short, discontinuous structures play a role in accommodating deformation in the southernmost ECSZ may be relevant for understanding the discrepancy between geodetically and geologically determined slip rates (Blisniuk et al., 2010; Herbert et al., 2014; McGill et al., 2013; McGill et al., 2015; Oskin et al., 2008; Spinler et al., 2010; Spotila and Anderson, 2004; Thatcher et al., 2016). This discrepancy has been attributed to off-fault deformation along poorly-constrained, short structures (Herbert et al., 2014; Shelef and Oskin, 2010), some of which were not even identified until they experienced historical rupture (Sieh et al., 1993). However, a complete kinematic picture of the ECSZ-SAF connection will not be acquired until all relevant structures have been adequately characterized.

The kinematics of slip transfer between the SAF and southern ECSZ varies to the east and west of SGP (Fig. 1). Some strands of the ECSZ appear to transfer slip indirectly to the south of their terminations at the Pinto Mountain fault into the domain of sinistral faulting and clockwise vertical axis rotation in the eastern Transverse Ranges (Fig. 1) (Carter et al., 1987). Western strands of the southern ECSZ appear instead to terminate or propagate diffusely into the convergent zone of the SBM, which lies north of the restraining bend at SGP (Fig. 1, 2) (Spotila

and Anderson, 2004; Spotila and Sieh, 2000). Although short, discontinuous northwest-trending dextral faults have been mapped in the hangingwall to the thrust faults responsible for uplifting the SBM (Fig. 2), the degree to which these provide a through-going transfer system between the ECSZ and SAF is unknown. These faults may merge with the Helendale, Old Woman Springs, and Johnson Valley faults to the north and the Mission Creek and Mill Creek faults and thrusts in SGP to the south, thereby directly feeding slip from the restraining bend into the ECSZ (Fig. 2) (Kendrick et al., 2015; Matti and Morton, 1993; Yule and Sieh, 2003). Such a connection could be nascent, propagating through a potentially dying transpressional zone that is advecting westward with respect to the bend in the SAF (Spotila and Anderson, 2004). However, little has been documented about the kinematics of these discontinuous dextral faults, and as a result the kinematics of this fault confluence are not presently understood (Yule, 2009).

The purpose of this study is test the plausibility of slip transfer from the SAF to the ECSZ via penetrative dextral shear within the hangingwall block of the SBM. Specifically, we use high-resolution topography and field mapping to assess the kinematics and evidence for recent activity along the Lake Peak and Lone Valley faults (Fig. 2). Fault mapping suggests that these faults displace previously mapped Quaternary surficial deposits (Dibblee, 1964b;1967; Miller and Cossette, 2004), but displacement along these faults is unknown. We assess these faults from the context of whether they represent the southern penetration of the ECSZ into the SBM transpressional domain and evaluate what potential they have to contribute to slip transfer from the SAF to the ECSZ. We find multiple examples for dextral shear within the SBM which display enough evidence for Quaternary faulting that this region should be considered a transfer zone of slip from the SAF to the ECSZ.

3.2.0 TECTONIC SETTING

3.2.1 San Andreas fault

The SAF system south of the "Big Bend" consists of several major fault segments and strands, which decrease in slip rate southwards as strain is transferred to other fault systems (Fig. 1, 2). The Mojave segment of the SAF accommodates ~35 mm/yr of dextral shear (Weldon and Sieh, 1985), which decreases to 25 mm/yr at Cajon Pass, where the San Bernardino strand and the San Jacinto fault diverge (Meisling and Weldon, 1989; Weldon and Sieh, 1985). Geologic slip rates of 8-15 mm/yr for the past 35 ka have been estimated for the San Bernardino strand (McGill et al., 2013). Studies suggest the San Jacinto fault initiated between 2.4 - 1.0 Ma and has accommodated 9-20 mm/yr slip during the Quaternary (Blisniuk et al., 2010; McGill et al., 2015; Spinler et al., 2010). Both the SAF and San Jacinto fault south of Cajon Pass have been characterized by temporal and spatial variation in fault behavior, and the decrease in slip southwards may in part be accommodated by a broad zone of distributed strain (Blisniuk et al., 2010; Matti and Morton, 1993).

SAF slip rate further decreases southwards through San Gorgonio Pass to ~10-14 mm/yr on the Coachella Valley segment (e.g. Behr et al., 2010). San Gorgonio Pass is a 20-km left-step between the San Bernardino and Coachella Valley strands, along which no clear, through-going trace of the SAF exists. The stepover instead consists of a complex array of dextral strike slip, reverse, and oblique normal faults, which generate fault slip transfer, off-fault deformation, and rock uplift (Matti and Morton, 1993; Spotila et al., 2001; Yule and Sieh, 2003). The SAF through the pass has been modeled as rolling over with moderate (37^{o}) northward dip to merge with the San Gorgonio Thrust system (Fuis et al., 2012), which exhibits ~2.5 mm/yr reverse slip (Yule and Sieh, 2003) but may accommodate as much as 4.5 mm/yr of reverse slip based on modeling

(Cooke and Dair, 2011). The total strike-slip motion accommodated through SGP has been estimated at ~6 mm/yr, or only one-third of the total slip coming northwards from the Coachella Valley segment (Rangel and McGill, 2016). Both geodetic and numerical modeling suggests the missing strain may be transferred north into the ECSZ (Loveless and Meade, 2011; McGill et al., 2013; Meade and Hager, 2005; Spinler et al., 2010), although the connectivity of the SAF through the pass has prompted suggestions of a possible barrier for rupture and therefore a strain accumulation zone (Yule, 2009; Yule and Sieh, 2003). South from SGP, the Garnet Hill, Banning, and Mission Creek faults integrate into the Indio Hills fault, which constitutes the main strand of Coachella Valley (Behr et al, 2010; Gold et al., 2015).

3.2.2 Eastern California shear zone

The ECSZ is a ~125 km wide zone of diffuse dextral shear involving numerous northwest-striking faults that accommodate ~25% of the motion between the Pacific and North America plates (Dibblee, 1961; Dokka and Travis, 1990a;b; Miller et al., 2001). The southern ECSZ in the Mojave Desert connects the SAF and extension in the Gulf of California with dextral shear and extension in the southwestern Basin and Range and Walker Lane (Plattner et al., 2010). Faults in the southern ECSZ have evolved diachronously since 4-6 Ma (Andrew and Walker, 2017; Glazner et al., 2002; Oskin and Iriondo, 2004; Oskin et al., 2007). Although individual faults exhibit only 1-10 km right-slip, the total dextral slip across the southern ECSZ is ~50-75 km (Andrew and Walker, 2017; Dokka and Travis, 1990a; Glazner et al., 2002). In the southern Mojave, the ECSZ consists of six discontinuous, northwest-trending, ~30-70-km-long dextral faults (i.e. Helendale, Lenwood, Camprock, Calico, Pisgah, and Ludlow faults) (Andrew

and Walker, 2017; Oskin et al., 2008), which become more northerly oriented and bifurcate into many shorter fault segments southwards towards the SAF (Fig. 2).

The SBM has several NW-trending dextral strike-slip faults which appear to connect with faults within the ECSZ (Fig. 2). To the southeast of the Helendale fault lies the NW-SE trending Lone Valley, where previous mapping suggests a possible continuation of the Helendale into this valley (Dibblee, 1964a). Along both the NE and SW sides of the valley are strong lineaments along the uplands, which we have adopted the name Lone Valley fault (NE and SW) (Fig. 2). Although rupture history along these faults is unknown, recent maps have suggest fault activity along the SW-side of the valley during the Quaternary (Miller and Cossette, 2004). Along strike of Lone Valley to the southwest lies the NNW-striking Pipes Canyon fault, where dextral offset is visible in a strong channel deflection of ~1.8 km (Fig. 2). Characterization of faults within the core of the SBM has been neglected, with notable faults including the Lake Peak fault (previously named the "Dollar Lake fault" by Spotila and Anderson, 2004) and the Deer Creek fault. The Lake Peak fault, located within the North Fork drainage of Whitewater River (Fig. 2,6), displaces Quaternary glacial deposit previously dated at 11-16 ka (Owen et al., 2003). Mapping suggests a possible connection between the Lake Peak and Deer Creek fault to the northwest, although no identifiable fault lineaments have been found (Dibblee, 1964b). The Deer Creek fault displays a prominent lineament which offsets a ridge, without any other kinematic information known. Additionally, there are several small, NW-striking faults throughout the SBM, but no information including age, displacement, and rupture history is known (Fig. 2). Many of these of these faults could be reactivated as young features, as evidence by the Cleghorn and Tunnel Ridge faults reactivation in the Pleistocene near Cajon Pass (Meisling and Weldon, 1989). Nearly all of these faults cut through erosional terrain, as opposed to depositional terrain

similar to faults within the Mojave Desert, which could be an indication as to why so little information is understood about strike-slip faulting within the SBM.

Whether these discontinuous faults are recently active, accommodate significant dextral motion, and represent a southward continuation of the ECSZ into the SBM is not known. As such, there is no clear kinematic model for how strain in the western ECSZ is transferred to the SAF in the vicinity of SGP. An additional complexity is how such a zone of strike-slip faulting could be maintained within in a stress domain that favors thrusting. Transpressional rock uplift in the SBM has been explained as the result of convergence in SGP (Spotila and Sieh, 2000) (Fig. 2). In the northern SBM, convergence has been accommodated by motion along the south-dipping North Frontal thrust system and north-dipping Santa Ana thrust, defining the broadly deformed Big Bear block (Spotila and Sieh, 2000). In the south, convergence is accommodated on more steeply dipping structures, including strands of the SAF, and results in greater magnitudes of deformation and rock uplift (Spotila et al., 1998; 2001; Spotila and Sieh, 2000). Spotila and Anderson (2004) proposed a kinematic model in which the ECSZ has penetrated only the eastern portion of the Big Bear block, thereby terminating thrust faults to the east but permitting thrust faults to the west of the Helendale fault to remain active (Fig. 2). This model does not explain the potential existence of dextral faults in the central and western SBM, however, further indicating the need for basic fault characterization.

3.3.0 METHODS

3.3.1 Study areas and approach

We conducted exploratory neotectonic mapping and characterization in remote areas of the SBM to determine the activity of previously identified northwest trending faults. Although

bedrock maps have previously been constructed for these areas at coarse scales (e.g. 1:62,500; Dibblee, 1964b), a concerted neotectonic examination of the discontinuous faults of the central and eastern SBM has not been previously completed. Because these faults occur in rugged terrain, we hypothesize that their neotectonic expression may be muted. The faults occur at high elevation, including across the >3 km high San Gorgonio Massif, and transect rugged hillslopes that presumably experience rapid erosion (Spotila and Sieh, 2000). In contrast, strands of the ECSZ to the north of the SBM have been characterized in well preserved alluvial surfaces of the Mojave Desert. This difference in geomorphic terrain may translate to a preservational bias, in which faults in the SBM may have experienced more recent fault activity than would otherwise be interpreted based on coarse mapping of muted neotectonic expressions.

We concentrated on two locations in the SBM. The Lake Peak fault in the area of Mt. San Gorgonio was characterized given its youthful geomorphic expression in satellite imagery and the possibility that it cuts previously mapped glacial moraines (Owen et al., 2003; Sharp et al., 1959). The Lone Valley fault was characterized given its proximity to and potential as an along-strike southward continuation of the Helendale fault (Dibblee, 1964a). Although the Helendale fault trace is lost at the North Frontal thrust fault and cannot be traced through Grapevine Canyon based on light detection and ranging (lidar) (Fig. 3), to the southeast there is a broad, graben-shaped valley with steep, linear valley walls that may be faulted, making it an ideal candidate for study. Miller and Cossette (2004) also mapped the Lone Valley fault as cutting Holocene alluvium in the southeastern side of this valley. Previous mapping of these faults has not benefitted from high resolution topography, however. We utilized high resolution topography from both airborne lidar and aerial photogrammetry to characterize neotectonic activity on these faults. We also synthesized all existing evidence for northwest-trending right lateral faulting

within the upper plate of thrust faults in the SBM, including analysis of fault trend relative to the main strands of the ECSZ to the north and east.

3.3.2 Data Collection

The airborne lidar survey encompassed a ~40 km^2 area along the Pinto Mountain, Mission Creek, Mill Creek, and Lake Peak faults, with a focus on the nexus of these converging strike-slip faults (Fig. 2). The survey was flown in 2016 by the National Center for Airborne Laser Mapping (NCALM) using the three-channel Optech Titan Airborne Laser Terrain Mapper (channel 1: 1550 nm; channel 2: 1064 nm; channel 3: 532 nm). The scanner parameters affect the density of the laser pulses (Table 1), with four GPS ground stations for calculating the aircraft trajectory. The survey was performed during snow-off conditions to ensure true topography was being returned from the laser sensor. A point density of 4.47 pts/m^2 was set to for consistency with existing lidar in the region.

We conducted aerial photography surveys in Fall 2016 using a DJI Phantom 3 Advanced Quadcopter, using both manual and autonomous methods for acquiring photographs. The UAV is equipped with a 12.4-megapixel camera attached to a 3-axis gimbal (angular control accuracy of ±0.02°). The camera lens has a focal length of 20 mm (i.e. 35 mm format equivalent) and aperture of f/2.8. Although the altitude above ground level varied due to topography, an average altitude of 50 m was necessary for the desired decimeter-scale resolution. Within Lone Valley, five surveys were collected along the southwestern side of the valley and combined during processing, totaling ~3,400 photos and ~0.80 km^2 (Table 2). Along the northeastern side of the valley, two surveys were combined, totaling 748 photos and ~0.27 km^2 (see Supplement). Along Lake Peak fault, the survey totaled ~780 photos for an area of ~0.26 km^2. Each individual survey

totaled 20 min of flight time with photographs taken at varying degrees of tilt to ensure high-resolution texture mapping in the later stages of processing. Ground control points were evenly spaced throughout the survey area and were recorded using a GARMIN handheld GPS unit and verified where necessary using Google Earth.

We conducted surficial field mapping of survey areas at 1:2,000 scale using traditional methods. Mapping of alluvial surfaces was based on sediment lithology, elevation, and channel incision. We also described alluvium and soil weathering profiles in local soil pits. Scarp and stream profiles were constructed later using DEMs based on the aerial photography. We also excavated the cut-bank of an ephemeral channel on the SW side of the Lone Valley where potentially faulted alluvium was observed. A photomosaic was digitized using a 12-megapixel PENTAX WG-3 GPS field camera (i.e. focal length 4.5 mm) and used as a basemap for mapping the exposed alluvial stratigraphy.

3.3.3 Data Processing

Raw lidar data was processed by NCALM and is available on the NSF OpenTopography website (www.opentopography.org). Both digital elevation models (DEMs) and digital surface models (DSMs) were generated by NCALM from point-classified lidar data, based on the time of return for each laser pulse (i.e. first return = vegetation canopy; last return = ground). We further processed the 1-m resolution DEMs in ArcMap 10.5 to generate 1-m-resolution hillshade maps. A strip map was generated from the final product along the Lake Peak fault for surficial mapping in ArcMap, for interpretation of the relationships between the different geomorphic surfaces. For further information on processing lidar data, see the NCALM website (http://ncalm.cive.uh.edu).

We processed aerial photographs using structure from motion (SfM) technology (Ullman, 1979). This method applies robust computer algorithms to traditional stereo photogrammetric techniques, whereby overlapping photographs are processed to create millions of 3D surface points (Lowe, 2004; Snavely et al., 2007). The "structure" (i.e. topography and color) of the ground surface scene, as well as the camera position and orientation, are reconstructed using overlapping photographs from multiple angles (e.g. Johnson et al., 2014). SfM is currently used for various applications, including 3D surface reconstruction of simple objects, paleoseismology (Bemis et al., 2014; Reitman et al., 2015), and neotectonics (Johnson et al., 2014; Westoby et al., 2012). We constructed DSMs of survey areas using Agisoft PhotoScan Pro. Dense point clouds were generated by creating Triangulated Irregular Networks (i.e. TINs), following the methods of Johnson et al. (2014). Using the default settings, we maximized the face count to produce DSMs with ~5 cm/pixel resolution (Table 2). In each model, we classified the point cloud to remove the vegetation by iteratively changing the height-above-ground (0.1-1.0 m) and angle (0-45°) parameters (defined relatively to the model-determined ground points) until an optimal surface model resulted. The best resulting parameters in all surveys were 0.1 m height-above-ground and 15° surface angle. Based on ground-truthing, these values remove the most vegetation while preserving underlying surface topography. Following this approach, DSMs were thereby transformed into true DEMs for interpretation of fault location and neotectonic activity. We followed a similar SfM approach for creation of a sub-mm/pixel resolution DSM from digital photographs of the potential fault exposure in Lone Valley.

3.4.0 RESULTS

3.4.1 Lone Valley

We selected Lone valley for detailed study because it lies directly along-strike of the apparent southern termination of the Helendale fault at the North Frontal thrust system (Fig. 2). The Helendale fault has one of the highest slip rates in the southern ECSZ (~1 mm/yr; Oskin et al., 2008), and for it to continue southeast, possibly to connect to the Pipes Canyon or Pinto Mountain faults, it would have to run through Lone Valley. Across the valley, there are three probable locations for such a connector fault: 1) the linear escarpment of the eastern edge of the Big Bear plateau that forms the western boundary of the valley, 2) the sharp eastern edge of the valley along Granite Peak, or 3) across the middle of the valley where Miller and Cossette (2004) mapped a northwest trending fault cutting bedrock and Holocene deposits (Fig. 3). Despite the sharpness of the eastern valley margin, a high-resolution DEM based on SfM analysis shows no geomorphic evidence for faulting (see Supplement). The slope-break consists of coarse-grained, loose granitic colluvium that is banked up against the linear edge of triangular facets. The form of these deposits are smooth and unbroken by scarps. Ephemeral drainages across these deposits appear un-deflected. We therefore conclude that if the eastern margin of Lone Valley is faulted, the fault has not been active recent enough to disturb depositional and erosional surfaces that are present.

More evidence of recent faulting is present in the center of Lone Valley. The high-resolution DEM shows that mapped fault traces locally appear as discontinuous, en-echelon lineaments (Fig. 4b), which Miller and Cossette (2004) interpreted to cut across both Pennsylvanian bedrock and presumed Holocene alluvium (Fig. 4a). These lineaments are also visible in aerial photographs on the basis of color changes and lineations, but only in a few

locations correspond to scarps demarcating elevation steps of 6-8 meters in the DEM (Fig. 4b). It's worth noting that these topographic steps occur in either Pennsylvanian bedrock only or where bedrock meets Quaternary alluvium (Fig. 4a). The alluvial surfaces along the fault include higher, more-incised surfaces of matrix-supported, fine-grained sediments of carbonate, feldspar, and granitic lithology and a prominent K-horizon with platy structure. Between these are lower surfaces that consist of fine-grained, loose, structureless alluvium. Because of the high sand and low clay content of this carbonate-rich alluvium, as well as the lack of a well-developed K-horizon, this surface is soft and does not preserve channel edges or other features. This may in part explain the lack of a well-developed scarp in Quaternary alluvium along the proposed fault. Although Miller and Cossette (2004) mapped discrete faulted bedrock domains and relative-dated alluvial surfaces, in most cases it was not possible to systematically relate these surface classifications to geomorphic features observable in the high-resolution DEM or in the field. Additional evidence for faulting along this weakly defined lineament is the deflection of numerous NE-running streams (Fig. 4b). These deflections are typically on the order of ~20-25 m and would correspond to right-lateral motion on the fault (if true offsets). Given the ambiguity in these deflections, the fact that other streams are not deflected, and the lack of ages on the relevant alluvial surfaces, we hesitate to interpret true lateral offset or speculate on slip rate based on these observations.

We observed additional evidence for faulting along this weakly defined lineament in a single exposure. Within a cut-bank of a stream channel we excavated and documented sharp discontinuities and potential offsets of alluvial beds (Fig. 5). The steep, SW-dipping contact juxtaposes coarse-grained, poorly sorted gravels (i.e. coarse sand to boulder-sized) and white, well-sorted fine-sand and clay. Rotated clasts within the coarse-grained gravel and laminated

wedge-shaped deposits of coarse sand occur along the contact. Below the coarse-grained gravel, white laminae of clay and fine sand appear to be relatively continuous across the downward projection of the discontinuity. These "layers" were found to be lenses in three-dimensions, and we were unable to map distinct, stratigraphic layers across the discontinuity. Although we did not trace the discontinuity to a master fault below these lenses, we hypothesize that deeper excavation at this site might reveal a true fault. While the termination and juxtaposition of layers along this contact could be interpreted as depositional (i.e. a buttress unconformity), the current drainage direction is orthogonal to the contact and the co-location with the lineament and deflected streams suggests a plausible tectonic origin.

The tectonic geomorphology of Lone Valley is thus somewhat ambiguous. Features across the center of the valley are roughly consistent with recent right-lateral faulting, suggesting a southeastward continuation of the Helendale fault. The minimal evidence for faulting may, however, imply a low rate of neotectonic activity. Alternatively, the poor topographic expression of this fault may be due to the poor preservation capacity of the loose deposits and vegetated surfaces of the valley.

3.4.2 Lake Peak

The discontinuous, en echelon trace of the Lake Peak fault is clearly visible in the lidar hillshade of the North Fork drainage of the Whitewater River near Mt. San Gorgonio (Fig. 6). The fault trace begins north of the confluence of the Mill Creek, Mission Creek, and Pinto Mountain faults in Hell For Sure Canyon, 2.5 km north of the Mill Creek fault, and is mappable for ~10 km northwestward to Dollar Lake. In the North Fork valley, the fault appears as a dark lineament on the northern flank of the valley above the trunk stream. Although it clearly cuts

across numerous tributary gullies, there are no clear lateral offsets (Fig. 7-8). To the northwest, the fault continues as en echelon scarps into higher elevation and cuts glacial deposits. These deposits have been mapped and dated as sharp-crested, nested end moraines and recessional loops created by cirque glaciers during the Wisconsin (Sharp et al., 1959). The fault scarp is high (up to ~20 m) and well defined in these coarse deposits (Fig. 9c-d). The fault is also visible as lineaments in older alluvium that occurs between deposits, although is not visible in active washes (Fig. 8a-d). To the northwest of the Mine Shaft Saddle, the fault continues through complex, lobate glacial deposits of the Dry Lake and Dollar Lake glaciers, but is locally lost in the complex ribbed, hummocky topography of the lower glacial deposits (Fig. 8a).

Geomorphic mapping of the fault through these deposits based on high resolution topography and field observations indicates that the fault has likely ruptured in the late Pleistocene (Fig. 7, 8, 9). The fault scarp occurs within mapped glacial deposits that are dated as ~12-16 ka based on cosmogenic dating (Owen et al., 2003). Due to the hummocky topography of these deposits and their coarse nature (typical boulder size ~1 m), there are no clear preserved offsets of geomorphic features, such as moraine edges or crests, that are evident in the LiDAR. These deposits are also locally mantled by coarse colluvium and talus derived from Mt. San Gorgonio, further obscuring interpretation of offsets (Fig. 8a-b).

The higher resolution DEM from SfM analysis of the North Fork glacier deposits shows the surface complexity of the deposits in more detail (Fig. 9a). The apparent height of the scarp through this moraine is ~22 m, but this is exaggerated due to the original steep slope of the faulted material as well as addition of boulders to the upper slope (Fig. 10c). The actual vertical separation across the fault is closer to 10 m (Fig. 9b-c). Because of the coarseness of the boulder moraine deposits, there are no clearly defined channels or levee deposits to check for lateral

displacement. However, we documented two subtle horizontal offsets of ~5 m (right-lateral) of stream channels that cut through the moraine and their respective fan deposits downstream (Fig. 9b). These channels are well-defined uphill of the scarp but are lost to the east of the fault (Fig. 9a-b). The proposed offsets are therefore based on the separation of these channels from the apex of lobate fan deposits of coarse alluvium derived from the eroding moraines (Fig. 9b). We delineated these fans in the field based on the color of fine grained matrix and lateral variations in grainsize. These slip estimates are speculative, and it is unclear whether more conclusive determinations could be made given the loose nature and rapid erosion of these coarse deposits. Figure 9d is a good example of how unstable this intermontane valley is due to the steep, eroding landscape, particularly so close (< 1 km) to Mt. San Gorgonio (Fig. 8b). Our mapping indicates loose colluvium is consistently being deposited atop the glacial moraines, skewing the true nature of fault expression, and estimation of fault offsets may be better suited to the northwest near Dry Lake or Dollar Lake glaciers. If these offsets are valid, however, they would suggest a minimum slip rate of 0.3 mm/yr based on the age of the glacial deposits.

3.4.3 Fault orientation in southern ECSZ

We compared the orientation of strike-slip faults in the SBM to the main strands of the southern ECSZ in the Mojave Desert. The trend of these faults based on published mapping and measurement using Google Earth at 1-km length increments are summarized in Figure 10. The total length of mapped northwest-striking faults in the SBM is 157 km and are grouped together roughly from south to north (locations on Fig. 2). Groupings include the Lake Peak and Deer Creek faults (faults 2, 4), the Pipes Canyon fault (fault 5), the northeast and southwest Lone Valley faults (faults (6, 7), and the remaining smaller faults from central SBM to the NFTS

(faults 1,3,8-13) (Fig. 2, 10). The average trend of these is N55°W, with a variation of ±16° (Fig. 11b). This orientation is moderately oblique to the regional compressive stress based on focal mechanisms within the SBM (N-S, ±10°) (Heidbach et al., 2016), but still favorable for strike-slip faulting. Individual faults become more northerly-trending with increasing proximity to the southern ECSZ in the north and east (Fig. 10a). More westerly trending faults also show more variability in fault trend (Fig. 10c).

The major fault strands of the southern ECSZ in the Mojave Desert are oriented more clockwise relative to those in the SBM. Mean orientation of these fault strands is N37°W (Fig. 10b), which is approximately parallel to the local small circle of relative Pacific-North America motion (N40°W; Savage et al., 2001). However, individual faults in the Mojave become more northerly trending to the south towards the Pinto Mountain fault (Fig. 10b), such that the local difference between faults in the SBM and neighboring faults of the ESCZ to the east of the SBM is more striking (Fig. 2). The angular difference in orientation of faults in the Mojave relative to the SBM is comparable to the clockwise rotation of maximum compressive stress, which is ~N28°E in the southern Mojave Desert (Hauksson et al., 2002; Heidbach et al., 2008). Individual Mojave ECSZ faults vary in orientation by 9-18°, which is similar to the variation in fault orientation in the SBM (Fig. 10a-c). This comparison reveals that faults in the SBM are similar in orientation, although systematically shifted, relative to the main strands of the southern ECSZ.

3.5.0 DISCUSSION

3.5.1 Evidence for strike-slip faulting in the SBM hanging wall

The results from this study provide two distinct examples of late Pleistocene to Holocene dextral faulting within the San Bernardino Mountains. The fault offsets we observe along both

the Lake Peak fault and Lone Valley fault are speculative and should be considered as evidence that slip may be transferred from the SAF to the ECSZ via dextral faults within the SBM. For example, the Lone Valley lies along strike from the Helendale fault to the northwest, and has been active since the Pleistocene (Oskin et al., 2008). Our data suggests that the Lone Valley fault is a likely candidate for a through-going fault in this region. Similarly, our investigations along the Lake Peak fault suggests the potential for slip transfer from the SAF northward into the SBM. To the south, the Mill Creek fault has been suggested to be inactive since ~12 ka (Michael Oskin, 2017, personal communication; Kendrick et al., 2015). South of the Mill Creek fault lies the Mission Creek fault, which has not been active since the late Quaternary, suggesting that a more favorable fault geometry which includes the Lake Peak fault may be occurring along this portion of the San Andreas fault (Kendrick et al., 2015). A relatively low rate of slip along the Lake Peak fault seems plausible due to the splaying nature of the SAF north from the Coachella Valley segment north into SGP.

The orientation of dextral faults within the eastern SBM have similarities to the southern ECSZ, where the average trend of the faults shows a more northwesterly-trend as you move from south to north across the SBM (Fig. 10a). The southern ECSZ also shows this trend in orientation (Fig. 10b), leading to the hypothesis that the NW-trending faults are older and have rotated counterclockwise to become unfavorable for slip, whereas the N-trending faults are nascent (Nur et al., 1993). This hypothesis is not strongly supported by evidence for counter-clockwise vertical axis rotation in the Mojave, however (Glazner et al., 2002; Golombek and Brown, 1988). Paleoseismic data also fail to suggest systematic evolution towards the more northerly-trending faults (Rockwell et al., 2000). We suggest that faults in the eastern SBM are more likely to be associated with the ECSZ than the SAF, due to the high-degree of variability in average trend.

While this is not a new hypothesis, connecting ECSZ with dextral faults within the SBM has yet to be suggested.

Other locations within the SBM provide strong evidence dextral shear (Fig. 11). The Pipes Canyon fault is dextrally offset by 1.8 km in two locations. One section shows a deflected channel within Pipes Canyon, and another shows an offset alluvial fan from the mouth of a major channel. No age constraints, however, exist for this fault, and it is unknown how the timing and fault kinematics relate to the regional deformation patterns. Along strike of the Lake Peak fault to the northwest, the Deer Creek fault displays evidence for Quaternary displacement, but no kinematic data exists for this fault (Spotila and Sieh, 2000). This fault is mapped to displace the much older Santa Ana thrust in the central SBM and could represent another nascent dextral fault within the SBM. In the vicinity of the Big Bear aftershock sequence, a northeast-trending linear valley could be the location of the fault which the earthquakes were generated. Since the Big Bear aftershocks did not rupture at the surface, no speculation as to a possible location of a surface fault has been conducted. Although strictly speculative, this location may provide evidence for a long rupture history, increasing the validity of earthquake hazard for the SBM.

The slip rate discrepancy between geologically- and geodetically-determined fault kinematics may be resolved if dextral faults within the SBM were added into the overall slip budget. Geodetically determined slip rates for the southern ECSZ are suggested to be ~15 mm/yr for all the main faults (i.e. Helendale-, Camp Rock-, Calico-, Lenwood-, Ludlow-, Johnson Valley-, Emerson-, and Pisgah-Bullion- faults) (McGill et al., 2015; Meade and Hager, 2005; Spinler et al., 2010), 2-3 times larger than the sum of the late Pleistocene slip rate of ~6 mm/yr across the same faults (Oskin et al., 2008). McGill et al. (2015) modeled transects across all major faults east and west of the SJF, with a total slip budget of ~47 mm/yr, ~7 mm/yr less than

the ~54 mm/yr of slip between the North American and Pacific Plates (DeMets and Dixon, 1999). While permanent, off fault deformation may be a contributing factor in the total slip deficit, our results suggest that smaller, nascent faults within the SBM must be accounted for in order to solver for the remaining 7 mm/yr of slip. While the majority of authors assume there is a slip-rate discrepancy, some studies suggest that a more complete picture of geologically determined slip rates is necessary for an accurate conclusion (Wetmore et al., 2017).

3.5.2 Kinematic model for westward migration of ECSZ

Our observations of Quaternary faulting within the predominantly transpressional system of the SBM provide an example of how far-field strain from the oblique convergence of the Pacific-North American plates is partitioned along small strike-slip faults within the hangingwall block of the SBM. This suggests that a possible mechanism for slip transfer from the SAF to the ECSZ is by accommodating dextral shear along these nascent strike-slip faults. The advection of crust into the restraining bend causes compression along the sides of the uplifting zone, namely the SGP and North Frontal thrust system, while the SAF continues to translate crust towards the southeast into the ECSZ. This mechanism of a migrating restraining bend progressively abandoning older deformed crust and increasing complex fault interaction along zones of transpression (Wakabayashi, 2007) has been observed along several transpressional systems, including the San Gabriel Mountains (Buscher and Spotila, 2007; Meisling and Weldon, 1989), the Alaska Range (Bemis et al., 2015; Benowitz et al., 2011; Burkett et al., 2016), and Santa Cruz Mountains (Anderson, 1990; Schwartz et al., 1990). Thus, the progressive migration of the SBM restraining bend towards the southeast inevitably causes the hangingwall block to become influenced by the ECSZ.

We present a conceptual "meat slicer" model for how the migration of the restraining into the ECSZ, based on previous research for the Quaternary activity along the NFTS (Spotila and Anderson, 2004) and the results from this study (Fig. 13). Spotila and Anderson (2004) suggested a disparity in Quaternary activity along the NFTS, whereby the eastern portion of the NFTS (i.e. east of the Helendale fault) appeared to be inactive and the western portion showed evidence for deformation within Quaternary gravel deposits. These results provide an explanation for how these co-active intersecting faults create a quasi-stable quadruple junction with different stress regimes acting on the same volume of crust. Our results in Lone Valley support this hypothesis, whereby the eastern NFTS is inactive due to the translation of the SBM into the ECSZ. As the SBM are translated towards the southeast along the SAF, the ECSZ progressively causes shearing within the hangingwall block of the SBM. Nascent strike-slip faults begin to form within the SBM as dextral shear becomes the dominant mechanism for deformation, especially along the eastern edge of the SBM where there is evidence for Quaternary deformation along the Lone Valley and Pipes Canyon faults (Fig. 13). Similarly, there is a northward migration of faulting along the SAF from SGP into the SBM. Here, researchers suggest the inactivity of two main strands of the SAF, namely the Mission Creek and Mill Creek faults, and show a progression of inactivity through time from south to north (e.g. Kendrick et al., 2015). The reorganization of fault geometry to produce a least-work means fault geometry has been suggested through modeling transpressional systems in wet kaolin, citing the Mission/Mill Creek faults as a natural system for this process (e.g. Cooke et al., 2013). While this model supports our hypothesis, we suggest that the SBM restraining bend is evolving from the south through a northward progression of nascent faults, and by the east due to the progressive translation into the ECSZ.

3.5.3 Implications for neotectonic studies on interacting fault systems

Another implication for the deformation observed within the SBM is the conjugate fault sets observed within the hangingwall of the NFTS. The area has been observed to be seismically active, most notably associated with the Big Bear "aftershock" of M>6 after the 1992 Landers rupture sequence whereby the most likely fault which ruptured was left-lateral (Jones and Hough, 1995). While our results provide evidence for dextral shear to be the dominant mechanism for deformation due to the influence of the ECSZ and SAF, the left-lateral focal mechanism for the Big Bear earthquake suggests complex stresses are coeval on longer timescales. This quasi-pure shear deformation has been observed in central Honshu, Japan, where the hangingwall of the upper plate is accommodating deformation within a predominantly compressive setting through small, conjugate left-and right-lateral strike slip faults (Yeats et al., 1997). Large, non-subduction related earthquake rupture has occurred along these faults, most notably the 1891 Mw = 7.5 Nobi earthquake (Wells and Coppersmith, 1994). While the dominant mechanism for deformation in the region is compressive deformation, these smaller faults play an active role in the evolution of the upper plate.

The rupture characteristics of the Landers 1992 earthquake sequence should be considered as a possible mechanism for rupture within the eastern SBM. During the Landers earthquake sequence, the location of aftershocks both north and south of the location of the initial rupture is telling as to the stress changes on local fault strands (Sieh et al., 1993). The propagating rupture sequence after the main shock provided empirical evidence that through-going rupture is possible along disconnected fault strands (Sieh et al., 1993; Wald and Heaton, 1994). Similarly, our results suggest a possible connection between the Helendale, Lone Valley,

and Pipes Canyon fault, simulating the potential for a minimum along-strike rupture distance of ~80 km. Adding in the potential for the rupture to cross the Pinto Mountain fault and connect to the Eureka Peak fault zone increases a maximum possible magnitude to Mw>7. While this is very much speculative, our "meat slicer" model does suggest a potentially through-going rupture sequence along the eastern edge of the SBM.

A final implication of our research involves the relative difficulty for estimating fault kinematics within a predominantly erosive geomorphic environment. Generally, fault kinematic studies involve field mapping along older, preserved depositional surfaces, similar to studies within the Mojave Desert (e.g. Oskin et al., 2007; Oskin et al., 2008). Our research provides a unique example of the challenges faced when trying to estimate fault offset using a classical approach, including: 1) young, cohesionless sediments subject to redistribution; 2) channel migration within the cohesionless sediments provide difficulty for using classical geomorphic markers (e.g. piercing points and offset channel terraces); 3) several modes of erosion, such as gravitational sliding, landslides, and debris fans, influencing the geometry of fault scarps at relatively high-elevations. This could be the reason why so little neotectonic research has been conducted within the SBM. While we do acknowledge the non-unique solution along each of the studied faults in this study, we wish to shed light on the unique geomorphic setting in which our study was conducted, providing an example of neotectonic research within a dominantly erosive setting.

3.6.0 CONCLUSIONS

Our results provide first-order evidence on incipient dextral strike-slip faulting within the SBM, focusing on two locations of previously mapped strike-slip faults which cut across

Quaternary age geomorphic surfaces. In Lone Valley, high-resolution UAV surveys reveal a series of right-laterally deflected streams and 6-8-meter-high topographic steps which cut through soft, loose alluvial sediments. The tectonic geomorphic expression, however, is somewhat ambiguous, and may reflect low rates of fault slip due to the preservation capacity within the valley. Although the cut-bank in an ephemeral stream shows juxtaposition of coarse gravel with fine sand and clay along strike of the proposed location of the Lone Valley fault, no master fault was found at depth. Similarly, the Lake Peak fault displays a prominent topographic step ~10 meters which cuts across Pleistocene glacial deposits, only speculative offsets of ~5 meters in alluvial fan deposits could be determined. We believe the lack of geomorphic expression is the result of the high-erosion capacity associated with debris from Mt. San Gorgonio. While our focus on the aforementioned faults provide some evidence for dextral faulting, several other locations faults within the SBM also display classic strike-slip faulting expression (Sylvester, 1988). Linear valleys, deflected streams, displaced ridges and alluvial fans suggest not only is strike-slip faulting prevalent within the SBM, but that a more complete log of fault kinematics is necessary for understanding how slip is transferred from the SAF to the ECSZ. We hypothesize that a more detailed kinematic history of dextral shear within the SBM may provide the necessary information to account for the overall slip deficit from the SAF to the ECSZ.

3.7.0 ACKNOWLEDGEMENTS

We would like to thank the folks at Whitewater Nature Preserve for hospitality and help with discovering best routes and trails to take. Support for this study was provided by National Science Foundation grant EAR-1145115 and NCALM seed proposal funding for flying the lidar survey.

3.8.0 REFERENCES

Anderson, R. S., 1990, Evolution of the Northern Santa Cruz Mountains by Advection of Crust Past a San Andreas Fault Bend: Science, v. 249, no. 4967, p. 307-401.

Andrew, J. E., and Walker, J. D., 2017, Path and amount of dextral fault slip in the Eastern California shear zone across the central Mojave Desert: Geological Society of America Bulletin, v. 129, no. 7-8, p. 855-868.

Behr, W. M., Rood, D. H., Fletcher, K. E., Guzman, N., Finkel, R., Hanks, T. C., Hudnut, K. W., Kendrick, K. J., Platt, J. P., Sharp, W. D., Weldon, R. J., and Yule, J. D., 2010, Uncertainties in slip-rate estimates for the Mission Creek strand of the southern San Andreas fault at Biskra Palms Oasis, southern California: Geological Society of America Bulletin, v. 122, no. 9-10, p. 1360-1377.

Bemis, S. P., Micklethwaite, S., Turner, D., James, M. R., Akciz, S., Thiele, S. T., and Bangash, H. A., 2014, Ground-based and UAV-Based photogrammetry: A multi-scale, high-resolution mapping tool for structural geology and paleoseismology: Journal of Structural Geology, v. 69, p. 163-178.

Bemis, S. P., Weldon, R. J., and Carver, G. A., 2015, Slip partitioning along a continuously curved fault: Quaternary geologic controls on Denali fault system slip partitioning, growth of the Alaska Range, and the tectonics of south-central Alaska: Lithosphere, v. 7, no. 3, p. 235-246.

Benowitz, J. A., Layer, P. W., Armstrong, P., Perry, S. E., Haeussler, P. J., Fitzgerald, P. G., and VanLaningham, S., 2011, Spatial variations in focused exhumation along a continental-scale strike-slip fault: The Denali fault of the eastern Alaska Range: Geosphere, v. 7, no. 2, p. 455-467.

Blisniuk, K., Rockwell, T., Owen, L. A., Oskin, M., Lippincott, C., Caffee, M. W., and Dortch, J., 2010, Late Quaternary slip rate gradient defined using high-resolution topography and10Be dating of offset landforms on the southern San Jacinto Fault zone, California: Journal of Geophysical Research, v. 115, no. B8.

Burkett, C. A., Bemis, S. P., and Benowitz, J. A., 2016, Along-fault migration of the Mount McKinley restraining bend of the Denali fault defined by late Quaternary fault patterns and seismicity, Denali National Park & Preserve, Alaska: Tectonophysics, v. 693, p. 489-506.

Buscher, J. T., and Spotila, J. A., 2007, Near-field response to transpression along the southern San Andreas fault, based on exhumation of the northern San Gabriel Mountains, southern California: Tectonics, v. 26, no. 5, p. n/a-n/a.

Carter, J. N., Luyendyk, B. P., and Terres, R. R., 1987, Neogene clockwise tectonic rotation of the eastern Transverse Ranges, California, suggested by paleomagnetic vectors: Geological Society of America Bulletin, v. 98, no. 2, p. 199-206.

Cooke, M. L., and Dair, L. C., 2011, Simulating the recent evolution of the southern big bend of the San Andreas fault, Southern California: Journal of Geophysical Research, v. 116, no. B4.

Cooke, M. L., Schottenfeld, M. T., and Buchanan, S. W., 2013, Evolution of fault efficiency at restraining bends within wet kaolin analog experiments: Journal of Structural Geology, v. 51, p. 180-192.

Cowgill, E., Arrowsmith, J. R., Yin, A., Xiaofeng, W., and Zhengle, C., 2004, The Akato Tagh bend along the Altyn Tagh fault, northwest Tibet 2: Active deformation and the

importance of transpression and strain hardening within the Altyn Tagh system: Geological Society of America Bulletin, v. 116, no. 11-12, p. 1443-1464.
Cunningham, W. D., and Mann, P., 2007, Tectonics of strike-slip restraining and releasing bends: Geological Society, London, Special Publications, v. 290, no. 1, p. 1-12.
DeMets, C., and Dixon, T. H., 1999, New kinematic models for Pacific-North America motion from 3 Ma to present, I: Evidence for steady motion and biases in the NUVEL-1A model: Geophysical Research Letters, v. 26, no. 13, p. 1921-1924.
Dibblee, T. W., 1961, Evidence of strike-slip movement on northwest-trending faults in Mojave Desert, California, *in* Survey, U. S. G., ed., Volume Professional Paper 424-B, p. 197-198.
Dibblee, T. W., 1964a, Geologic map of the Lucerne Valley quadrangle, San Bernardino County, California: U.S. Geological Survey, scale 1:62,500.
Dibblee, T. W., 1964b, Geologic map of the San Gorgonio Mountain quadrangle, San Bernardino and Riverside Counties, California: U.S. Geological Survey, scale 1:62,500.
Dibblee, T. W., 1967, Geologic map of the Morongo Valley quadrangle, San Bernardino and Riverside Counties, California: U.S. Geological Survey, scale 1:62,500.
Dokka, R. K., and Travis, C. J., 1990a, Late Cenozoic strike-slip faulting in the Mojave Desert, California: Tectonics, v. 9, no. 311-340.
Dokka, R. K., and Travis, C. J., 1990b, Role of the eastern California shear zone in accommodating Pacific-North American plate motion: Geophysical Research Letters, v. 17, no. 9, p. 1323-1326.
Fuis, G. S., Scheirer, D. S., Langenheim, V. E., and Kohler, M. D., 2012, A New Perspective on the Geometry of the San Andreas Fault in Southern California and Its Relationship to Lithospheric Structure: Bulletin of the Seismological Society of America, v. 102, no. 1, p. 236-251.
Glazner, A. F., Walker, J. D., Bartley, J. M., and Fletcher, J. M., 2002, Cenozoic evolution of the Mojave block of southern California: Geologic evolution of the Mojave Desert and southwestern Basin and Range: Geological Society of America Memoir, v. 195, p. 19-41.
Golombek, M. P., and Brown, L. L., 1988, Clockwise rotation of the western Mojave Desert: Geology, v. 16, no. 2, p. 126-130.
Gomez, F., Nemer, T., Tabet, C., Khawlie, M., Meghraoui, M., and Barazangi, M., 2007, Strain partitioning of active transpression within the Lebanese restraining bend of the Dead Sea Fault (Lebanon and SW Syria): Geological Society, London, Special Publications, v. 290, no. 1, p. 285-303.
Harris, R. A., and Day, S. M., 1993, Dynamics of fault interaction: Parallel strike-slip faults: Journal of Geophysical Research: Solid Earth, v. 98, no. B3, p. 4461-4472.
Hauksson, E., Jones, L. M., and Hutton, K., 2002, The 1999 M w 7.1 Hector Mine, California, earthquake sequence: complex conjugate strike-slip faulting: Bulletin of the Seismological Society of America, v. 92, no. 4, p. 1154-1170.
Heidbach, O., Rajabi, M., Reiter, K., Ziegler, M., and Team, W., 2016, World stress map database release 2016: GFZ Data Services.
Heidbach, O., Tingay, M., Barth, A., Reinecker, J., Kurfeß, D., and Müller, B., 2008, The world stress map database release 2008, doi: 10.1594/GFZ: WSM. Rel2008, v. 9.
Herbert, J. W., Cooke, M. L., Oskin, M., and Difo, O., 2014, How much can off-fault deformation contribute to the slip rate discrepancy within the eastern California shear zone?: Geology, v. 42, no. 1, p. 71-75.

Johnson, K., Nissen, E., Saripalli, S., Arrowsmith, J. R., McGarey, P., Scharer, K., Williams, P., and Blisniuk, K., 2014, Rapid mapping of ultrafine fault zone topography with structure from motion: Geosphere, v. 10, no. 5, p. 969-986.

Jones, L. E., and Hough, S. E., 1995, Analysis of broadband records from the 28 June 1992 Big Bear earthquake: Evidence of a multiple-event source: Bulletin of the Seismological Society of America, v. 85, no. 3, p. 688-704.

Kendrick, K. J., Matti, J. C., and Mahan, S. A., 2015, Late Quaternary slip history of the Mill Creek strand of the San Andreas fault in San Gorgonio Pass, southern California: The role of a subsidiary left-lateral fault in strand switching: Geological Society of America Bulletin, v. 127, no. 5-6, p. 825-849.

Loveless, J. P., and Meade, B. J., 2011, Stress modulation on the San Andreas fault by interseismic fault system interactions: Geology, v. 39, no. 11, p. 1035-1038.

Lowe, D. G., 2004, Distinctive image features from scale-invariant keypoints: International journal of computer vision, v. 60, no. 2, p. 91-110.

Magistrale, H., and Day, S., 1999, 3D simulations of multi-segment thrust fault rupture: Geophysical Research Letters, v. 26, no. 14, p. 2093-2096.

Matti, J. C., and Morton, D. M., 1993, Paleogeographic Evolution of the San Andreas Fault in Southern California: A Reconstruction Based on a New Cross-Fault Correlation, *in* Powell, R. E., Weldon, R. J., and Matti, J. C., eds., The San Andreas fault system: displacement, palinspastic reconstruction, and geologic evolution, Volume 178: Boulder, CO, Geological Society of America Memoir, p. 107-160.

McGill, S. F., Owen, L. A., Weldon, R. J., and Kendrick, K. J., 2013, Latest Pleistocene and Holocene slip rate for the San Bernardino strand of the San Andreas fault, Plunge Creek, Southern California: Implications for strain partitioning within the southern San Andreas fault system for the last ~35 k.y: Geological Society of America Bulletin, v. 125, no. 1-2, p. 48-72.

McGill, S. F., Spinler, J. C., McGill, J. D., Bennett, R. A., Floyd, M. A., Fryxell, J. E., and Funning, G. J., 2015, Kinematic modeling of fault slip rates using new geodetic velocities from a transect across the Pacific-North America plate boundary through the San Bernardino Mountains, California: Journal of Geophysical Research: Solid Earth, v. 120, p. 2772-2793.

Meade, B. J., and Hager, B. H., 2005, Block models of crustal motion in southern California constrained by GPS measurements: Journal of Geophysical Research, v. 110, no. B3.

Meisling, K. E., and Weldon, R. J., 1989, Late Cenozoic tectonics of the northwestern San Bernardino Mountains, southern California: Geological Society of America Bulletin, v. 101, p. 106-128.

Miller, F. K., and Cossette, P. M., 2004, Preliminary geologic map of the Big Bear City 7.5' quadrangle, San Bernardino County, California: U.S. Geological Survey, scale 1:24,000.

Miller, M. M., Johnson, D. J., Dixon, T. H., and Dokka, R. K., 2001, Refined kinematics of the eastern California shear zone from GPS observations, 1993-1998: Journal of Geophysical Research: Solid Earth, v. 106, no. B2, p. 2245-2263.

Morton, D. M., and Matti, J. C., 1993, Extension and contraction within an evolving divergent strike-slip fault complex: The San Andreas and San Jacinto fault zones at their convergence in southern California, *in* Powell, R. E., Weldon, R. J., and Matti, J. C., eds., The San Andreas fault system: Displacement, palinspastic reconstruction, and geologic

evolution, Volume Memoir 178: Boulder, CO, Geological Society of America, p. 217-230.
Nur, A., Ron, H., and Beroza, G. C., 1993, The nature of the Landers-Mojave earthquake line: Science, v. 261, no. 5118, p. 201-203.
Oskin, M., and Iriondo, A., 2004, Large-magnitude transient strain accumulation on the Blackwater fault, Eastern California shear zone: Geology, v. 32, no. 4.
Oskin, M., Perg, L., Blumentritt, D., Mukhopadhyay, S., and Iriondo, A., 2007, Slip rate of the Calico fault: Implications for geologic versus geodetic rate discrepancy in the Eastern California Shear Zone: Journal of Geophysical Research, v. 112, no. B3.
Oskin, M., Perg, L., Shelef, E., Strane, M., Gurney, E., Singer, B., and Zhang, X., 2008, Elevated shear zone loading rate during an earthquake cluster in eastern California: Geology, v. 36, no. 6, p. 507.
Owen, L. A., Finkel, R. C., Minnich, R. A., and Perez, A. E., 2003, Extreme southwestern margin of late Quaternary glaciation in North America: Timing and controls: Geology, v. 31, no. 8, p. 729-732.
Plattner, C., Malservisi, R., Furlong, K. P., and Govers, R., 2010, Development of the Eastern California Shear Zone—Walker Lane belt: The effects of microplate motion and pre-existing weakness in the Basin and Range: Tectonophysics, v. 485, no. 1, p. 78-84.
Rangel, T., and McGill, S., 2016, Low Slip Rate for San Gorgonio Pass Section of the San Andreas Fault Inferred from Geodesy, Geological Society of America Abstracts with Programs, Volume 14-5.
Reitman, N. G., Bennett, S. E. K., Gold, R. D., Briggs, R. W., and DuRoss, C. B., 2015, High-Resolution Trench Photomosaics from Image-Based Modeling: Workflow and Error Analysis: Bulletin of the Seismological Society of America, v. 105, no. 5, p. 2354-2366.
Rockwell, T., Lindvall, S., Herzberg, M., Murbach, D., Dawson, T., and Berger, G., 2000, Paleoseismology of the Johnson Valley, Kickapoo, and Homestead Valley faults: Clustering of earthquakes in the eastern California shear zone: Bulletin of the Seismological Society of America, v. 90, no. 5, p. 1200-1236.
Rubin, C., 1996, Systematic underestimation of earthquake magnitudes from large intracontinental reverse faults: Historical ruptures break across segment boundaries: Geology, v. 24, no. 11, p. 989-992.
Savage, J., Gan, W., and Svarc, J., 2001, Strain accumulation and rotation in the Eastern California Shear Zone: Journal of Geophysical Research: Solid Earth, v. 106, no. B10, p. 21995-22007.
Schwartz, S. Y., Orange, D. L., and Anderson, R. S., 1990, Complex fault interactions in a restraining bend on the San Andreas Fault, southern Santa Cruz Mountains, California: Geophysical Research Letters, v. 17, no. 8, p. 1207-1210.
Segall, P., and Pollard, D., 1980, Mechanics of discontinuous faults: Journal of Geophysical Research: Solid Earth, v. 85, no. B8, p. 4337-4350.
Sharp, R. P., Allen, C. R., and Meier, M. F., 1959, Pleistocene glaciers on southern California mountains: American Journal of Science, v. 257, no. 2, p. 81-94.
Shelef, E., and Oskin, M., 2010, Deformation processes adjacent to active faults: Examples from eastern California: Journal of Geophysical Research: Solid Earth, v. 115, no. B5.
Sieh, K., Jones, L., Hauksson, E., Hudnut, K., Eberhart-Phillips, D., Heaton, T., Hough, S., Hutton, K., Kanamori, H., Lilje, A., Lindvall, S., McGill, S., Mori, J., Rubin, C., Spotila, J. A., Stock, J., Thio, H. K., Treiman, J., Wernicke, B., and Zachariasen, J., 1993, Near-

field investigations of the Landers earthquake sequence, April to July, 1992: Science, v. 260, p. 171-176.
Snavely, N., Seitz, S. M., and Szeliski, R., 2007, Modeling the World from Internet Photo Collections: International Journal of Computer Vision, v. 80, no. 2, p. 189-210.
Spinler, J. C., Bennett, R. A., Anderson, M. L., McGill, S. F., Hreinsdóttir, S., and McCallister, A., 2010, Present-day strain accumulation and slip rates associated with southern San Andreas and eastern California shear zone faults: Journal of Geophysical Research, v. 115, no. B11.
Spotila, J. A., and Anderson, K. B., 2004, Fault interaction at the junction of the Transverse Ranges and Eastern California shear zone: a case study of intersecting faults: Tectonophysics, v. 379, no. 1-4, p. 43-60.
Spotila, J. A., Farley, K. A., and Sieh, K., 1998, Uplift and erosion of the San Bernardino Mountains associated with transpression along the San Andreas fault, California, as constrained by radiogenic helium thermochronometry: Tectonics, v. 17, no. 3, p. 360-378.
Spotila, J. A., Farley, K. A., Yule, J. D., and Reiners, P. W., 2001, Near-field transpressive deformation along the San Andreas fault zone in southern California, based on exhumation constrained by (U-Th)/He dating: Journal of Geophysical Research: Solid Earth, v. 106, no. B12, p. 30909-30922.
Spotila, J. A., and Sieh, K., 2000, Architecture of transpressional thrust faulting in the San Bernardino Mountains, southern California, from deformation of a deeply weathered surface: Tectonics, v. 19, no. 4, p. 589-615.
Sylvester, A. G., 1988, Strike-slip faults: Geological Society of America Bulletin, v. 100, no. 11, p. 1666-1703.
Thatcher, W., Savage, J. C., and Simpson, R. W., 2016, The Eastern California Shear Zone as the northward extension of the southern San Andreas Fault: Journal of Geophysical Research: Solid Earth, v. 121, no. 4, p. 2904-2914.
Ullman, S., The interpretation of structure from motion, *in* Proceedings Proc. R. Soc. Lond. B1979, Volume 203, The Royal Society, p. 405-426.
Wakabayashi, J., 2007, Stepovers that migrate with respect to affected deposits: field characteristics and speculation on some details of their evolution: Geological Society, London, Special Publications, v. 290, no. 1, p. 169-188.
Wald, D. J., and Heaton, T. H., 1994, Spatial and temporal distribution of slip for the 1992 Landers, California, earthquake: Bulletin of the Seismological Society of America, v. 84, no. 3, p. 668-691.
Weldon, R. J., and Sieh, K., 1985, Holocene rate of slip and tentative recurrence interval for large earthquakes on the San Andreas fault, Cajon Pass, southern California: Geological Society of America Bulletin, v. 96, no. 793-812.
Wells, D. L., and Coppersmith, K. J., 1994, New empirical relationships among magnitude, rupture length, rupture width, rupture area, and surface displacement: Bulletin of the seismological Society of America, v. 84, no. 4, p. 974-1002.
Wesnousky, S. G., 1988, Seismological and structural evolution of strike-slip faults: Nature, v. 335, no. 6188, p. 340.
Westoby, M. J., Brasington, J., Glasser, N. F., Hambrey, M. J., and Reynolds, J. M., 2012, 'Structure-from-Motion' photogrammetry: A low-cost, effective tool for geoscience applications: Geomorphology, v. 179, p. 300-314.

Wetmore, P., Xie, S., Gallant, E., Owen, L., and Dixon, T., A New Geological Slip Rate Estimate for the Calico Fault, Eastern California: Implications for Geodetic Versus Geologic Rate Estimates in the Eastern California Shear Zone, *in* Proceedings AGU Fall Meeting Abstracts2017.

Yeats, R. S., Sieh, K. E., and Allen, C. R., 1997, The geology of earthquakes, Oxford University Press, USA.

Yule, D., 2009, The enigmatic San Gorgonio Pass: Geology, v. 37, no. 2, p. 191-192.

Yule, D., and Sieh, K., 2003, Complexities of the San Andreas fault near San Gorgonio Pass: Implications for large earthquakes: Journal of Geophysical Research, v. 108, no. B11.

3.9.0 TABLES

Table 1. Airborne lidar survey flight parameters and sensor settings

Flight Parameters		Equipment settings	
Flight altitude	700 m	Wavelength	1550, 1064, & 532 nm
Flight speed	72 m/s	Beam divergence	0.5-1.0 mrad
Swath width	800 m	Laser PRF	75 kHz
Swath overlap	50%	Scan frequency	25 Hz
Point density	4.47 pts/m^2	Scan angle	± 30^o
Horizontal resolution (1σ)	0.127 m	Scan cutoff	± 1^o
Vertical resolution (1σ)	< 5-15 cm	Scan offset	0^o

Table 2. UAV modeling parameters and results

Site	Model area (m^2)	Number of images	Number of GCP's	Point density (pts/m^2)	Ground resolution (m/pixel)	DSM resolution (m/pixel)	Root mean squared (m)
Lone Valley site	804,000	3372	43	519	0.022	0.044	0.83
Lake Peak site	260,000	780	9	292	0.029	0.058	2.12
Gully cut-bank	39.4	223	N/A	$1.17x10^9$	0.000463	0.000926	N/A

3.10.0 FIGURES

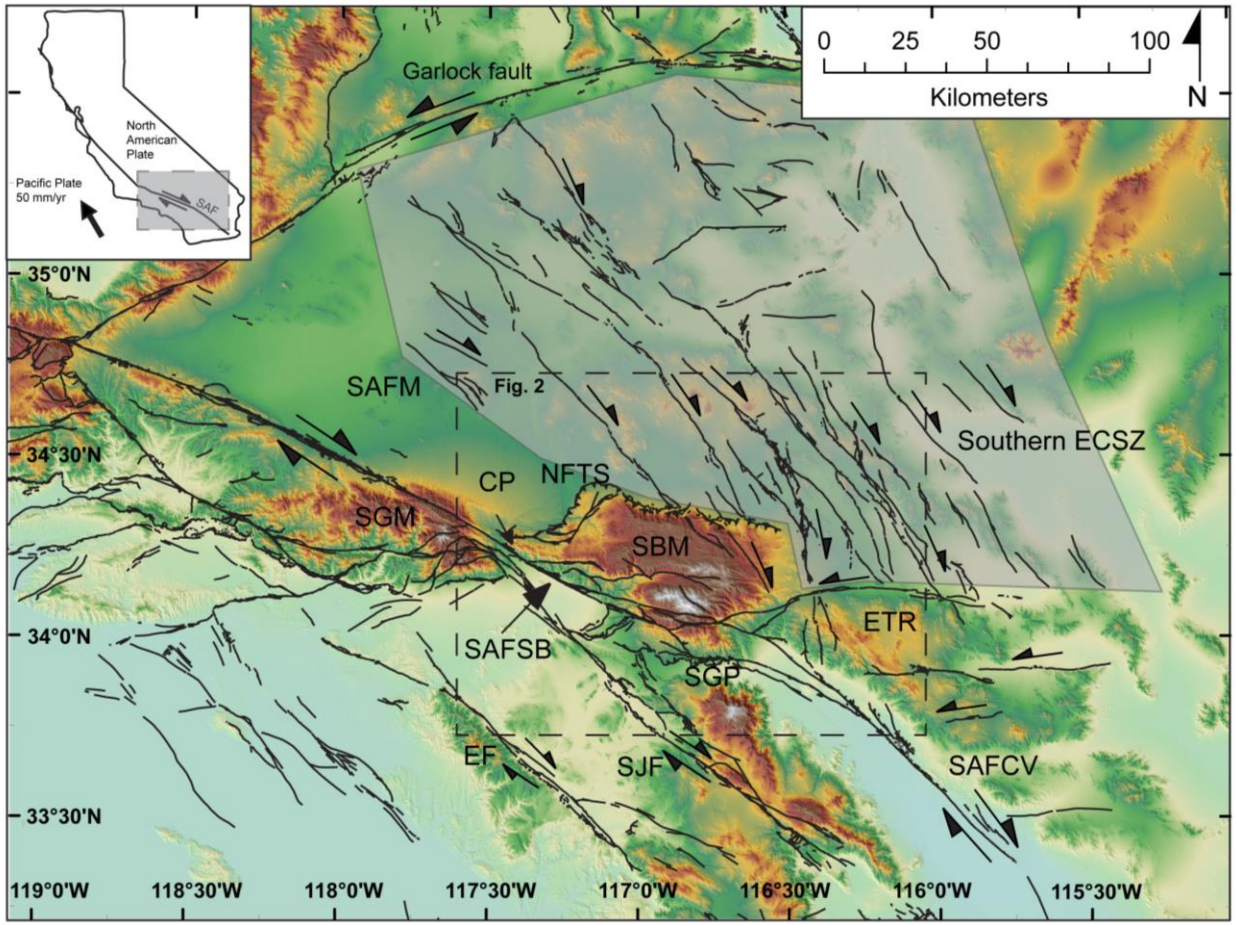

Fig. 10. Relationship between the ECSZ and San Andreas fault zone. Inset: location of San Andreas fault and plate velocity vector from (DeMets and Dixon, 1999). ECSZ – Eastern California shear zone; EF – Elsinore fault; ETR – Eastern Transverse Ranges; NFTS – North Frontal thrust system; SAFCV – Coachella Valley segment of San Andreas fault; SAFM – Mojave segment of San Andreas fault; SB – San Bernardino segment of San Andreas fault; SGM – San Gabriel Mountains; SGP – San Gorgonio Pass; SJF – San Jacinto fault.

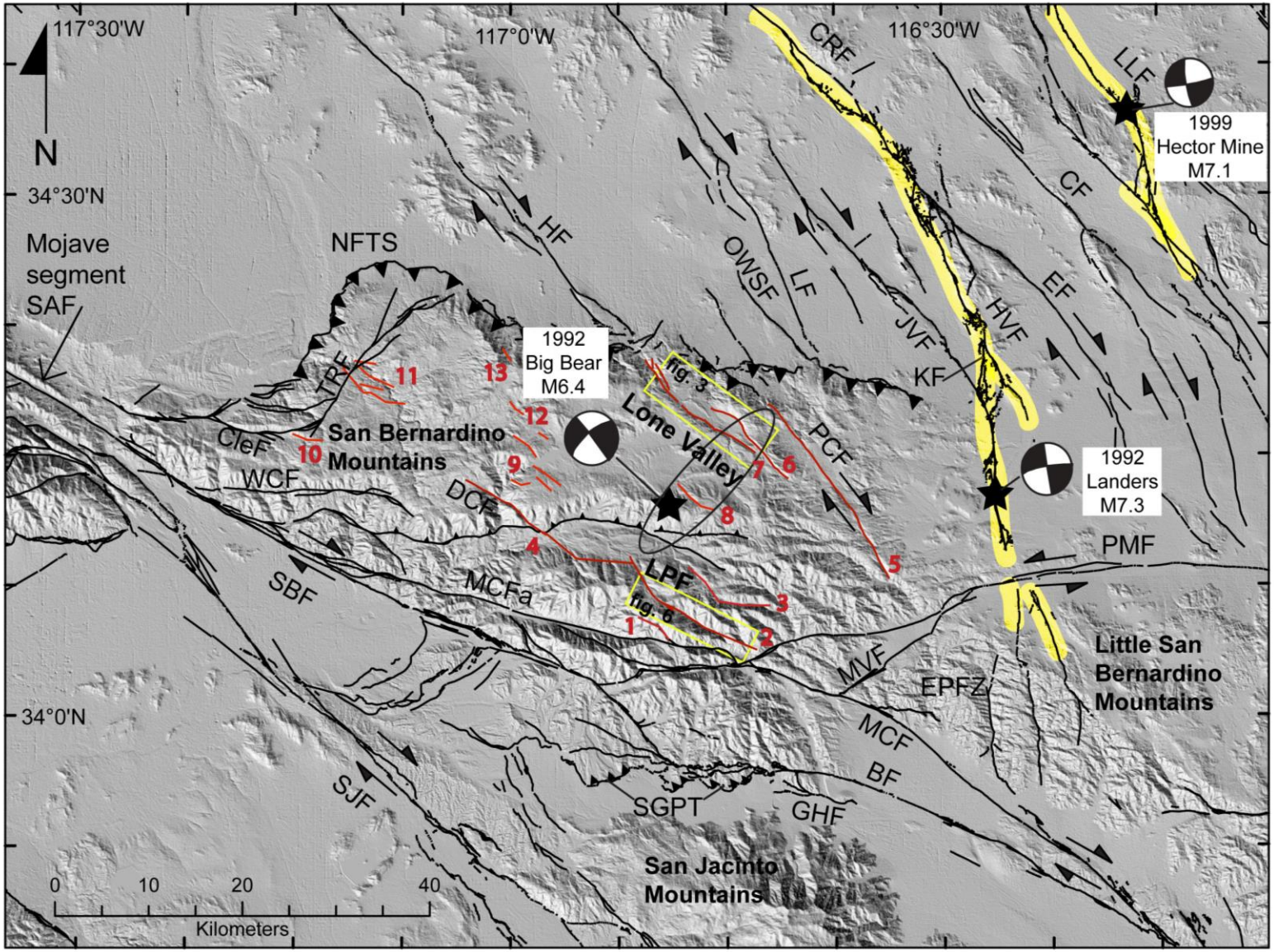
117°30'W
117°0'W
116°30'W
N
34°30'N
34°0'N
Mojave segment SAF
NFTS
HF
OWSF
LF
CRF
LLF
CF
EF
HVF
JVF
KF
PCF
PMF
1999 Hector Mine M7.1
1992 Big Bear M6.4
1992 Landers M7.3
Lone Valley
fig. 3
fig. 6
LPF
San Bernardino Mountains
Little San Bernardino Mountains
San Jacinto Mountains
RF
CleF
WCF
DCF
SBF
MCFa
MVF
EPFZ
MCF
BF
GHF
SGPT
SJF
1
2
3
4
5
6
7
8
9
10
11
12
13
0
10
20
40
Kilometers

Fig. 11. Fault map for the San Bernardino Mountains and southern Eastern California shear zone. Faults are denoted in black and red. Black faults are from (Survey, 2006). Red faults were originally mapped by (Dibblee, 1964a;b;1967a;b). Numbers next to red faults correspond to fault groups used for Fig. 10a. Yellow lines represent surface rupture during the 1992 Landers earthquake (Sieh et al., 1993) and the 1999 Hector Mine earthquake (Hauksson et al., 2002). Ellipse represents the rough trend of the epicentral location of the 1992 Big Bear aftershock sequence (Jones and Hough, 1995). BF – Banning fault; CF – Calico fault; CleF – Cleghorn fault; CRF – Camp Rock fault; DCF – Deer Creek fault; EF – Emerson fault; EPFZ – Eureka Peak fault zone; GHF – Garnet Hills fault; HF – Helendale fault; JVF – Johnson Valley fault; KF – Kickapoo fault; LF – Lenwood fault; LLF – Lavic Lake fault; LPF – Lake Peak fault; MCF – Mission Creek fault; MCFa – Mill Creek fault; MVF – Moronga Valley fault; NFTS – North Frontal thrust system; OWSF – Old Woman Springs fault; PCF – Pipes Creek fault; PMF – Pinto Mountain fault; SAF – San Andreas fault; SBF – San Bernardino fault; SGPT – San Gorgonio Pass thrust zone; SJF – San Jacinto fault; TRF – Tunnel Ridge fault; WCF – Waterman Canyon fault

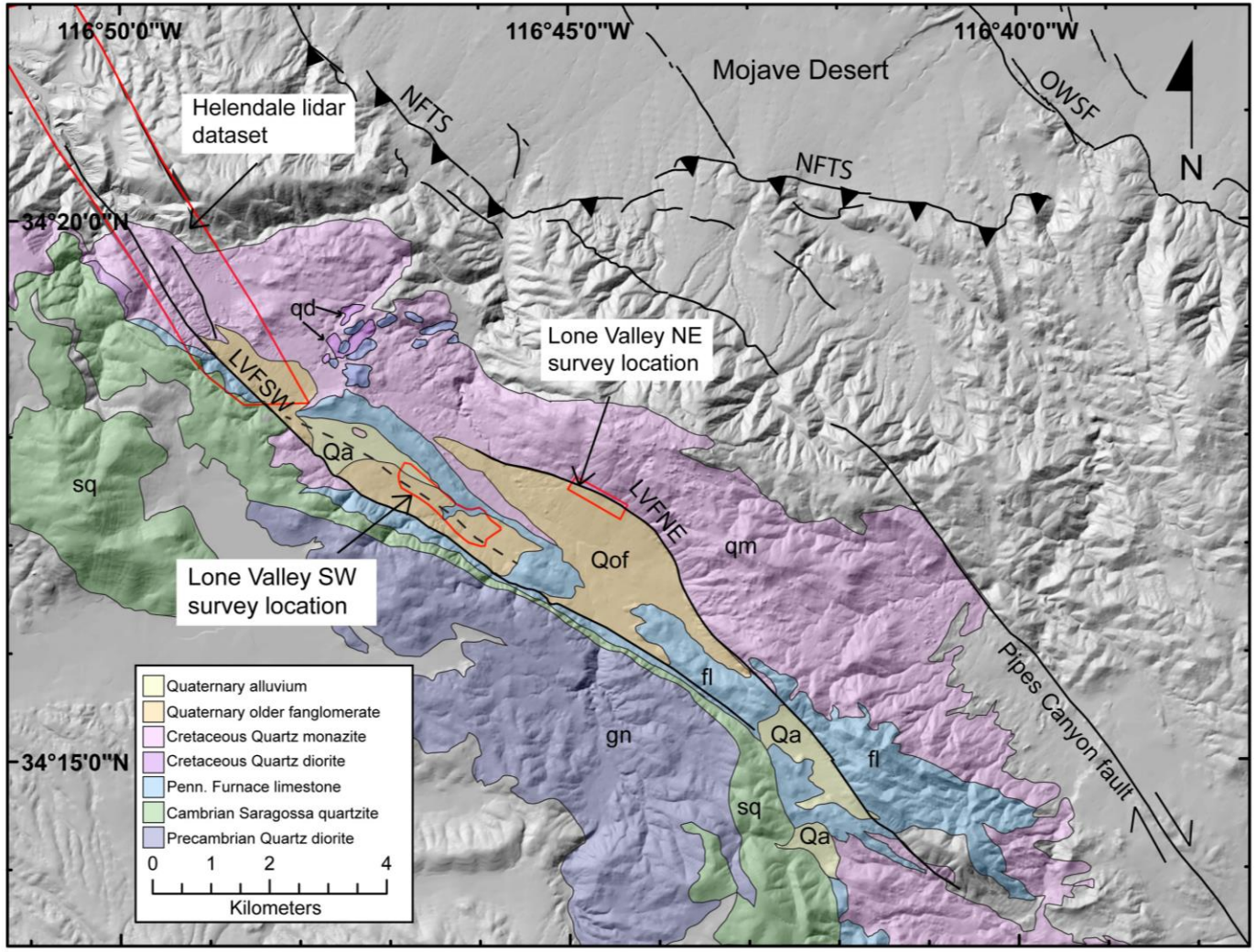

Fig. 12. Fault location and bedrock geology map modified from (Dibblee, 1964a;b;1967a;b) for Lone Valley. Red outlines indicate data extent of high-resolution topography surveys (both lidar and UAV). The Helendale lidar survey data can be found at (www.opentopogrpahy.org). Faults represented by black lines are from (Survey, 2006). LVFNE – Lone Valley fault northeast; LVFSW – Lone Valley fault southwest; OWSF – Old Woman Springs fault; NFTS – North Frontal thrust system

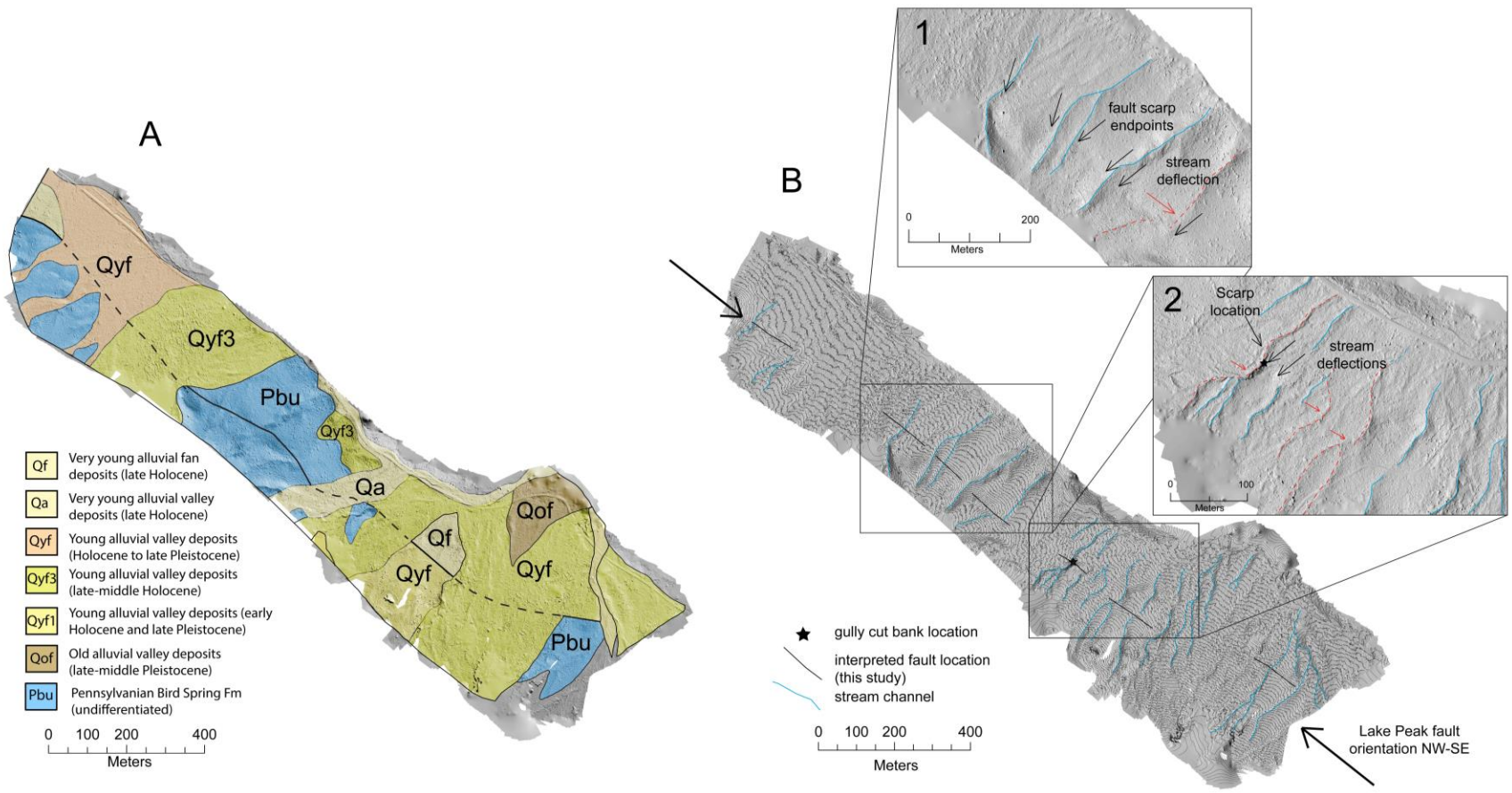

Fig. 13. Lone Valley fault southwest site showing the surface mapping (A) by (Miller and Cossette, 2004) and the high-resolution hillshade (B) from our UAV survey. A) Bedrock and surficial geology previously mapped by Miller and Cossette (2004) indicates Quaternary age faulting which cut across several young alluvial surfaces. B) UAV hillshade overlain by a 1-meter contour map derived from the UAV DEM. Black lines represent interpreted faults based on lineaments found in the hillshade from this study. The star is the location of Fig. 5. Ephemeral stream channels were traced based on contours and show a series of deflected channels (B-1 & 2). B1 and B2 are insets showing endpoints for topographic step locations (black arrows) and deflected stream channels (red dashed lines).

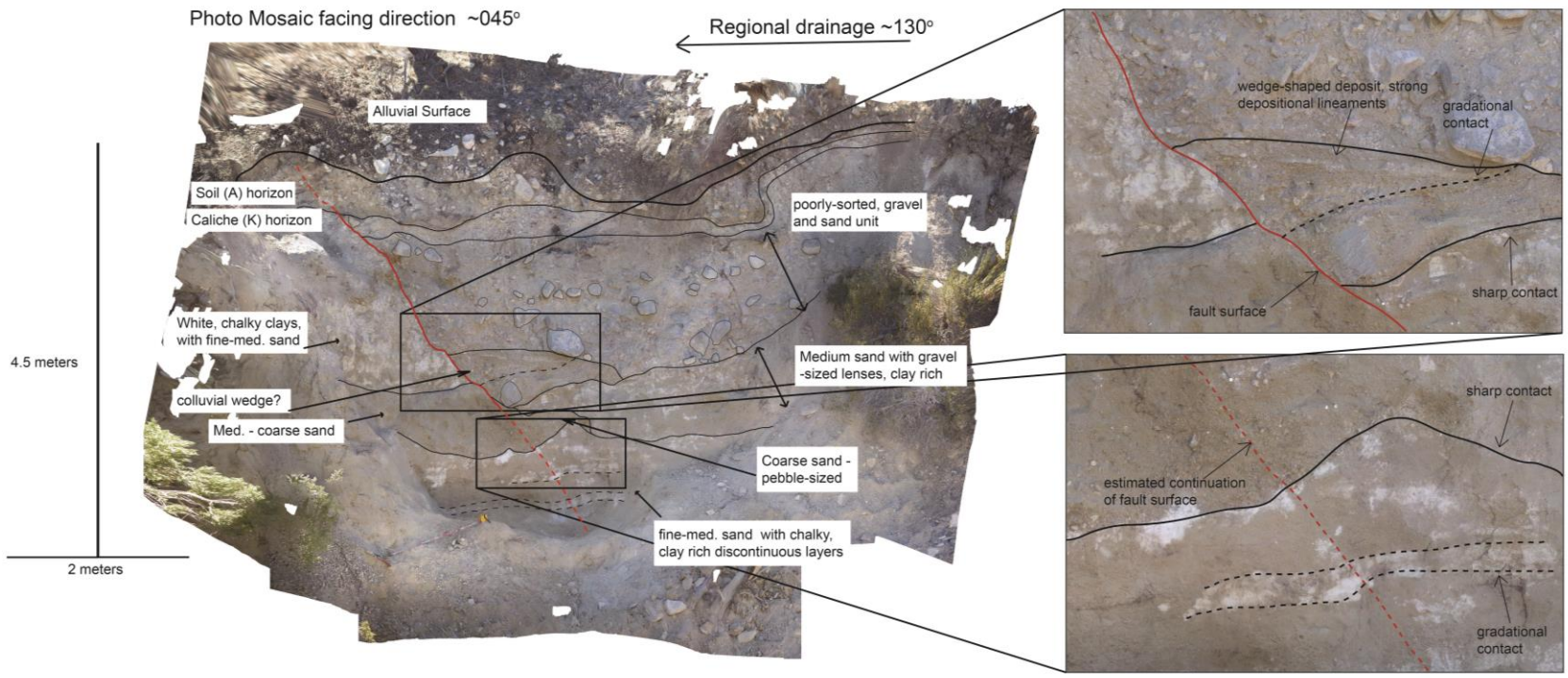

Fig. 5. Photomosaic using Agisoft Photoscan from a cut-bank within an ephemeral stream along the southwest side of Lone Valley (see Fig. 4B for location). A clear discontinuity exists between coarse, poorly sorted gravel and fine-medium sand and white clay (red line). Upper right inset shows a potential colluvial wedge deposits forming right at the contact between these two units. No true master fault could be found at depth, and could potentially be lost in the finer grained, massive unit at the base of our excavation (lower right panel). Black lines represent contacts between the sediment packages mapped during field work. Dashed lines are gradational contacts and solid lines are sharp contacts.

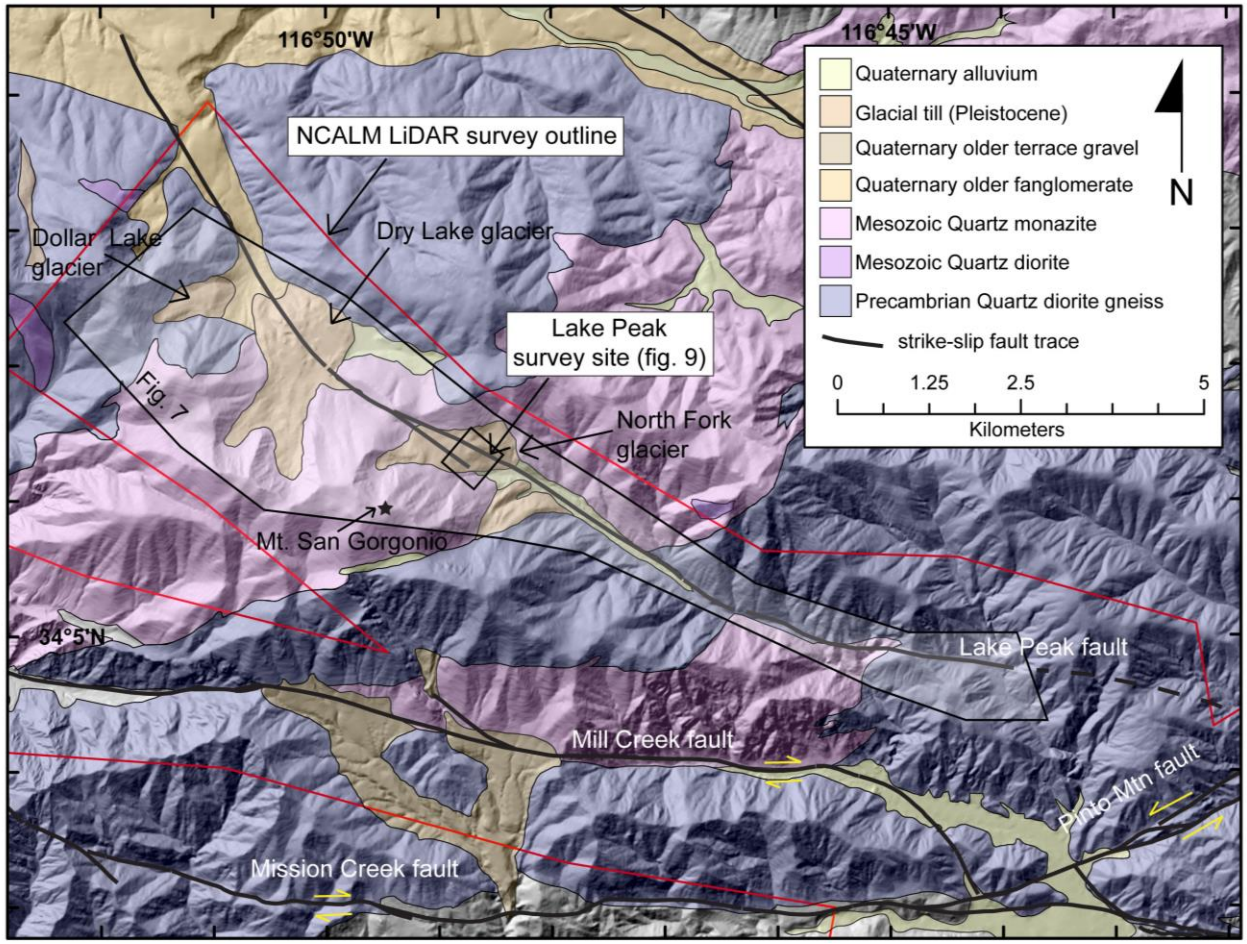

Fig. 6. Bedrock geology map modified from (Dibblee, 1964b) overlaid on a 1/3 arc second DEM- derived hillshade. Locations for the Lake Peak, Mill Creek, Mission Creek, and Pinto Mountain faults form a nexus of converging strike-slip faults in Whitewater River watershed. The red outline shows the extent of our NCALM survey in the San Bernardino Mountain and is publicly available at (www.opentopography.org). Black lines represent the faults. The black transparent strip is the location of our strip map found in Fig. 7. The Lake Peak fault can be seen cutting across the three glacial deposits, namely the North Fork, Dry Lake, and Dollar Lake glaciers.

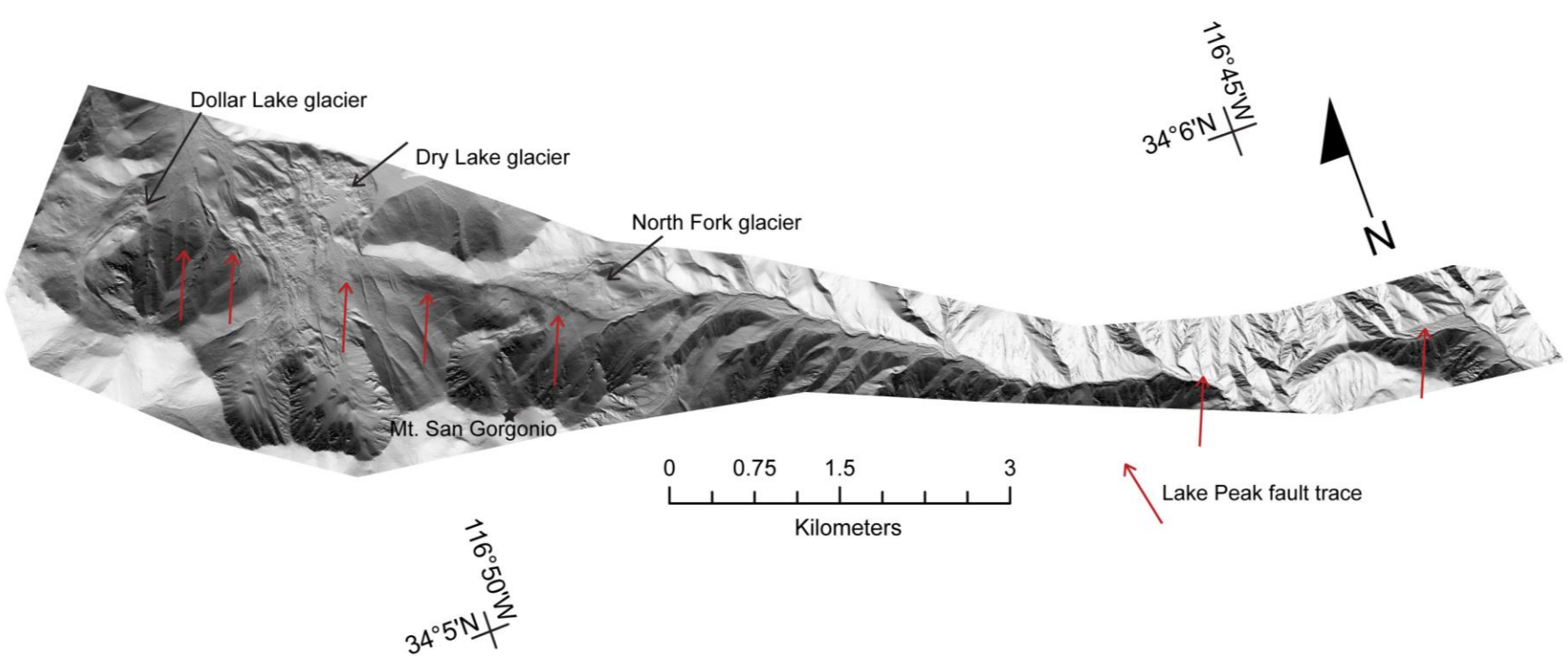

Fig. 7. One-meter DEM-derived hillshade (lighting direction 090 °) map of North Fork drainage (Whitewater River) showing the locations of several fault scarps of the Lake Peak fault (red arrows). Four panels were cut, from NW (Fig. 8a)-SE (Fig. 8d), from this hillshade and used as the basis for geomorphic mapping. The Dollar Lake, Dry Lake, and North Fork glaciers were originally described by (Sharp et al., 1959). Radiometric ages (see Fig. 8a-d for location) for each of these glaciers were produced using cosmogenic nuclides, originally from (Owen et al., 2003).

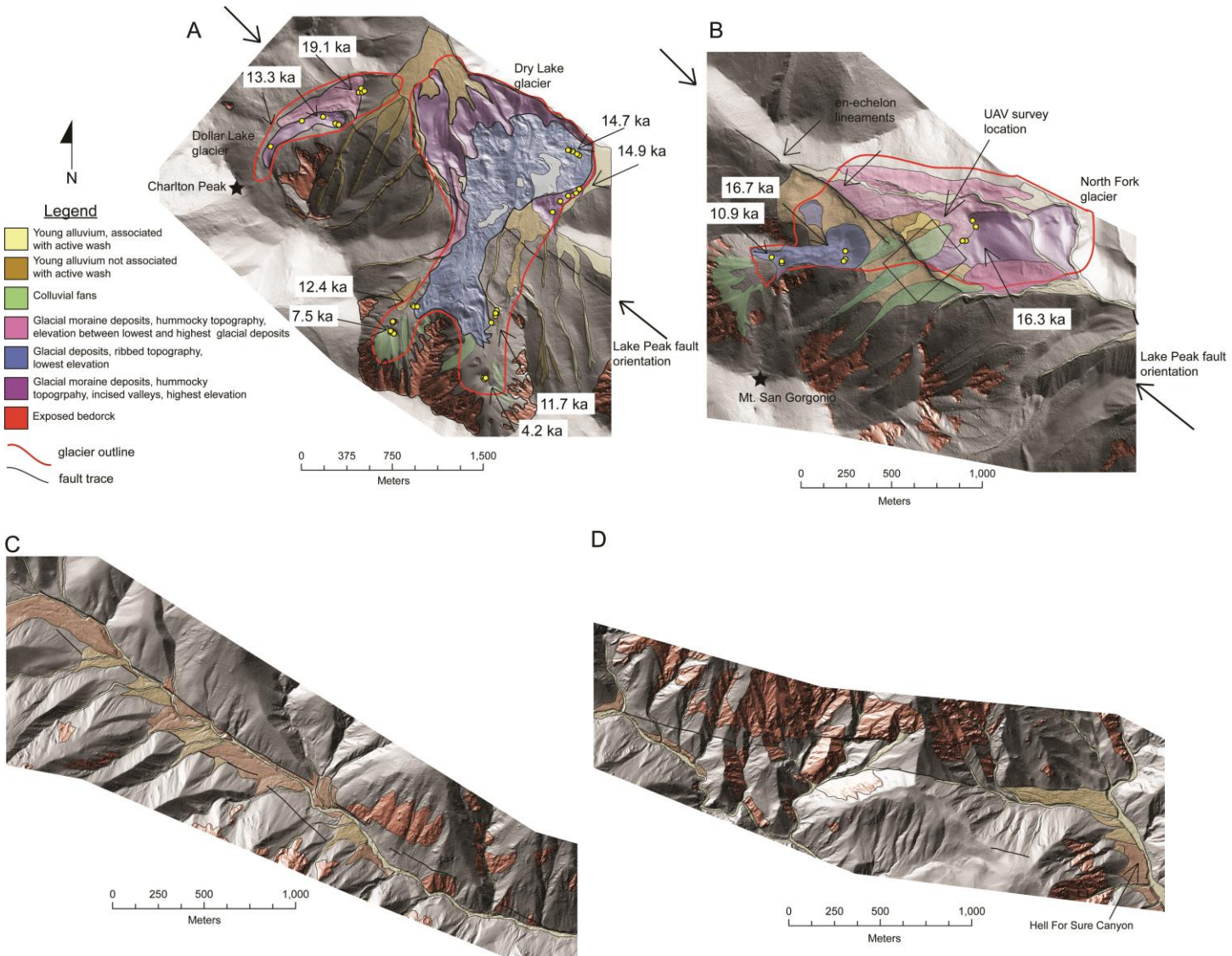
A
19.1 ka
13.3 ka
Dry Lake glacier
14.7 ka
14.9 ka
Dollar Lake glacier
N
Charlton Peak
Legend
Young alluvium, associated with active wash
Young alluvium not associated with active wash
Colluvial fans
Glacial moraine deposits, hummocky topography, elevation between lowest and highest glacial deposits
Glacial deposits, ribbed topography, lowest elevation
Glacial moraine deposits, hummocky topogrpahy, incised valleys, highest elevation
Exposed bedorck
glacier outline
fault trace
12.4 ka
7.5 ka
Lake Peak fault orientation
11.7 ka
4.2 ka
0 375 750 1,500
Meters
B
en-echelon lineaments
UAV survey location
North Fork glacier
16.7 ka
10.9 ka
16.3 ka
Lake Peak fault orientation
Mt. San Gorgonio
0 250 500 1,000
Meters
C
0 250 500 1,000
Meters
D
0 250 500 1,000
Meters
Hell For Sure Canyon

Fig. 8. Four panels (a-d) were clipped from the lidar hillshade and used as a basis for geomorphic mapping. Mapping was based on field evidence, surface elevation, and geomorphology of the surface (e.g. hummocky, ribbed, etc.). The Lake Peak fault trace is en-echelon and discontinuous. Yellow dots represent average cosmogenic ages grouped together by location. Original ages were produced by (Owen et al., 2003). Black lines represent interpreted fault lineaments from this study. Red outlines in A and B are the glacial extent of the moraines mapped by (Sharp et al., 1959). A) Geomorphic mapping of the Dry Lake and Dollar Lake glaciers showing the fault lineaments crossing both the glacial deposits and the young alluvium. B) Surficial geology mapping of the North Fork glacier suggests multiple periods of deposition of young colluvium since glacial retreat in the Pleistocene. C) and D) Mapping were based solely on the lidar and indicate discontinuous lineaments throughout the North Fork Drainage. The juxtaposition of young alluvium in the active wash suggests Quaternary activity of the Lake Peak fault.

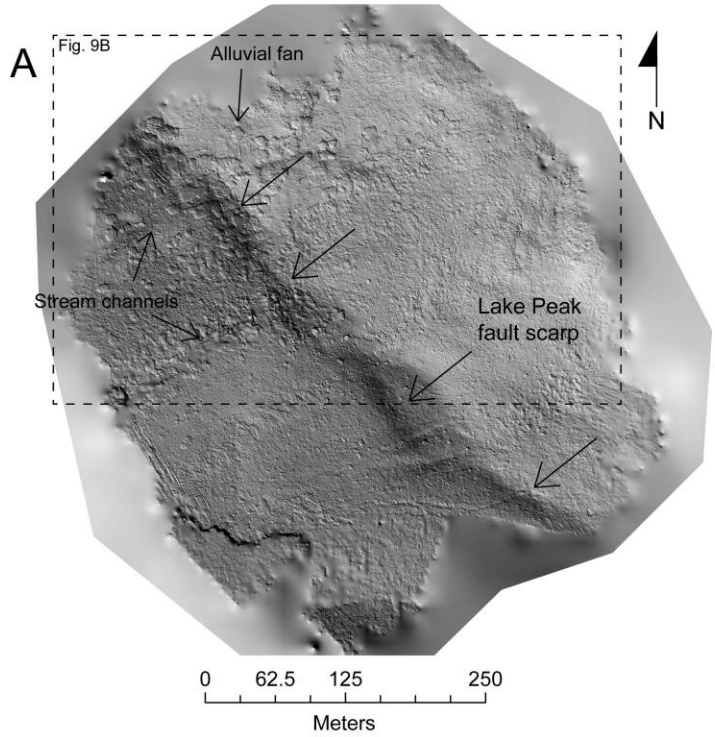
A
Fig. 9B
Alluvial fan
N
Stream channels
Lake Peak
fault scarp
0
62.5
125
250
Meters

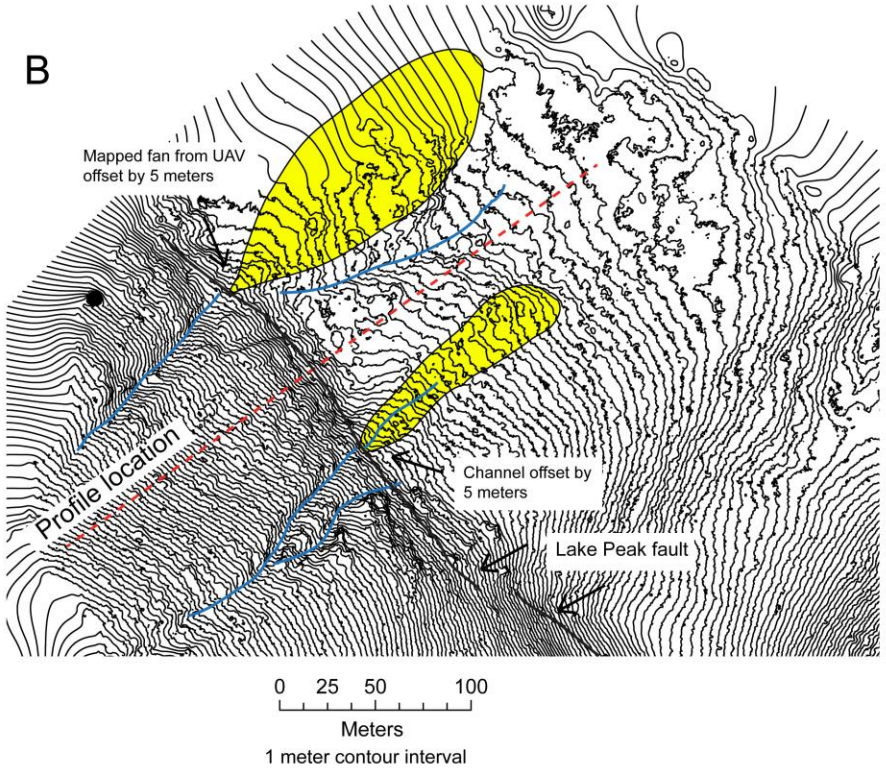
B
Mapped fan from UAV
offset by 5 meters
Profile location
Channel offset by
5 meters
Lake Peak fault
0
25
50
100
Meters
1 meter contour interval

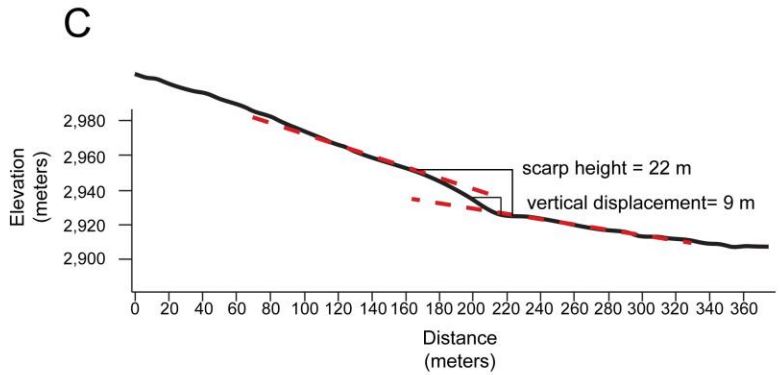
C
Elevation
(meters)
2,980
2,960
2,940
2,920
2,900
scarp height = 22 m
vertical displacement= 9 m
0
20
40
60
80
100
120
140
160
180
200
220
240
260
280
300
320
340
360
Distance
(meters)

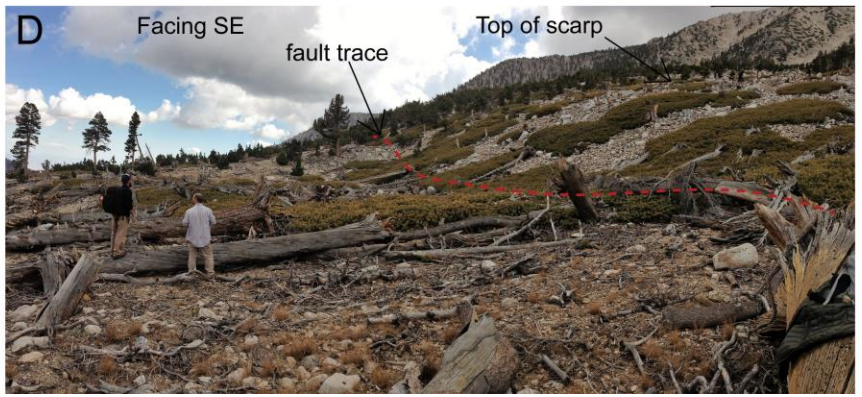
D
Facing SE
fault trace
Top of scarp

Fig. 9. Lake Peak UAV survey site. Two surveys were combined to using manual flight mode for generation of surface model along the fault scarp. A) UAV DEM (5-cm resolution) derived hillshade (lighting direction from SW). Points were classified using Agisoft Photoscan parameters 0.10 meters and 15 degrees. As a result, the model interpolated across the areas were vegetation was removed and can leave a “lunar surface”. At the resolution we have obtained, little information is lost during point classification. Scarp endpoints are represented by black arrows. B) One-meter contour map showing interpretation from our high-resolution topography. Two 5-meter offsets are interpreted at the front of the fault scarp: 1) interpreted as the apex of an alluvial fan is matched to the mouth of the channel to the northwest, and 2) the dextral offset channel across the scarp based on topographic contours and field evidence. C) profile of Lake Peak scarp (see B for location) showing the magnitude of both the total scarp height and the vertical separation. The vertical separation assumes that the near-vertical fault is located at the toe of the scarp. D). Field photo facing southeast showing the magnitude of the fault scarp and the loose, poorly defined nature of the deposits which are cut by the fault.

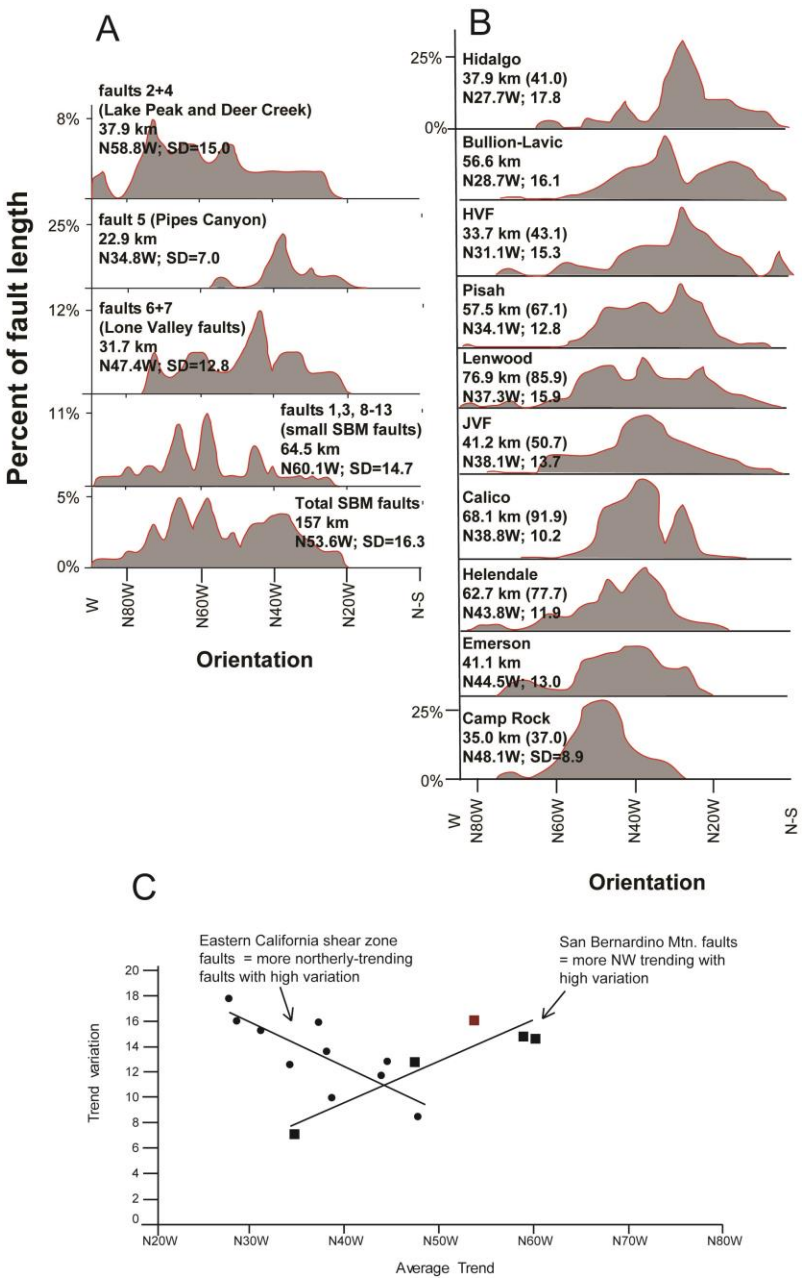

Fig. 10. Distribution of orientation of faults within the SBM and the ECSZ (see Fig. 2 for locations). A) Orientation of SBM faults in 1-km increments. Faults were grouped based on length, and geographic location (i.e. latitude). Four groups of faults were used and are roughly arrange from south (top) to north (bottom) and indicate that faults become more westerly-trending from south to north. The average trend of faults in the SBM is N54W. B) Orientation of southern ECSZ in 1-km increments. Similarly, these faults are arranged from south (top) to north (bottom) and show a similar trend of increasing western-trending faults towards the north. C) Average trend vs. trend variation (standard deviation) plot for SBM (squares) and ECSZ (circles) faults. ECSZ faults show high variation for more northerly-trending faults, while the SBM faults show that more northwesterly-trending faults have high variation. The average trend vs. variation for all SBM faults is shown as the red square.

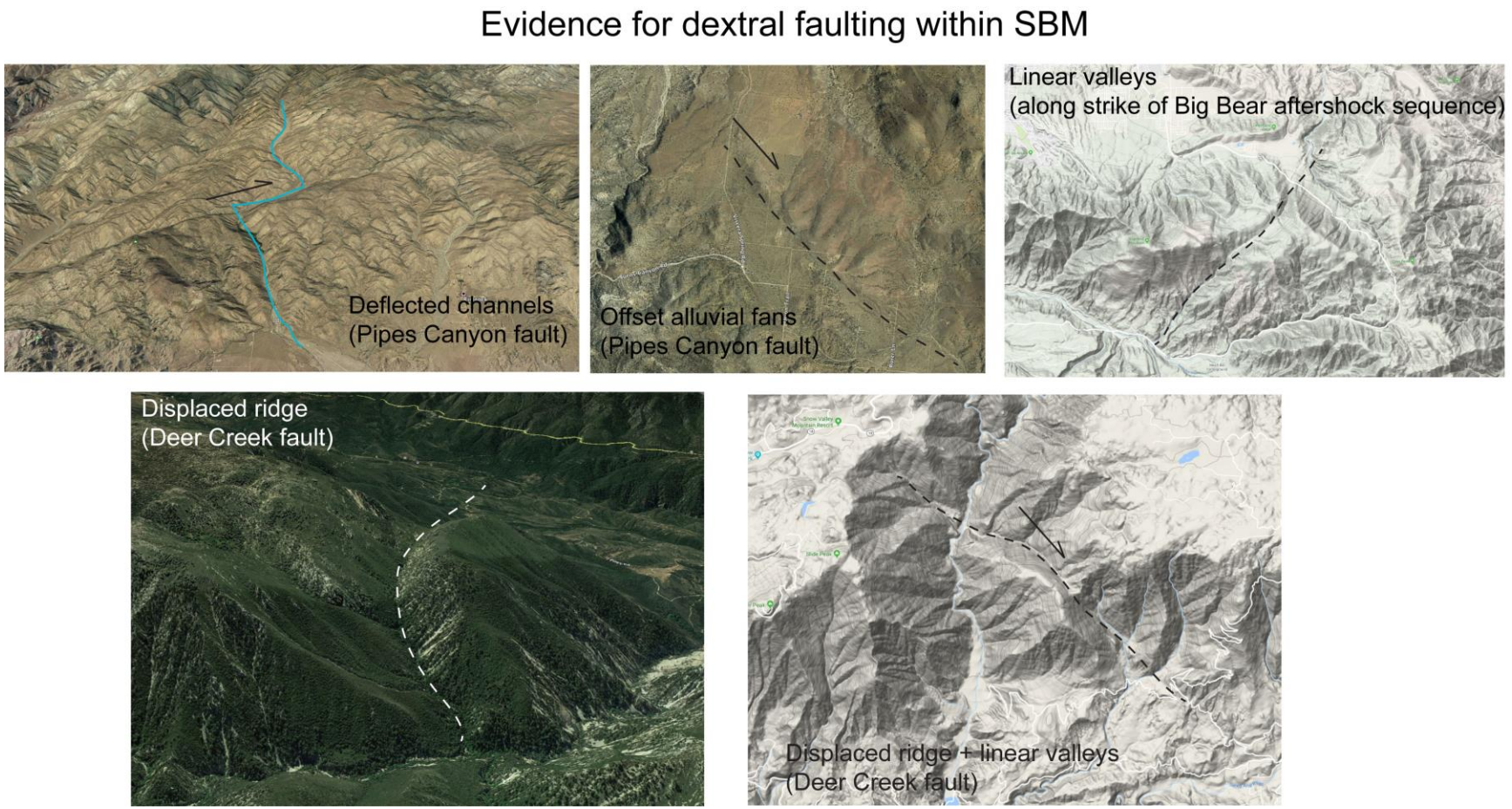

Figure 11. Google Earth and Google Maps screen captures of various locations within the SBM showing evidence for strike-slip faulting. The Pipes Canyon fault (two upper left) shows two, 1.8 km right-lateral offsets: one in the form of a deflected stream, and the other as an offset alluvial fan. The upper right shows a linear valley along within the trend of the 1992 Big Bear aftershock epicentral locations and may represent the surface expression of this known fault. The bottom two show an offset ridge along the Deer Creek fault. The fault kinematics of these locations are unknown and should be the focus of future neotectonic studies within the SBM.

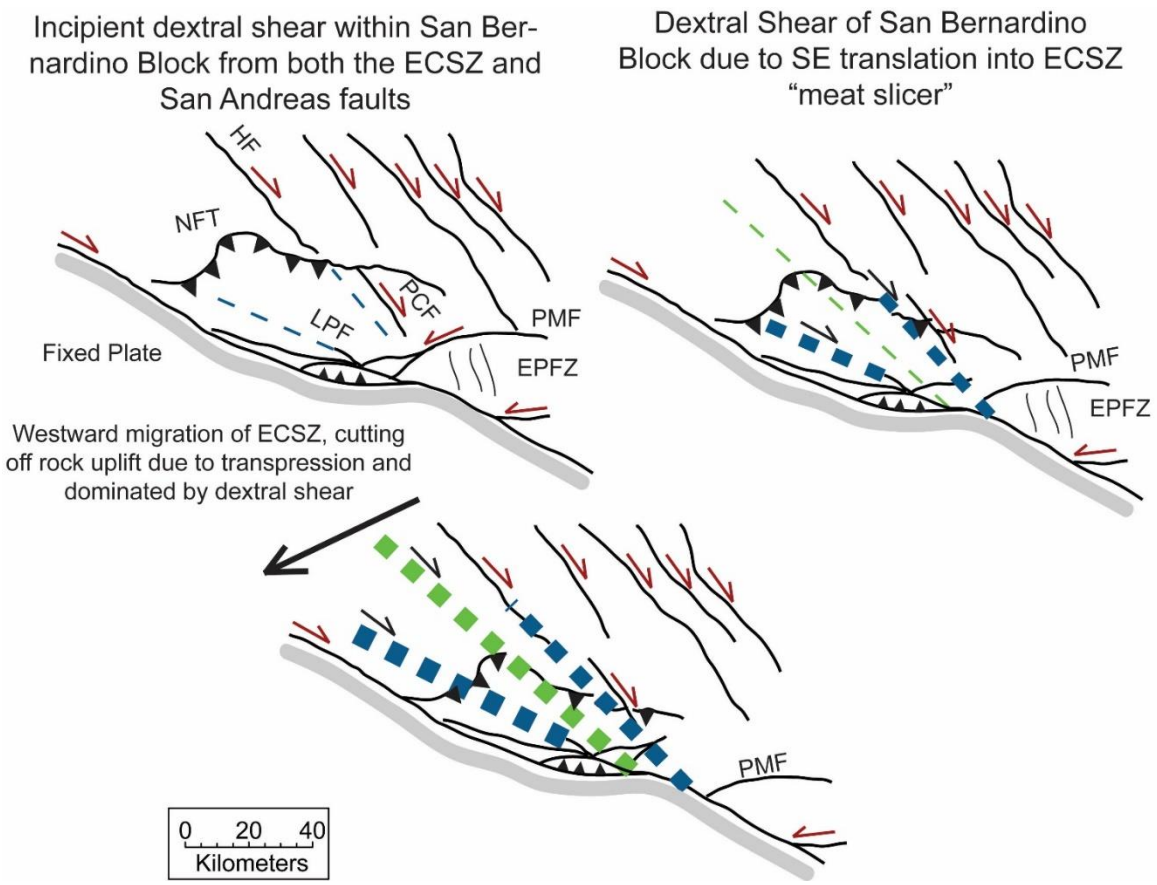

Fig. 12. "Meat slicer" model showing the eastward migration of the ECSZ. The evidence for incipient faulting within the SBM, and the along-strike nature of these faults with the ECSZ, suggests that as the SBM are translating towards the SE, faulting develops within the SBM and connects to the ECSZ (upper left). As time passes, through-going faults begin to develop and connect with the SAF to the south (upper right). The Blue lines represent active faults and the green lines represent incipient faults. Eventually the translation of the SBM towards the SE and the eventual migration of the ECSZ to the west will transpfer slip from the ECSZ to the southern SAF via dextral faulting. EPFZ – Eureka Peak fault zone; HF – Helendale fault; LPF – Lake Peak fault; PCF – Pipes Canyon fault; PMF – Pinto Mountain fault; NFT – North Frontal thrust

3.11.0 SUPPLEMENT MATERIAL

Table 1. UAV model parameters for Lone Valley (NE)

Site	Model area (m^2)	Number of images	Number of GCP's	Point density (pts/m^2)	Ground resolution (m/pixel)	DEM resolution (m/pixel)	Root mean squared (m)
Lone Valley (NE)	270,000	748	10	417	0.025	0.049	4.19

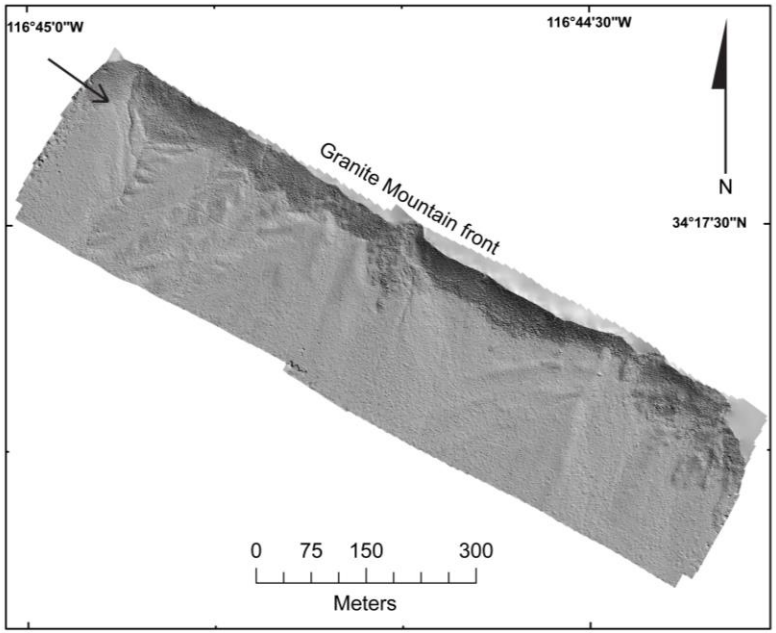

Figure 1. UAV-derived hillshade of the northeastern side of Lone Valley (see figure 3 for location). Lineaments along the mountain front present little evidence for recent faulting. No channel offsets or displaced alluvium could be found, both in the field and using high-resolution topography. While this is a most probable location for faulting prior to the Pleistocene?, we suggest the northeast side of Lone Valley to be inactive.